Dynamics of Hydrogen Bond Networks in the Condensed Phase: Ultrafast X-ray Absorption Spectroscopy

BY

YISHUO JIAO

B.S., HEBEI UNIVERSITY, 2010

Advisor: Prof. Christoph G. Rose-Petruck

A DISSERTATION SUBMITTED IN PARTIAL FULFILLMENT OF THE REQUIREMENTS FOR THE DEGREE OF DOCTOR OF PHILOSOPHY IN THE DEPARTMENT OF CHEMISTRY AT BROWN UNIVERSITY

PROVIDENCE, RHODE ISLAND

MAY 2017

This dissertation by Yishuo Jiao is accepted in its present form
by the Department of Chemistry as satisfying the
dissertation requirement for the degree of Doctor of Philosophy.

Date _____ _____

Christoph G. Rose-Petruck, Advisor

Recommended to the Graduate Council

Date _____ _____

Jimmie D. Doll, Reader

Date _____ _____

Lai-Sheng Wang, Reader

Approved by the Graduate Council

Date _____ _____

Andrew G. Campbell, Dean of the Graduate School

VITA

Yishuo Jiao was born in Xingtai, Hebei, China in 1989. He attended Hebei University in the fall of 2006, where he performed undergraduate research about the temperature sensitive polymer materials under the guidance of Prof. Kuilin Deng. He graduated from college in 2010 with a Bachelor of Science degree, majored in Materials Chemistry. In 2011, Yishuo enrolled in the chemistry graduate program at Brown University. While at Brown under the guidance of Christoph Rose-Petruck, he studied condensed phase acoustic phonon effects using ultrafast x-ray absorption spectroscopy, and the electrochemical properties of clathrate hydrates with respect to CO_2 reduction. The research was conducted at both Brown University and Argonne National Laboratory. He presented posters about the electrochemical work at the CO_2 Sequestration and Conversion Gordon Conference in May 2015, and gave a lecture about solvent shell coherent movement at the January 2016 northeastern regional meeting for ultrafast dynamics. At Brown, he served as a teaching assistant for the general chemistry course, and also acted as head TA for all course sections. He was awarded with honorarium the Gordon Research Conference and Dissertation Fellowship by the Chemistry Department of Brown University. He completed all requirements for PhD degree in December 2016.

ACKNOWLEDGEMENT

There are so many people to thank, all of whom were integral parts of my time at Brown University and the completion of this thesis.

First and foremost, I owe the greatest gratitude to my advisor, Prof. Christoph Rose-Petruck for his fabulous guidance and help in the research we conducted. His talent and creativity in experimental design, prestigious physical insight and kind guidance made my graduate studies an invaluable experience. He exposed me to a series of cutting-edged techniques, and provided many opportunities to contribute to the development of novel problem solving strategies. I believe that these opportunities did not only train me in science, but also prepared me for general challenges of the future. I can never thank him enough for all he did in my five years in his lab.

I would also like to thank our main collaborator, Dr. Bernhard W. Adams, the then beamline scientist we worked with in Argonne National Laboratory. Since most of my research was done at the Advanced Photon Source, Argonne National Lab, I was able to regularly conduct experiments with him. Dr. Adams is a very knowledgeable physicist, who taught me almost as much as Prof. Rose-Petruck. It was such an awesome experience to work with him. Additional collaborators include the theoretical group led by Prof. Hannes Jónsson at the University of Iceland. I am grateful for the support provided by Prof. Jónsson and his postdoc, Dr. Asmus Ougaard Dohn. Despite Dr. Dohn

and I never having met in person, we were able to engage in an efficient and fruitful exchange of ideas via email.

The Rose-Petruck group has always been a cool combination of nice students from various backgrounds. It has been very pleasant to work with them for the past several years. Among all the students, I would like to start by thanking our former group member, Dr. Francisco Schunk, one of my best friends in the United States. Frank and I entered the group in the same year, and in that respect shared the same learning curves. Even though we did not work on the same project we developed a pattern of consulting each other about research issues for inspiration before seeking Prof. Rose-Petruck's guidance. We have had so many fruitful discussions about our research that we sometimes even joke that we are each other's "secondary advisor". Conversations ranging from very formal and serious scientific debates to very relaxed chat when we were very drunk in the bar not only resulted in a solid friendship, but also improved my spoken English and understanding of American culture.

When I entered the group, there were several graduate students who are older than myself. They were Dr. Yanan Liu, Dr. Petr Bruza and Dr. Danielle Rand. They all provided help in either a direct or indirect way. All of them are very-well trained scientist. Their dedicated, systematic and methodical way of conducting research all became a general guideline for the execution of my own research. Dr. Bruza is one of the most gifted experimentalist I have ever seen in my life. It is such an enjoyable process to watch him working on instruments. It was his work in the lab that got me to believe experiments can be as entertaining as good games; a notion that helped me through this relatively long period of life saturated with experimental work.

Besides working at the APS, I also spent some time doing work in the field of electrochemistry. This work was done with our former group member, Daniel DeCcicio. Daniel is a very active person with a quick and sharp mind. He is full of fresh ideas and provided me with lots of helpful problem solving suggestions. Daniel possesses a broad knowledge base and is like a walking Wikipedia. He seems to have a mental image of science at large that allows him to have ideas spanning many disciplines of science.

I would also like to thank, current group members Joseph Daou and Alexandra Kat Stephan. I did not work directly with them, yet know them to be wonderful colleagues and officemates. Joseph is very dedicated and thorough in his course work and research, and I am confident that he is capable of complete whatever work lies before him. Alexandra is a uniquely talented researcher that solves problems in her own way. She has a clear plan about what she is doing and her future. These characteristics lead me to believe that she is going to obtain ground-breaking research results I am looking forward to seeing.

I must thank the chemistry department staff for facilitating my graduate career. The list individuals that helped me is rather long, but I must mention some of them explicitly. Ken Talbot, Randy Goulet and Al Tente offered me their technical expertise, without which I would not have been able to execute my experiments. Allen Sylvia, Robert Wilson and Eric Friedfeld helped me purchase the items I required to conduct the work contained in this thesis.

Finally, I need to acknowledge my beloved parents. Without their love and support, I could not have finish this thesis. Their encouragements were always the most important driving force for me to cross all the barriers I confronted in the graduate study. I also

want to express my thanks to my whole family and my close friends for sharing happiness with me and helping me getting rid of negative moods I had.

CONTENTS

LIST OF TABLES

LIST OF FIGURES

CHAPTER 1. INTRODUCTION AND MOTIVATION

Water molecules may undergo several different forms of motion, including single molecule vibration, librational motion (hindered rotation), intermolecular vibration and reorientation. The hydrogen bonds of water result in local regular arrangements of molecules, such as the tetrahedral structure.[1] The intermolecular bonds of water are what make its properties unique and challenging to understand. The complexity of aqueous environments has led to long-standing contention within this field of scientific research. Conflict persists over hydrogen bonding dynamics in both neat water and solution of solute species.

Single water molecule reorientation detected by IR takes approximately half of the time required for bulk water dipole moment reorientation detected by dielectric spectroscopy.[2-5] Collective reorientation involves several co-dependent mechanisms that are not well understood.[5] Therefore, a rigorous explanation which reconciles these observations does not exist.

Methods to study the effects solutes have on water in the immediate and extended vicinities have been developed within the past few decades. Bakker and his co-workers conducted a series of IR pump-probe experiments to study the reorientation of O-H bonds.[6] They concluded there is no so-called long range ionic structure breaking or structure making in electrolyte solutions. Instead of a homogeneous liquid, the ionic solutions have been described as a colloidal suspension of particles composed of the ionic solute surrounded by one or two hydration layers.[7-8] By hyper-polarization light scattering, Chen *et al.* observed long-range perturbations of the hydrogen bonding network induced by ions.[9] Sheldon conducted a series of hyper-Rayleigh light scattering experiments and, in agreement with Chen *et al.*, concluded that there is a long-range

dipole moment correlation effect in liquid water. The correlation domains are at least 23nm and can extend to up to hundreds of nanometers.[10].

Dynamic Light Scattering experiments revealed the formation of high solute concentration domains in aqueous solutions that exist on length scales larger than those proposed by Chen.[11-12] The formation of these domains is attributed to the hydrogen bond interactions between both solute-water and water-water molecules.[13] These domains have been shown to be common to many aqueous solutions, and stable up to several months.[14] The existence of these domains can be intimately related to the manner in which solute molecules perturb the surrounding aqueous environment on length scales small compared to the domain size.

Recently, phonons were discovered both experimentally and theoretically, and are used to interpret the dynamics in liquids.[2, 10, 15] Acoustic phonons were proposed to be responsible for long-range correlation effects in aqueous solutions,[10] and phonon sound speed characterization in liquid water was used to determine one of the structural relaxation times to be 0.6 ps.[2] Therefore, the collective motions in water (phonons) play an important role in understanding the complex dynamics that occur within the liquid phase. Phonons represent a means for the potential reconciliation of the oddities and conflicts listed above by permitting the interpretation of spectra in terms of both photon-matter interaction and more collective motion occurring over longer-ranges.[15]

Experimental studies of phonons are all based on macroscopic scale light-scattering experiments, which probe the integrated scatter signal from the whole sample.[2] This integrated scatter signal is a measure of the dynamics that occur on scales that are large relative to the molecular level. In this thesis, the study of phonons via microscopic probes, and the importance of this approach will be discussed.

Clathrate hydrates are another example of the important role hydrogen bonds play in the dynamics of water. Clathrate hydrates are water-based, ice-like solids generally formed at low temperatures and pressures above 100 bar. Small gas molecules can be trapped in the "cage" composed of frozen water molecules linked by hydrogen bonds Clathrate hydrates can store up to two orders of magnitude more CO_2 than clathrate-free water under similar conditions. For instance, 1L of clathrate hydrates can trap as much as 170L of CO_2.[16-17] This enables storage and transfer of large amounts of CO_2 by sequestration into clathrates, establishing an avenue to study high concentration CO_2 dynamics in the liquid phase. The work presented in this thesis covers the utilization of clathrate hydrates as a means of delivering high concentration carbon dioxide to the electrode surface in the electrochemical reduction of CO_2 to higher hydrocarbons.

In this thesis, localized phonons are used for studying the hydrogen bond network in high-solute-concentration domains. In the second Chapter, the background and mechanisms relevant to the dynamics and its detection method will be discussed. In the third Chapter, the experimental setup is discussed. In the fourth Chapter, the theoretical calculation methods and results are presented. Chapters five and six show the results and analysis of the ultrafast spectroscopy experiments. Chapter 7 is a brief discussion about clathrate hydrates and their application to the electrochemical reduction of CO_2. Chapter 8 summarizes contents of this thesis and future plans.

CHAPTER 2. XAS AND DYNAMICS IN AQUEOUS SOLUTIONS

2.1 The X-ray Absorption Spectroscopy (XAS)

2.1.1 Principles of X-ray Absorption

The interaction of x-ray photons and bound electrons can be divided into three categories, absorption and inelastic (Campton) and elastic (Rayleigh) scattering. Each process is characterized by its respective cross section. The process cross sections are determined by x-ray photon energy, the atomic number Z, and the chemical environment. X-ray Absorption Spectroscopy probes absorption by measuring the probability that a photon is absorbed by the excitement of inner-shell electrons into photoexcited states. Changes in the factors affecting the absorption cross section are reflected in the probability of absorption. Absorption can be further labeled by an alphabetical scheme corresponding to the principle quantum number of the orbital from which the photo excited electron made a transition. K, L and M transitions are made by electrons that resided in the 1^{st}, 2^{nd} and 3^{rd} shell respectively. The work to be discussed below involves K edge transitions exclusively.

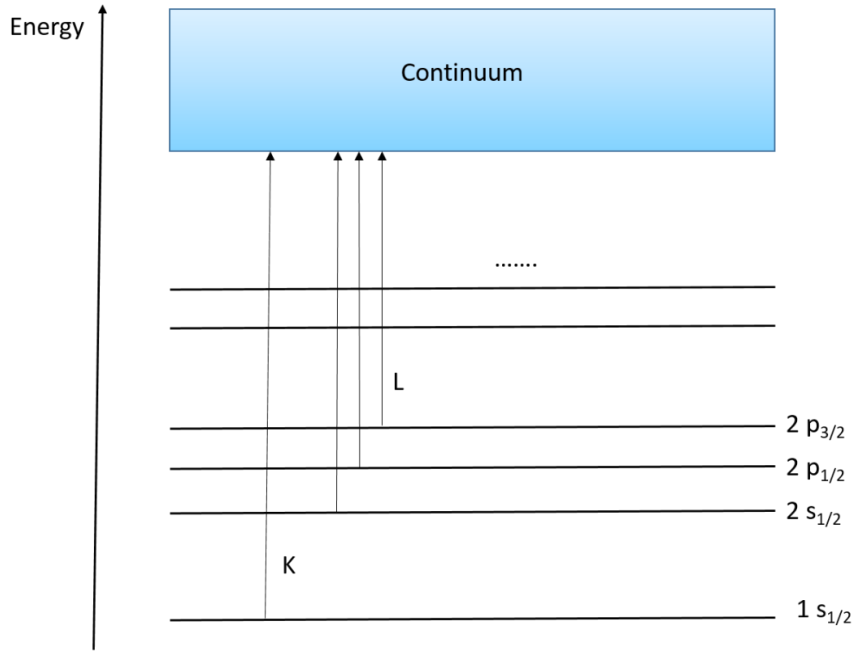

Figure 2.1 Nomenclature of transitions from different core-electrons absorptions. Here only K and L edges are shown. The transition can be excited into continuum or unoccupied energy states. More details are to be discussed in the following sections.

For a given absorption edge the X-ray absorption spectra, edge can be divided into low and high probe energy regions, named XANES (X-ray Absorption Near Edge Spectra and EXAFS (Extended X-ray Absorption Fine Spectra) respectively. In the XANES region the probing x-ray photon energy is within a 50-eV range above the ionization threshold, and in the EXAFS region the probing phone energy ranges from 50eV to 1000eV above the ionization threshold. [18-19] Figure 2.2. shows a typical XAS region division, with Ferro and Ferric Hexacyanide as sample.

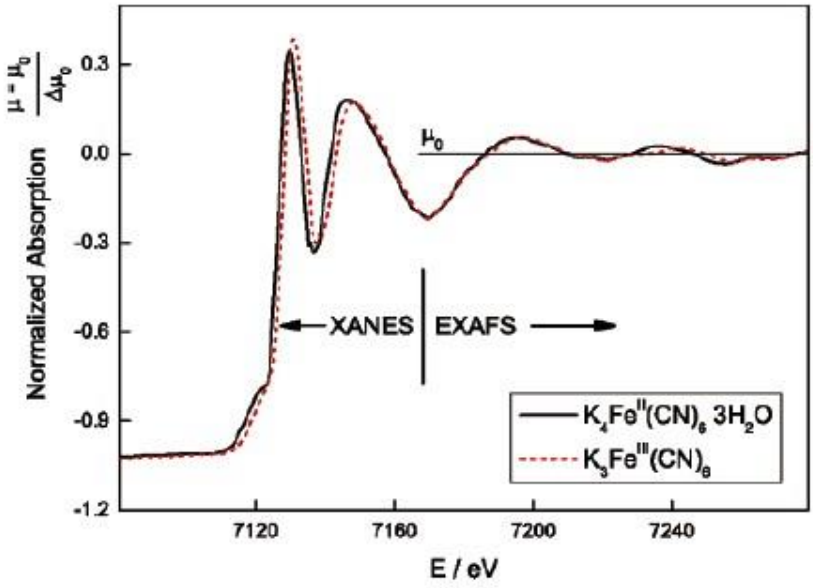

Figure 2.2 Nomenclature of transitions from different core-electrons absorptions. Here only K and L edges are shown. The transition can be excited into continuum or unoccupied energy states. More details will be given in the following sections. Taken from Ref [19].

2.1.2 EXAFS Region

If X-ray absorption results in the excitation of an electron into a continuum state, there is a subsequent physical process that accompanies absorption, photoelectron scattering. After excitation to a continuum state a photoelectron will propagate with wave-vector *k* determined by the excitation energy and its bound energy in the absorption atom:

$$E_k = h\nu - E_B \tag{2.1}$$

$$k = \frac{2\pi}{\hbar}\sqrt{2m(h\nu - E_B)} \tag{2.2}$$

The photoelectron wave is then scattered by neighboring atoms. The scattering process is categorized as either a single scattering or multiple scattering event.

Figure 2.3 The illustration of scattering process of photoelectron spherical wave propagating through the neighborhood of absorption atom. The picture is taken from Ref [19].

The oscillatory feature in the EXAFS region is due to interference between the outgoing photoelectron wave and the waves backscattered from neighboring atoms. The dominant effect is due to a single scattering off of atoms in the vicinity of the absorbing atom.[19] While the probing region used in this thesis does not lie in the EXAFS region, discussion of the absorption process will begin with the EXAFS region for its relative simplicity. Also, some of the parameters used to describe this region can still bear meaning in the XANES region. The XANES calculations will be presented in Chapter 4.

The oscillatory signal in the EXAFS region is best mathematically described by

$$\chi(k) = S_0^2 \sum_i N_i \frac{|f(k)|}{kr_i^2} \sin(2kr_i + 2\delta_c + \phi)\, e^{-2r_i/\lambda(k)} e^{-2\sigma_i^2 k^2} \tag{2.3}$$

The calculation is summed over subgroups indexed with i, the subgroups are defined by N_i atoms with the same structural property, such as bond length r_i, thermal-fluctuations and structural disorder factor σ_i. The backscattering amplitude is $f(k) = |f(k)|e^{i\phi(k)}$ and is the most important factor in the specification of the oscillatory signal. The factors $2\delta_c$and ϕ describe the phase shift due to the interaction between the photoelectron and all relevant atoms.

The mean free path of the photoelectron is *λ(k)*, and its modulation effect on the EXAFS signal amplitude is captured by the term $e^{-2r_i/\lambda(k)}$.

In the calculation, the atomic positions must not be fixed to account for thermal motion. To solve this problem, the atomic positions are defined with a Gaussian distribution $e^{-2\sigma_i^2 k^2}$, where σ_i is the Debye-Waller factor. This term can also account for possible structure disorders in some systems. Finally, S_0^2 is a factor that describes many-body effects that may be involved in the X-ray absorption process.[20]

The derivation of the EXAFS equation starts with the approximation that a photoelectron only interacts with its backscattered waves. In reality, the creation of a core hole after photoexcitation will lead the electrons in the photoexcitation atom to be embedded in a different potential. Also, the passive electrons can be excited by the photoelectron, or the active electron, via Coulomb interaction. The passive electrons in the valence shell can either be excited to a higher energy bound state, which is the shake-up process, or into continuum, which is the shake-off process.[21] All of these possible effects are described by the S_0^2 factor. This factor is a phenomenological treatment of the inelastic losses after photoelectrons are created and is usually approximated as a constant.

2.1.3 Pre-edge and XANES Region

During X-ray absorption, if the inner-core electron is excited into an energy level above the Fermi energy yet below the ionization threshold, a pre-edge feature is seen in a series of 3d transition metal complexes. The complexes have specific symmetries, like a Td Structure. In the pre-edge region, the absorption is a transition from a 1s to a 3d orbital in the metal atom. This transition is forbidden by the dipole transition operator, thus having a small transition rate. The special symmetry of the molecule allows for strong mixing of 3d and 4p orbitals. The mixing of orbitals, with 1s to 4p transition allowed, resulted in the pre-edge absorption.[22] The transition sensitivity to ligand symmetry about the metal center makes XAS pre-edge features of transition metal complexes a means of a probing the species' environment. This concept will be delineated over the course of this thesis.

In the XANES region, multiple scattering processes dominate. The photoelectron has lower kinetic energy in comparison with those produced in the EXAFS region, and will be scattered multiple times by neighboring atoms. EXAFS spectra carry geometric information about pair-correlation function. XANES spectra contain information about bond length, bond angle and chemical oxidation states, etc. The theoretical calculation of the absorption cross section in the XANES region requires starting from the calculation of transition rate based on the Fermi's Golden Rule:

$$\mu(E) \propto \sum_{f}^{E_f > E_F} |\langle f|\hat{\varepsilon}\cdot\vec{r}|i\rangle|^2 \delta(E - E_f) \tag{2.4}$$

Here $\hat{\varepsilon}\cdot\vec{r}$ is the transition dipole operator describing the interaction between the X-ray electromagnetic wave and the absorbing atom. One approach to calculating the absorption cross section relies on accurately calculation of all possible final states, and then summing them together as shown in this equation. This is the molecular orbital (MO) theory. However, the accuracy of this strategy is in many cases limited by the explicit description of final states.

The alternative approach is the Multiple Scattering Theory. In this approach, the scattering of photoelectrons is treated as interaction with a series of potentials at different regions. In this scenario, the potentials are divided into flat interstitial regions with constant potential V_{int} and scattering regions with potential δV, by the Muffin tin (MT) approximation. The schematic drawing of this Muffin Tin potential is shown in Fig. 2.4.[23]

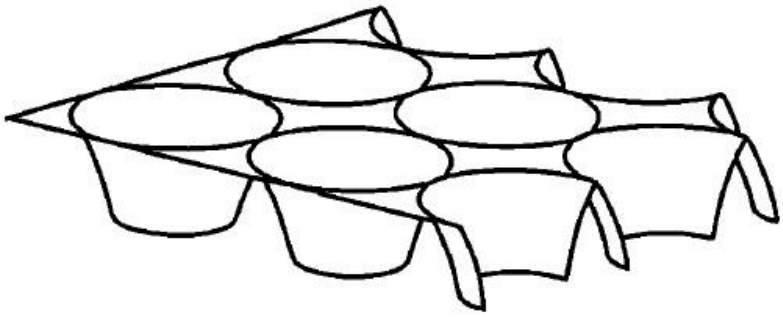

Figure 2.4 Figure for the illustration of the Muffin-tin potential drawn at 2D space. Taken from Ref [23].

The effective one-electron Hamiltonian for the scattering photoelectron is then $H = H_0 + V_{int} + \delta V$ and the propagation of the photoelectron can be treated as a quasiparticle. The one-electron Green's function operator describing electron with energy E can be defined as[24]:

$$G(E) = (E - H)^{-1} \tag{2.5}$$

Based on the spectra representation:

$$\sum_f |f\rangle\delta(E - E_F)\langle f| = \left(-\frac{1}{\pi}\right) ImG(E) \tag{2.6}$$

The golden rule can be rewritten as:

$$\mu \propto -\frac{2}{\pi} Im\langle i|\hat{\varepsilon}\cdot\vec{r}\,' G(\overrightarrow{r'},\vec{r},E)\hat{\varepsilon}\cdot\vec{r}|i\rangle \tag{2.7}$$

The propagator G is related to the scattering via the operator equation $G = G + G^0TG^0$, with $G^0 = (E - H0)^{-1}$ as the non-interacting, free electron propagator and T is the total atomic scattering matrix.

The total scattering matrix can be further expressed in terms of scattering amplitude of each atom by introducing the scattering path operator or τ-matrix[25-26]:

$$T = \sum_{i,j} \tau^{i,j} \tag{2.8}$$

with $\tau^{i,j}$ as the sum of all possible scattering path that begins with atom i and terminates at atom j.

Detailed presentation of the algorithm for the calculation of the interaction matrix would be inappropriate as the focus of this thesis is not theoretical, or based on computational algorithm development. The full calculation of the propagator G is called FMS, and can be carried out with a series of software packages. In this thesis the FEFF9.6[23, 27-28] software package was used for the calculation of the XANES spectra.

2.2 Review of Structural Dynamics in Liquid Phase Probed with Different Methods

A series of experimental methods have been applied to the study of aqueous structural dynamic processes with different spatial and time scales. This section is a brief review of these experiments and the most important conclusion drawn from this work. Each of these methods addresses how 'structured' the aqueous solution can be, and how ions affect the structure.

2.2.1 IR Reorientation Study for The Water Molecules

In these experiments, HDO molecules (in various kinds of solutions) are used as samples. A midinfrared laser is used to excite a fraction of these molecules into a vibrationally excited state of the O-H stretching mode (ν_{OH}=1). This excitation leads to a $\nu = 0 \rightarrow \nu = 1$ bleaching effect and induces increased $\nu = 1 \rightarrow \nu = 2$ absorption. Another pulse is sent to the sample at different time delays to probe the energy and spectral relaxation. With the variation of the probe pulse, several parameters are detected.

The polarization of the probe pulse is set at the magic angle with respect to the pump pulse to eliminate the orientational diffusion effect of the probed molecule. The time-dependent vibrational relaxation of the excited molecule and the time-dependent fluctuations of the OH bond environment , called "spectral diffusion", can also be detected.[6, 29]

If the polarization of the probe pulse is rotated by 45 degrees with respect to the pump pulse, the transmission changes of the probe parallel to the pump [$\ln(T(t)/T_0)_{\parallel}$] and perpendicular to the pump [$\ln(T(t)/T_0)_{\perp}$] can be measured, and then the anisotropy parameter can be calculated[6, 29]:

$$R(t)=\frac{[\ln[\left(\frac{T(t)}{T0}\right)]_{\perp}-\ln[\left(\frac{T(t)}{T0}\right)]_{\parallel}]}{\ln[\left(\frac{T(t)}{T0}\right)]_{\perp}+2\ln[\left(\frac{T(t)}{T0}\right)_{\parallel}}. \quad (2.9)$$

In this equation, the numerator contains signal from the physical effect of molecular reorientation, spectral diffusion and vibrational relaxation. The denominator contains only the effect of spectral diffusion and vibrational relaxation. So after normalization, the anisotropy parameters are an indicator of the orientation effect alone. This parameter is a direct reflection of orientational correlation of O-H vector in a HOD molecule. The reorientation time is considered closely relevant to the hydrogen bonding strength. For instance, in neat water, the reorientation of O-H group bonded to a strong O-H··O bond is slow and vice versa.[30]

This reorientation value (or relaxation time) from the anisotropy parameter is a second order correlation function: $\langle P_2 cos\theta(t)\rangle$. For the neat water without any solute, like HDO in H_2O or D_2O, the decay of anisotropy can be divided into three different time domains. 1) There is a very fast decay after excitation, less than 200 fs, and this decay is generally attributed to the librational motion of water molecules. 2) At intermediate delay times (200 fs to 1 ps), the anisotropy decay strongly depends on the excitation wavelength. The associated dynamics in this time range are interpreted with the simulation technique indicated Large Angular Jump model of water. In this model, it is proposed that the reorientation of a water molecule started with a double bifurcated HB with two other water molecules. The evolution of this state is accompanied with the formation of new HB by the water molecule finding a new partner and a large O-H orientation rotation of ~60°. This event is defined as a switch event.[31] 3) At longer decay times, the anisotropy has a time constant of 2.5ps, independent of the pumping and probe laser frequencies.[32]

Based on this method and quantities listed above, the ion effect on the HB network was studied using $Mg(ClO_4)_2$. In this solution, two kinds of water molecules are considered to exist. The first is water with OD group bonded to other waters and is representative of a water molecule in a bulk environment. The second is a water molecule hydrogen bonded to the anion. These two types of water molecules have different absorption properties, with the water molecules in bulk water peaking at 2500 cm^{-1} and water molecules associated with anions peaking at 2640 cm^{-1}. Thus, by tuning the probing wavelength the reorientation dynamics of bulk water molecules and anion-associated water molecules can be identified separately. Also, Mg^{2+} is believed to be a structure-making ion based on viscosity tests. If the hydrogen bond network is enhanced by Mn^{2+} over a long range, the reorientation time of water molecules in bulk liquid will be longer than that in neat water. The anisotropy parameters R in 0 M, 1 M, and 3 M $Mg(ClO_4)_2$ aqueous solution were measured. It turned out that there is no concentration dependence of water-bonded OD group reorientation dynamics. This implies that the hydrogen bonds in bulk water are not affected by the presence of Mg^{2+} and ClO_4^- ions. This result is further supported by the measurements of orientational dynamics of $NaClO_4$ and Na_2SO_4. Therefore, it has been confirmed that there is no dependence onion identity or concentration of the reorientation time of an OD group bonded to bulk water.

The authors then suggested that ion solutions should not be treated in a homogeneous way, rather, as a colloidal suspension of inert particles in liquid bulk water where the particles are composed of the ion and the first hydration shell. [7-8] Following this assumption, the suspended 'particle' size can then be estimated using the Einstein equation:

$$\frac{\eta-\eta_0}{\eta_0} \approx 2.5\emptyset \tag{2.10}$$

where $\emptyset$ is volume fraction of the sphere. The authors further estimate that the suspended sphere of 'particles' in 1M $Mg(ClO_4)_2$ solution is around 3.6, in agreement with the size of this ion and its first hydration shell.[7]

2.2.2 Dielectric Relaxation Spectroscopy

In dielectric relaxation spectroscopy a small amplitude oscillating electric field is sent to the sample, and the sample's response to this time-dependent field is observed. The electric field will induce polarization of the sample, accompanied by dipole moment reorientation under the field perturbation. This polarization can then be recorded in either the time-domain or frequency domain. In the frequency domain, the response of the sample is expressed as the total permittivity of the sample:[33]

$$\hat{\eta}(\nu) = \hat{\varepsilon}(\nu) - \frac{i\kappa}{2\pi\nu\varepsilon_0} \tag{2.11}$$

where ν is the frequency, κ is the electric conductivity of the sample, and ε_0 is the vacuum permittivity.

The complex permittivity is

$$\hat{\varepsilon}(\nu) = \varepsilon'(\nu) - i\varepsilon''(\nu). \tag{2.12}$$

The real part of the permittivity is the in-phase response of the sample to the external field. This parameter measures the degree of how much the sample polarization is able to follow the change of external field. The imaginary part is defined as dielectric loss, indicating there is an absorption process in the sample. It is a measurement of the out-of-phase response of the sample polarization to the external field.

One of the most important advantages of dielectric spectroscopy is that it can be universally applied to all electrolyte systems, that it can measure the system response for very broad spectrum ranges. The dynamics probed are only restricted by the frequency range limitations of the experimental setup. The mechanisms that are involved in dielectric relaxation are listed in Figure 2.5.

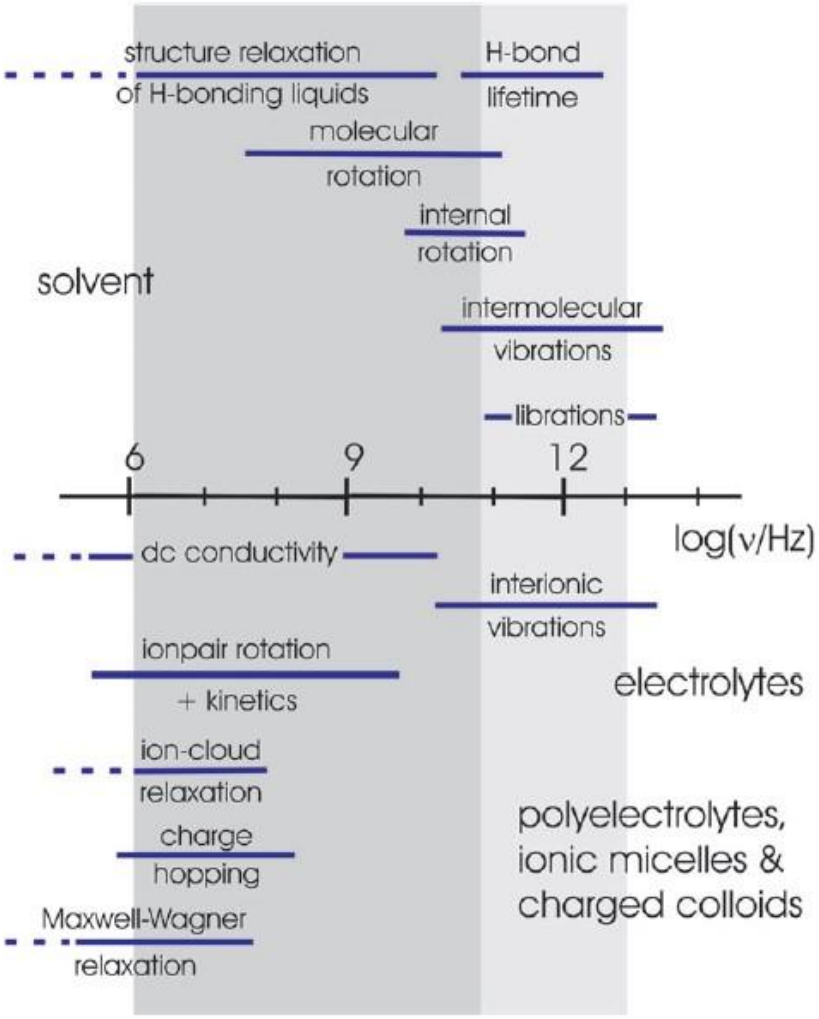

Figure 2.5 Frequency scales for various kinds of dynamics in aqueous solutions This picture is taken from Ref [33].

The detailed information contained in dielectric spectra also make them difficult to analyze. Individual modes contributing to the $\hat{\varepsilon}(\nu)$ generally overlap with each other. Therefore, highly accurate data are necessary for the decomposition of the data.

Despite the data acquisition and analysis challenges of this technique, some very useful conclusions have still been made about the ion effects in aqueous solution from DR spectroscopy. The dielectric relaxation process in aqueous solutions is mainly governed by the cooperation relaxation process of hydrogen bond network. For instance, the 'wait-and-switch' mechanism was

previously proposed as the rate-determining step of dielectric relaxation.[34-38] The more recent Large Angular Jump model essentially holds the same viewpoint. The dipole reorientation of water molecules relies on hydrogen bond network cooperative movement and that the reorientation is finished quickly (tens of femtoseconds) and accompanied by an angular jump (around 60°).[31] Therefore, the dielectric relaxation process can serve as a probe for cooperative relaxation in aqueous solutions.

The dielectric relaxation process in ionic aqueous solutions was then studied with the DR spectroscopy. It is assumed that if the exchange of solvent shell molecules around the ions and the bulk water molecules is slow, there will be some water molecules bonded to the ions in a way that they do not produce any response in the dielectric relaxation. These water molecules are the so-called ‘irrotationally-bound’ (ib) solvent molecules. The number of ib water solvent molecules per salt unit is defined as the ‘effective solvent number’, and is a reflection of the hydration shell structure. Besides the ib solvent molecules, DR spectroscopy also points to a conclusion that there exist a region around solute molecules in side of which solvent molecule relaxation time is distinctly slower than bulk water. This region is the so-called “slow-water” region. The relaxation time value of “slow water” is solute dependent and in the range of 15-30ps based on the current available measurements of various samples.[33, 39-42]

Contrary to the results from IR vibrational spectroscopy that ions have no effect beyond the first hydration shell, DRS studies and simulations show that there do exist perturbation effects on the hydrogen bonding network beyond the second and sometimes even third hydration layer.[43-46]

Buchner *et al.* applied DR spectroscopy to a series of electrolyte solutions and found that the cooperative relaxation times of water molecules in bulk water change with variation of salt concentration, indicating that the hydrogen bond strength in bulk water is affected by the ions. They also provided an equation showing that the cooperative relaxation time of bulk water molecules are correlated with salt concentrations.[39, 41, 47-50] The cooperative relaxation time

dependence on salt concentrations point to a conclusion that DR spectroscopy detects the long-range effects ions can exert to bulk water.

2.2.3 Hyper-polarization Scattering Revealed Long-range Correlation in Aqueous Solutions

One of the most important revelations about ion induced effects based on light scattering experiments was made by D. Shelton. In this experiment, hyper-Rayleigh scattering (HRS) was used on D_2O in KCl aqueous solution. In his publication, it is assumed that the electric field around ions will induce a perturbation effect around the ion and change the orientation of solvent shell molecules such that the local centrosymmetry will be broken. The breaking of symmetry will induce a macroscopic second-order non-linear susceptibility. Then, the scattered light near the second harmonic frequency of the incident laser light beam was measured with incident and scattered light polarization denoted as VH. Here, the scattering plane is horizontal, V denotes that the incident electric field polarization is vertical and the H denotes that the scattered light electric field is horizontal. The physical quantity obtained from the scattering was defined as S/B, that is, the ratio of measured VH HRS spike intensity (S) to the background intensity from the randomly oriented solvent molecules (B). He did find a signal indicated by S/B increasing with KCl molar concentration. His results show that the electric-field-induced second harmonic generation does occur in ionic solutions. The VH HRS spectrum can carry information about long-range effects induced by ions and also indicates the existence of possibility to experimentally measure the static local field factor in polar liquids.[51]

Most recently, more systematic and better time-resolved experiments were done with femtosecond elastic second harmonic scattering (fs-ESHS). In these measurements, the authors sent S- or P-polarized 1028-nm 190-fs 200-kHz laser pulses to the aqueous electrolyte solutions. These laser pulses again induce a second-order polarization, and instantaneously scatter polarized 514-nm second harmonic photons. The second harmonic generated scatter can be from electronic anisotropy within an individual nonspherical molecule. With proper selection of polarization of

incident and scattered light, information reflecting the orientational correlations between any pair of molecules can be extracted. It is shown that structural information relevant to collective orientation can be extracted: $P_{out}P_{in}P_{in}$, $P_{out}S_{in}S_{in}$, where the subscripts denotes whether the light is in excitation or scattered.[52-53] The authors then measured the polarized scattered light intensities of NaCl aqueous solutions with concentration from 1 mM to 0.1 M and compared the intensity

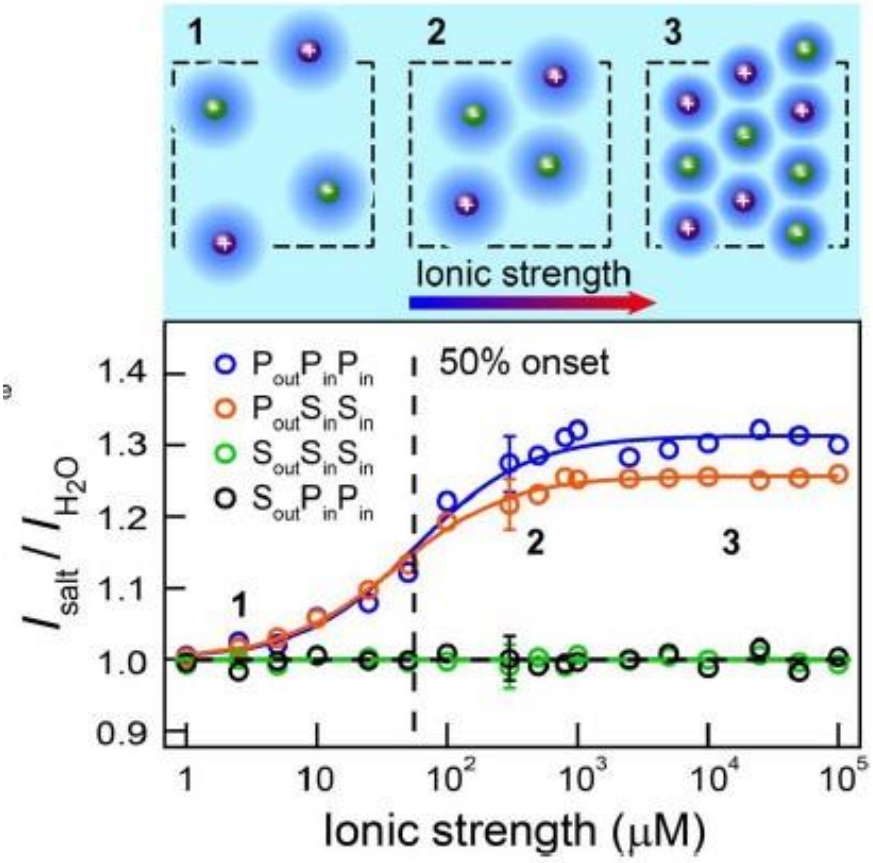

Figure 2.6 Upper panels show that with ionic strength (concentration) increase, domains around each ion start overlapping with each other. Lower graph shows that the scattering intensity from long-range correlation of water molecules increase with respect to ionic strength and then level off due to domain overlapping as shown in upper panel. This picture is taken from Ref [9].

relative to the neat water. The results are plotted in Figure 2.6.

From the lower figure the scattering intensity shows a salt concentration dependence. The intensity levels off at ~1 mM. This effect is attributed to the volumes associated with different ions starting to overlap with each other (as shown on upper figure), producing spatial correlations on the bulk scale. This will saturate the scattering signal and thus no concentration dependence will be detected anymore. Without presenting too much detail here, analysis of the data showed collective orientational order could extend as far as 19 to 70 hydration shells.

Ion-dipole interactions are generally captured by the mean-field description. The Debye-Hückel model was used to explain the data. It turned out that the temperature dependence of the data does not follow the actual measured fs-ESHS scattering intensity. This model failed to explain the saturated response of samples at high concentrations. In order to explain this kind of concentration dependent long-range correlation effect the authors proposed that the orientational order from hydrogen bond interaction also contributes to second harmonic generation in the scattering process. Ions distort the water orientation distribution by ion-dipole interaction changing the hydrogen bond network of bulk water. This argument was confirmed with a simulation by the authors in which both ion-dipole interaction and dipole-dipole interactions were included. Specifically, the authors argued that water-water interactions are very strong over a short distance (involving less than ~100 water molecules), whereas ion induced perturbation effects on the hydrogen bond network are relatively weak and can extend to distances greater than 8 nm. Their simulation box size was limited to 8 nm.[9]

Interestingly, long-range effects were shown to exist in neat water by the HRS technique discussed above. Analysis of the data led to the conclusion that light scattering from neat water is mainly from the transverse polar mode. This mode is the result of small azimuthal bias imposed on the randomly oriented spherical domains with a minimum radius of 23 nm. To explain the origin of this kind of long-range correlation, D. Shelton proposed the existence of a longitudinal-orientational phonon coupling process. In this process, molecular orientation is coupled to

molecular displacement (phonons).[10] This kind of orientation-translation coupling was also found in a Molecular Dynamics simulation of water in nanotubes, which may also be applicable to the case of unconfined water. [54]

2.2.4 Phonon Dynamics in Aqueous Solutions

A phonon is a quanta of collective excitation of atoms in an elastic medium, mostly in solids and liquids and is treated as quasiparticle. Even though it was previously associated with crystals, recent simulation and experimental results indicates that phonons can also play an important role in understanding water structure.

Some progress was made recently in resolving the contradiction between Raman and dielectric/IR spectra of water with Molecular Dynamics simulation. Raman peaks of water were previously interpreted as librational motions of the water molecule-twisting at 435 cm^{-1}, rocking at 600 cm^{-1} and wagging at 770 cm^{-1}.[55-57] Contradiction appears when these interpretations are compared with IR and dielectric data. It is believed that only rocking and wagging motions are IR active, and the twisting motion not. Therefore, only the two higher frequency modes (600cm^{-1} and 770cm^{-1}) are expected to show up in IR and dielectric spectra. However, the two peaks present in IR spectra are at 380 and 665 cm^{-1}.[58] Similarly, peaks show up at 420 and 620 cm^{-1} in dielectric spectra of water.[59] These contradictions put the physical interpretation of Raman peaks into question. By analyzing their simulation data, D. Elton and M. Fernandez-Serra argued that it is not only the single molecular movements that need to be taken into consideration, but also the coherent vibrations of molecules with ranges for as large as 2nm. They argued that the ~435 cm^{-1} Raman peak is a transverse phonon mode and the 770cm^{-1} peak is a longitudinal optical phonon mode. The longitudinal property of 770cm^{-1} mode answers why this peak does not show up in the IR/dielectric measurements since these techniques will only report transverse responses.

In order to quantify the propagation range of these optical phonons, the authors further studied the spatial extent of polarization dipole correlations with respect to frequency by decomposing the spectra into distance-dependent components. In their analysis, R is defined as the distances between molecules taken into consideration, thus the spatial content of the dynamics for spectra analysis. R can be defined as approaching zero limit, which is the single molecular spectra contribution and R can be defined as the maximum of $(\sqrt{3L}/2)$, which is then the full response function for the whole simulation box. They found the emergence of new peaks in both longitudinal and transverse modes with increasing of R. The peaks correspond to the phonon propagation mode, and contain long-range order contributions. The maximum propagation length can be 3nm in their 4 nm simulation box. Actually, this is not necessarily the upper limit for the propagation length because the authors also noted that it is needed to run simulations in larger simulation boxes to further quantify the extent of phonon propagation. Yet, these results have already shown that there is an extended hydrogen bond network for supporting the coherent propagation of these modes.[15]

Another important phenomenon involving acoustic phonons is the so-called 'fast-sound' in liquid water. By both inelastic light scattering experiments and simulation, 'fast-sound' has been proven to exist in liquid water. Acoustic modes propagate usually with a speed of ~1500 m/s in the hydrodynamic limit. Yet, it is measured in the scattering experiment that when the momentum transfer Q reaches the lower limit of 4 nm^{-1}, another acoustic mode excitation arises that propagates as fast as 3000 m/s, known as 'fast-sound'. At the same time, at $Q > 4nm^{-1}$, a dispersionless mode with ~5-meV energy is also identified.[60-61]

To explain this unusual sound speed in water, simulations were conducted using the widely accepted viscoelastic theory proposed. M. Sampoli *et al.* ran Molecular Dynamics simulations of water and checked the water molecules center of mass density fluctuation effects. The results show that there are two regimes that can be divided according to the Q value. In the small Q limit

where Q < 2 nm^{-1}, the acoustic dynamics is purely liquid-like and only longitudinal mode can propagate with normal sound speed. In the $Q \rightarrow 0$ limit, the transverse mode lost its propagation property and becomes relaxational-like. When Q > 4 nm^{-1}, the water is going to behave in a solid-like way and two modes that are similar to the transverse and longitudinal mode in ice can be identified. Even though the dynamics can be compared with ice, the authors also noted that unlike in the pure solid, the pure symmetry characters of both longitudinal and transverse modes in liquid water are greatly lost due to the lack of translational invariance. According to the viscoelastic model of water, the transition from normal sound (low Q regime) to the fast-sound (high Q regime) is believed to happen when the frequency of the sound waves is equal to the structural relaxation time of water. Based on this physical interpretation, the structural relaxation time of water can be obtained by checking the normal to fast-sound transition and this time is measured to be ~0.6 ps.[2, 60-61]

A model different from the viscoelastic model proposed for the explanation of the fast-sound. In this model, it is believed that in the Q = 4 nm^{-1} region, there exist an acoustic and optical-like mode. These models have the same symmetry and it is the repelling between these two models that cause the generation of fast-sound. The fast sound is due to the fact that the interaction between two modes causes a steeper slope of acoustic branch. F. Sacchetti *et al.* showed that this model, even empirical, is adequate to explain their Brillouin neutron scattering data of heavy water. The authors also pointed out that the viscoelastic model does not taken into consideration of an additional scattering intensity at ~6 meV found in the neutron scattering experiments.[62-63] Therefore, more studies are still valuable to have better assessment of different models used for explaining the 'fast-sound' generation.

2.2.5 Water Molecule Split from Multi-Photon Absorption

When water is irradiated with strong enough UV light, electrons are going to be produced by two-photon absorption process, with a hydronium, hydroxyl and a solvated electron produced.

The absorption coefficient for the neat water is measured by Pommeret *et al.* to be around $1.8*10^{-11}$ m/W and the quantum yield is measured to be between 0.26 and 0.33.[64]

$$H_2O+2\hbar\nu \rightarrow (H^+ + OH + e^-)_{aq} \rightarrow H_3O^+(aq)+OH(aq)+e^-(aq)$$

There are solvated electron dynamics on the sub-picosecond time scale, yet all the dynamics except for the electron germinate combination are finished after 10 ps of laser excitation.[65]

The ejection length for Ferrocyanide is around 15 Å. For water, the ejection length depends on the excitation energy. The ejection length is measured to be constant of 15 Å below about 9-9.5 eV and then started to increase with higher energy up to 10.1 eV.[66]

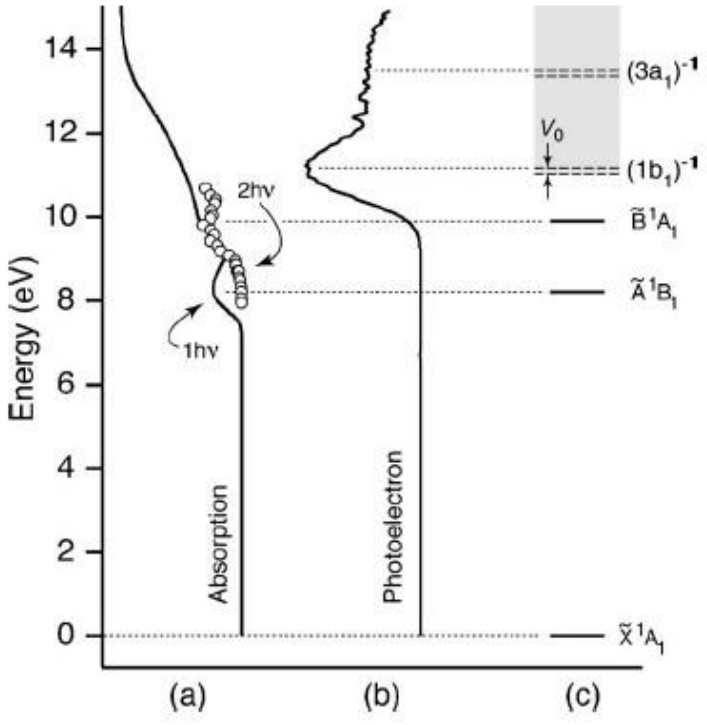

Figure 2.7 Energy diagram showing the water photoexcitation transition process. This picture is taken from Ref [67].

Elles *et al.* drew an energy diagram for the water ionization potential.[67] The first excited state ($\tilde{B}^1A_1$) is the one electron transitions of $1b_1$ nonbonding orbital to the $4a_1$ orbital and the second excited state ($\tilde{A}^1B_1$) is the transition of $3a_1$ bonding orbital to the $4a_1$ orbital. The initially empty $4a_1$ orbital is also described as a 3s orbital of Rydberg state.[68-70] It is measured that the two-photon absorption has a much stronger band for the second excitation than the first one.

The photoelectron experiments show that the energy for directly removing an electron from the highest occupied state ($1b_1$) of water is around 11.2eV. This energy corresponds to the vertical excitation of an electron into the vacuum without giving the electron further kinetic energy.[71] The solvate stabilization energy is calculated to be very small, so the authors estimated that the energy to excite an electron from the valence band to the conduction band is between 11.1 to 11.2 eV. For the excitation energy lower than this threshold, the conduction band can still be achieved by nuclear rearrangements. Here is another graph for the illustration of this process:

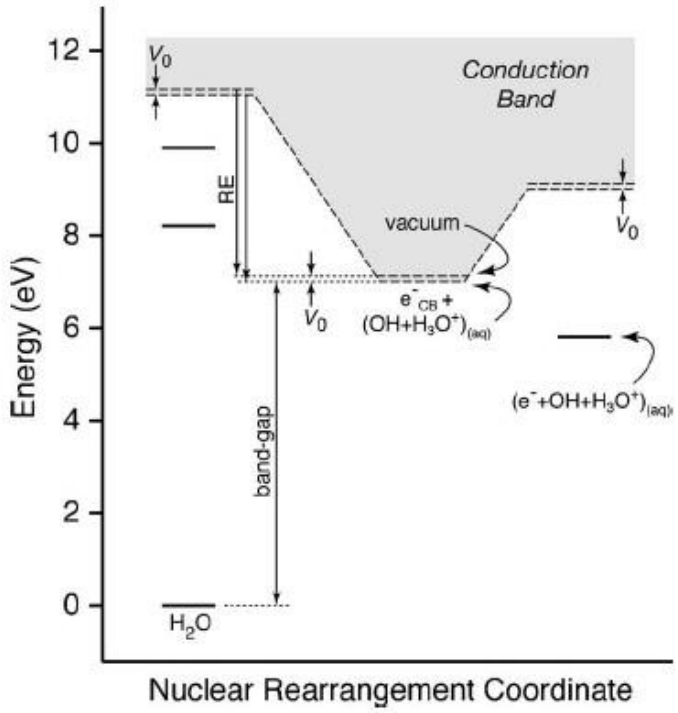

Figure 2.8 Scheme showing the water excitation final states and their relationship with the photoexcited molecules geometry. Taken from Ref [67].

For the nuclear rearrangement motion, as the H_2O^+ is unstable then it will transfer a proton into its neighboring molecule and form hydronium cation and the fully relaxed form of the fully ionized solute is the separated hydronium and hydroxyl radicals. More nuclear rearrangement occurs when the electron is trapped by the solvents from the conduction band to form a solvated electron. All these processes are finished in a few picoseconds.

1. Proton-transfer mechanism: Nuclear motion after molecular excitation enables the system to attain a favorable geometry to transfer an electron into a localized trapped state with energy lower than the conduction band. In other words, the electron can be ejected into a trapped state bypassing the conduction band with this mechanism.

2. Autoionization mechanism: If the excitation energy is higher than the adiabatic band gap, it is energetically possible for the electron to reach the conduction band via autoionization process.

In the gas phase, the electron is ejected into vacuum via autoionization from a molecular excited state. Similarly, in the liquid phase, the electron is ejected into conduction band from an electronically excited molecular state. The rate of the autoionization process is determined by how much the nuclear rearrangement need to take in order for the electron to be transferred into conduction band.

3. Direct ionization mechanism: If the excitation energy is high enough (above ~11eV for water cases), the water molecule is going to behave like an amorphous semiconductor and the electron is going to be excited into the quasi-free state in the conduction band of the liquid without changing the nuclear position of the molecules. Then the hydronium cation is going to decompose in the following step by transferring a proton into the neighboring molecule and the ejected electron is going to be trapped and solvated by other molecules.

Laenen *et al*. also think that since the two water molecules (one in the ionization and one as the neighbor) in the ionization process are in the hydrogen bonding network and the hydrogen bonding between these two molecules may help during the proton transfer process.[72] They also believe that there is an OH:e- complex as an intermediate with a lifetime of 100fs and this complex may also still be hydrogen bonded. Yet, after a few picoseconds should be that, the fully relaxed ionized solute should be in the form that the hydroxyl free radical and hydronium cation are separated after nuclear rearrangement.

2.2.6 Domains in Aqueous Solutions

Another effect solutes can have in aqueous solutions is the formation of domains. It has been shown by Static Light Scattering (SLS) and Dynamic Light Scattering (DLS) experiments that there are inhomogeneities in many aqueous solutions.[73-74] For instance, using DLS, Georgialis *et al.* measured domains in NaCl, $(NH_4)_2SO_4$, and Na-citrate aqueous solutions with hydrodynamics radii up to 500 nm.[12] A more systematic study of these domains was conducted by Sedlak *et al*.

with both SLS and DLS techniques. It was confirmed by these studies that domains contain up to 100 solute-solvent pairs that include both electrolytes and non-electrolytes, and these domains are not a trivial consequence of incomplete mixing of the components.[13-14] These domains are found in millimolar to molar concentration solutions, and are identified as having higher solute concentrations than the rest of the solutions. With the angular dependence analysis of their experimental data, the domain size distribution can be obtained, as shown in Figure 2.9.

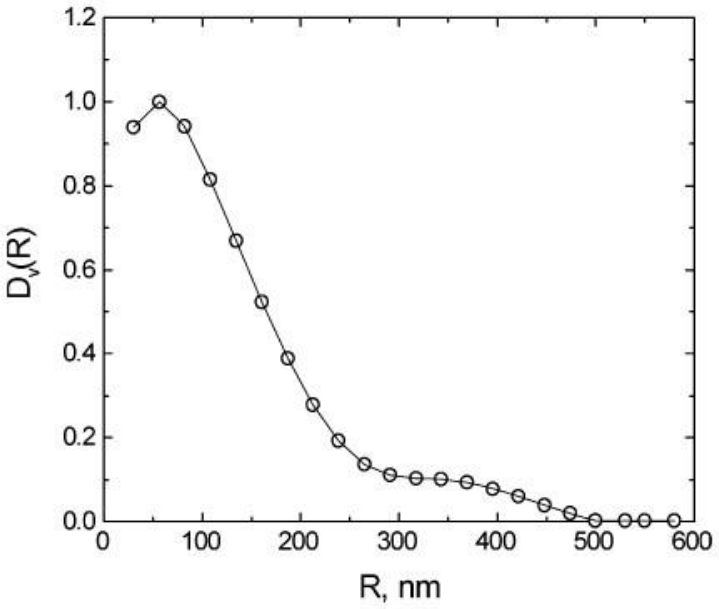

Figure 2.9 Domain size distribution from angular dependence analysis of 10.5 mass % DMSO aqueous solution. Taken from Ref [14].

The stability of these domains was found to be solute-dependent, ranging from hours to months. For instance, the domains in DMSO aqueous solutions are proved to be pretty stable for several months. The domains of NaCl aqueous solutions, on the other hand, grow to their largest size after several hours, then have a decay in domain sizes with a time scale of tens of days.[14]

Another several important conclusions can be made from these systematic studies. Sedlak *et al*. concluded that the formation of these domains relies on the existence of hydrogen bonds in the samples under study. The most likely reason for domain formation is that the domains are hydrogen-bonded networks with both hydrogen bonds between solute molecules and hydrogen bonds between water molecule themselves. Even though the exact concentration of the solutes inside of these domains cannot be obtained from scattering experiments, the domains are thought to be rather a loose aggregates of solutes dispersed among water molecules.[11] An illustration of these domains are shown in Figure 2. 10.

Since the domains exist in various kinds of aqueous solutions, this actually implies that many chemical dynamics of solutes in aqueous solutions need to be reconsidered in terms of these solute domains constituting an inhomogeneous solvation environment.

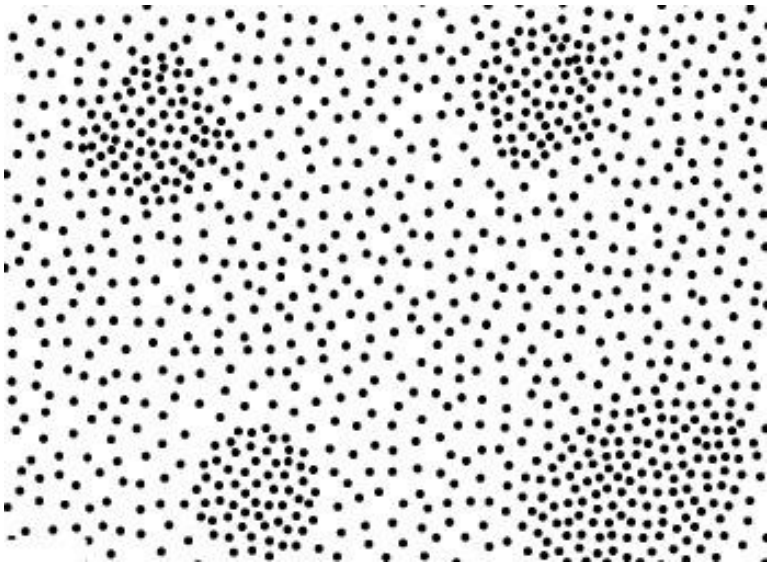

Figure 2.10 Schematic illustration of the "loose aggregates". Solute molecules are shown as black dots. Solvent molecules are assumed to occupy the rest. This is an illustration and is not necessarily exact reality since the solute concentration cannot be determined by the scattering data. Taken from Ref [11].

2.2.7 Inconsistences and Limitations of Results Listed above

Based on the several sections above, a series of inconsistencies can be listed based on different experimental methods.

(1). Whether the ions are really inducing long-range effects. IR vibrational spectroscopy renders the results that the reorientation time of OH bonds in bulk water is solute concentration-independent and the ions, together with the most vicinity hydration shell, can be treated as colloidal suspends in homogeneous liquid water. Yet, the fs-ESHS experiments prove that there are long-range perturbation effects ions can cause to hydrogen bond network in liquid water.

(2). To what extent the phonons can really propagate and how are the modes of these phonons. It can be seen that for the explanation of transition to fast sound, the simulation indicates that the transverse phonon mode can only propagate in large Q region ($Q > 4\ nm^{-1}$). In other words, only high-Q value transverse phonon, with very local feature, can propagate in liquid water. This is somewhat inconsistent with the hyper-Polarization light scattering results showing that there is very long-range water orientation correlation on scales of tens to even hundreds of nanometers.

(3). The hyper-Rayleigh scattering experiments do provide a quantitative correlation length of water molecules in aqueous solutions and the longitudinal-orientational acoustic phonons propagation is considered to be the cause of this effect. Yet, the scattering is still a static measurement of the liquid structure and the real dynamics of such assumed phonons still remain to be observed. Also, simulations do prove the propagation of phonons along hydrogen bonds network, yet the actual propagation lengths remain to be checked due to the limitation of simulation box size, which is generally on the scale of several nanometers.

2.3 Clathrate Hydrates Applied in Electrochemistry

It is well known that the large amount of CO_2 emission into the atmosphere due to consumption of fossil fuels has been not only scientific but also social implications. The

Intergovernmental Panel on Climate Change (IPCC) suggested that in order to maintain the atmospheric CO_2 concentration between 350 and 440 ppm, the CO_2 emissions must be reduced by 30 – 85% by 2050.[75] Except for reducing the emission amount, it is equally important to handle the CO_2 that already has been emitted. Approximately half of all CO_2 will stay in the atmosphere for centuries, if no action is taken.[76] Therefore, capturing and reduction of CO_2 into other useful materials hold particular merit in both environmental and energy aspects.

The pioneer work on CO_2 reduction via electrochemical methods was done by Hori *et al.* in a series of studies with various transition metals. They concluded that copper is the most efficient monometallic catalysts for electrochemically reducing CO_2 to a hydrocarbons including methane, formic acid and ethylene, even though it suffers from the drawback of lacking of selectivity, high over potentials necessary to produce product, and the accompanied hydrogen evolution reaction (HER). [77-79] One approach for minimizing the competing HER is to increase the CO_2 concentration in the electrolyte, generally done by increasing the pressure or reducing the solution temperature. It has been shown that increasing the CO_2 concentration via increasing the pressure does help to suppress HER.[80] Yet increasing CO_2 solubility in liquid phase will render a costly, complicated experimental setup and reducing electrolyte solution temperature will only slightly increase the solubility of CO_2 in water from $0.04\%_{mol}$ at 20°C to $0.1\%_{mol}$ in water at 0°C. [81]

The first successful trial of increasing CO_2 concentration in electrolyte using clathrate hydrates was conducted by our former group members Daniel DeCcicio and Dr. Francisco Schunk. The simultaneous use of clathrate hydrates as an electrolyte and storage medium altered the product distribution of CO_2 reduction relative to similar experiments that did not use clathrate hydrates. Copper foam was used as an electrode material.[17, 82] It was demonstrated by Linga *et al.* that adding THF into the aqueous solution greatly reduces the pressure necessary to form Clathrate Hydrates. Adding $1.5\%_{mol}$ THF into the electrolyte solution will reduce the pressure to form Clathrate from 100 to 10 bar at 0°. [83-84] By adding $10\%_{mass}$ THF into the Potassium

Bicarbonate aqueous solution, D. DeCiccio *et al.* successfully made Clathrate Hydrates with $14\%_{mass}$ ratio in the aqueous solution under pressure only slightly higher than 1 bar of CO_2 atmosphere. With the CO_2 gas molecules trapped in the Clathrate Hydrates cages, high concentration of CO_2 was captured in the liquid. The Clathrate Hydrates solution with high concentration of CO_2 was used as electrolyte for CO_2 electrochemistry reduction, with copper foam electrode made by S. Sen *et al.*[82] The copper foam structure has porous structure and were tested to be mechanically stable during handling and electrolysis. A platinum mesh was used as a counter electrode and Ag/AgCl reference electrode was used as reference electrode. As a summary of their results, the electrolysis Faraday Efficiencies were presented in Figure 2.11.

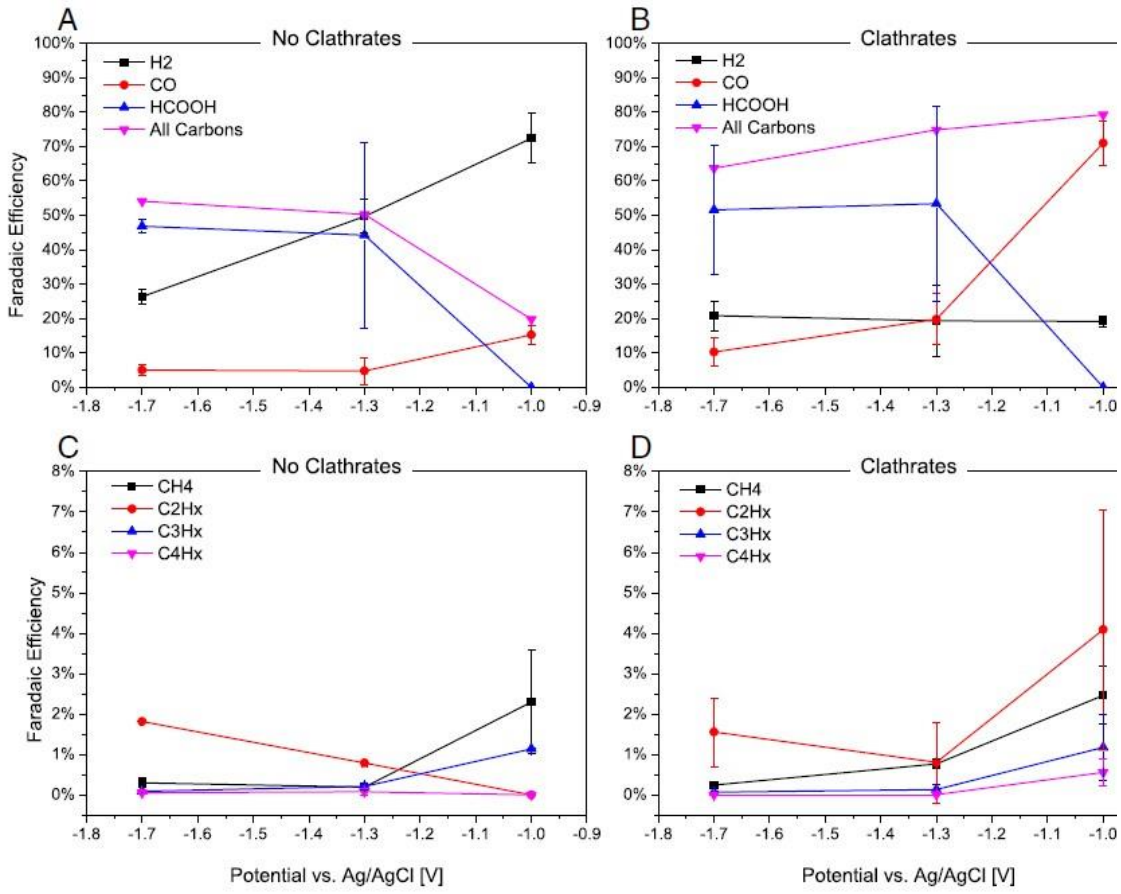

Figure 2.11 Summary of Faraday efficiency of CO_2 electrochemical reducing products with copper foam as working electrode. Panel A and C represent the electrolysis results with no Clathrate Hydrates in the electrolyte solution. B and D present the result with Clathrate Hydrates in solution. The whole results were plotted with reduction potential versus Ag/AgCl reference electrode. The upper frames show the major products and the lower frames show the minor products with expanded scale. This picture is taken from Ref [17].

The experimental results indicate that HER is reduced indicated with decreased H_2 and increased carbonaceous products with the presence of Clathrate Hydrates. The products at relatively high potentials are of special interest because the presence of Clathrate make the largest difference. At -1.0V vs Ag/AgCl, the Faraday Efficiency is measured to be 70% and the Hydrocarbon products are 8% with Clathrate existing in the electrolytes. In comparison, the Faraday efficiencies for CO and Hydrocarbon products without Clathrate Hydrates in the

electrolyte are only 5% and 3%, respectively. In addition, the production of heavier Hydrocarbon products was also found. These results were interpreted by the authors to be the fact that the CO_2 loaded in the Clathrate cages lead to a substantial increase of CO_2 concentration in the electrolyte which will shift the relative rates of electrochemical reduction of CO_2 and H^+ to favor the production of carbonaceous products.[17]

CHAPTER 3. EXPERIMENTAL SETUP AND DEVELOPMENTS IN APS

3.1 Light Source – Synchrotron Radiation

All the ultrafast dynamics measurements were done in the Advanced Photon Source (APS) in the Argonne National Laboratory. The APS is a synchrotron used for the generation of x-ray photons in the experiments discussed in this thesis. Synchrotrons produce radiation by accelerating electrons to relativistic velocities and modulating the velocity directions with bending magnet. One of the most important synchrotron radiation characteristics is the high photon flux at a particular wavelength, or the radiation spectral brightness. Brightness is the radiated power (P) per unit angle (ΔΩ) and per unit area (ΔA):

$$B = \frac{\Delta \mathrm{P}}{\Delta\Omega * \Delta \mathrm{A}} \tag{3.1}$$

and the spectral brightness is defined as the brightness per unit relative spectral bandwidth:

$$B_{\Delta\omega/\omega} = \frac{\mathrm{P}}{\Delta\Omega * \Delta A * (\frac{\Delta\omega}{\omega})} . \tag{3.2}$$

It is more common in the synchrotron community to express the spectral brightness with photon flux (photons per unit time). The photo flux is more generally described with the unit of relative spectral bandwidth set to 10^{-3}, written as 0.1%BW.

Here, the parameters of APS are listed as reference values for a synchrotron. Electrons are emitted by and electron gun. The electrons are then accelerated to 450 MeV by high-voltage

alternative electric fields in a linear accelerator, after which the electrons are injected into the booster synchrotron. When injected, the electrons are further accelerated from 450 MeV to 7 GeV by electric fields in four radio frequency (RF) cavities. When reaching 7 GeV energy, the electrons are travelling at >99.999999% speed of light. The 7-GeV electrons are then transferred into the storage ring, which is a circle with more than 1,000 electromagnets and a 1104-m circumference. The electrons in the storage ring are focused by a strong electromagnetic force into a narrow beam and circulate inside of this aluminum-alloy chamber under a high vacuum of about 10^{-9} Torr. Synchrotrons can have different electron travelling patterns in the storage rings by which their component magnets can be categorized. Earlier synchrotron facilities used bending magnets to keep the electrons moving in a circular path. More modern facilities also employ insertion devices, or undulator/wiggler magnets that force the electrons to undergo a sinusoidal motion as they move through the storage ring. This information is depicted in Figure 3.1. The APS is a modern facility that uses both storage ring and insertion devices. [85]

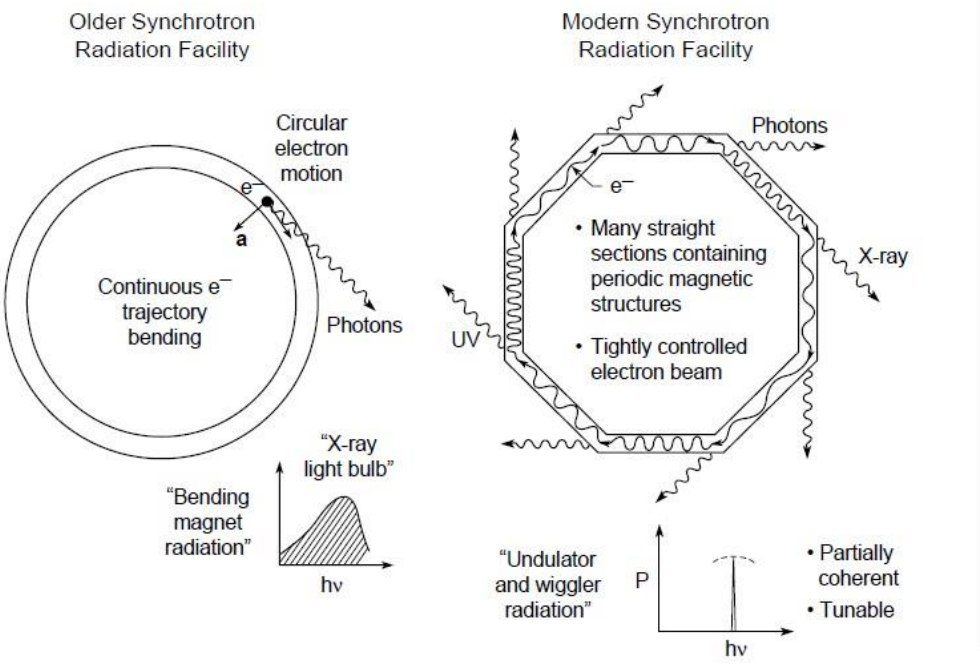

Figure 3.1 Two kinds of synchrotron radiations illustrations. The left one is an early radiation facility with basic circular rings and bending magnetic radiation. The right one is the more modern radiation facilities. In these facilities, the bending magnetic are still being used and photons are produced from the turning electrons from one direction to another. Yet, the periodic magnetic structures are inserted into the straight part as undulators and wigglers. This picture is taken from Ref [85].

The photon radiation generated by bending magnet synchrotrons is illustrated in Figure 3.2.

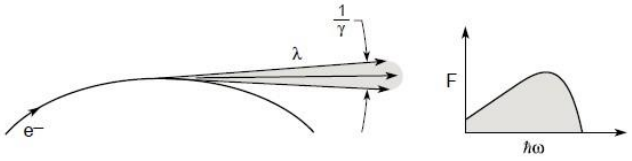

Figure 3.2 Schemes illustrating the radiation cone from bending magnets and its radiated light frequency distribution. Taken from Ref [85].

When a charged particle (here the electron) moves in a curved path it will experience a centripetal acceleration, causing it to emit an electro-magnetic wave. The electrons in the storage ring of a synchrotron are travelling near the speed of light, so relativistic effects must be taken into consideration. Relativistic effects distort the angular distribution of emitted light and narrow the radiation cone in the forward direction with angular spread of $\theta \sim 1/\gamma$, where γ is the Lorentz factor,

$$\gamma = \frac{1}{\sqrt{1-(\frac{v}{c})^2}} \tag{3.3}$$

The equations describing the radiation that results from the use of bending magnets are derived by solving Maxwell's equation for an electron in a uniform magnetic field and at relativistic speeds. The photon flux F_B for bending magnet radiation with electrons moving in a circular path on a given axis can be shown to be[85-86],

$$\left.\frac{d^3F_B}{d\theta d\varphi d\omega/\omega}\right|_{\varphi=0} = 1.33 * 10^{13}\ E_e^2(GeV)\ I(A)\ H_2(\frac{E}{E_c})\ \frac{photons/s}{mrad^2 * (0.1\%\ BW)} \tag{3.4}$$

where θ is the defined in-plane observation angle, φ is the vertical angle with respect to the plane in which the electrons are moving and ω is the radiation frequency. *Ee* is the circulating electron energy and *E* is the emitted photon energy. The function $H_2(x) = x^2 * K_{2/3}^2(\frac{x}{2})$ is a modified Bessel function whose functional dependence on its argument is contained in table

values. The value E_C is the critical photon energy that lies at the center of the photon energy range. r. The critical photon energy can be calculated as:

$$E_C = \frac{3eB\gamma^2\hbar}{2m} \tag{3.5}$$

here B is the magnetic flux density and m the electron mass. The corresponding critical wavelength then can be calculated as:

$$\lambda_C = \frac{4\pi mc}{3eB\gamma^2}\,. \tag{3.6}$$

Bending magnet radiation facilities are the earliest version of a synchrotron. Bending magnets are still used in newer generations of synchrotrons because bending magnets are necessary for keeping the electrons circulating in the storage ring. Radiation produced by the use of bending magnets suffers from a large radiation cone and relatively low brightness in comparison with the later generations of synchrotrons, like undulator and wigglers, as is shown in Fig. 3.3.[87]

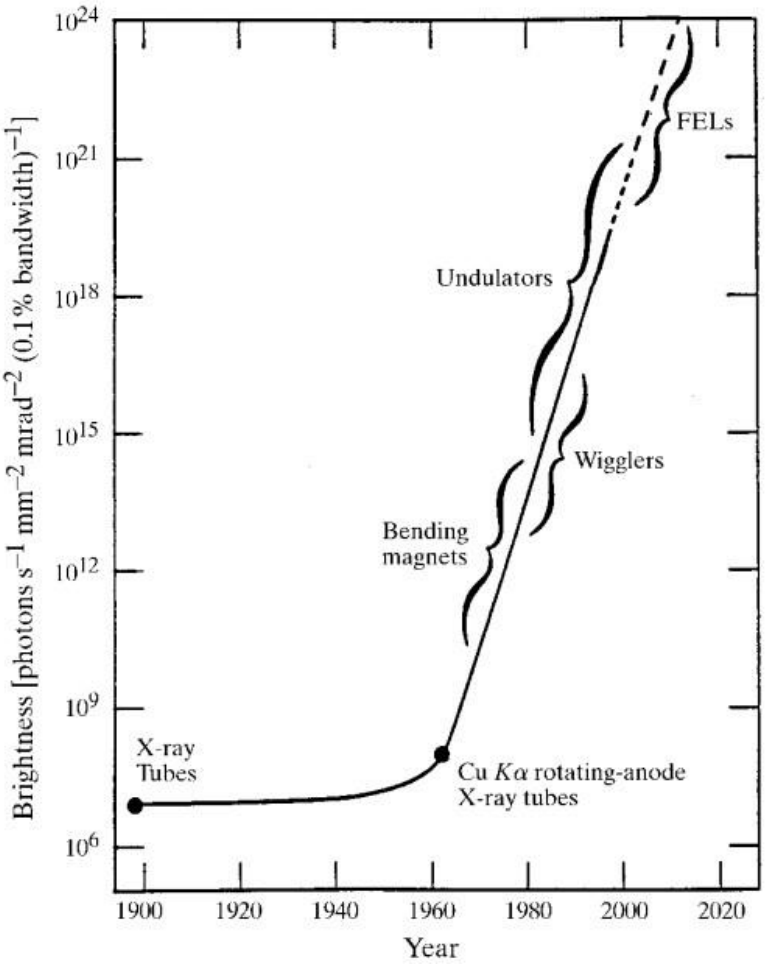

Figure 3.3 Different generations and years of synchrotrons and their performance indicated by brightness. Picture taken from Ref [87].

The undulators and wigglers are inserted into the straight part of the synchrotrons. The most essential feature of these facilities is the periodic dipole magnetics creating an alternating magnetic field. These magnetic fields drive electrons in the storage rings to oscillate in a sinusoidal way, causing radiation to be emitted., This process is depicted in Figure 3.4.

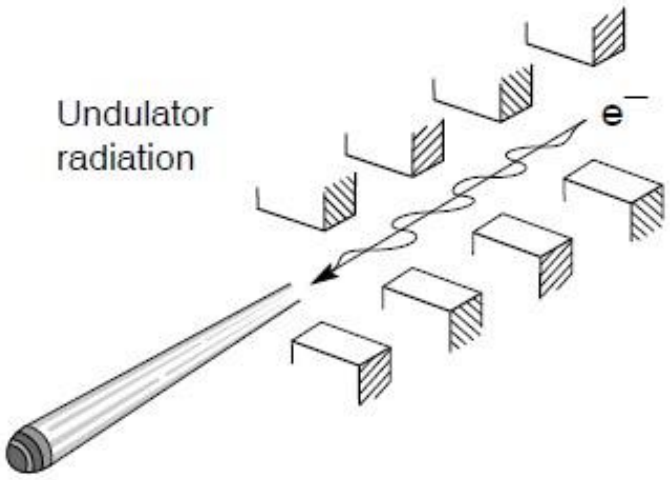

Figure 3.4 Schematic illustration of the electrons moving in the alternative magnetic fields with undulator radiation as an example. Picture taken from Ref [85].

The most important factor characterizing radiation produced by the use of undulators and wigglers is the deflection parameter K

$$K = \frac{eB_0\lambda_u}{2\pi mc} \tag{3.7}$$

with λ_u as the magnet period.

When the electrons are travelling in these periodically positioned magnets, cone radiation is emitted during each sinusoidal oscillation period. For different K values the radiated cones are going to overlap and interfere in different ways, leading to different spectral properties. The motion of an electron in such an oscillating magnetic field is shown in Figure 3.5.

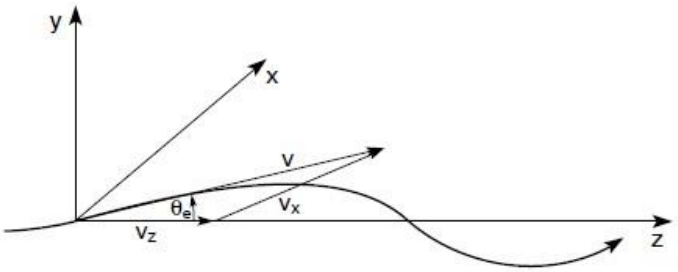

Figure 3.5 Illustration of electrons moving in the periodic dipole magnets in a sinusoidal way. Picture taken from Ref [85].

In Figure 3.5 electrons are moving in a sinusoidal way. The angular excursions are harmonic with maximum excursion K/γ. In the undulator case, K is smaller than 1 and the angular excursions are small, leading to a smaller cone of radiation. In this scenario the interference effects between the cones of radiation are intensified, spectral brightness is higher and sometimes there is partial coherence between the cones. When wiggler magnets are used, K>>1 and there are no such interference effects.

The observed wavelength produced by an undulator can be shown to obey the so-called undulator equation,

$$\lambda = \frac{\lambda_u}{2\gamma^2}\left(1 + \frac{K^2}{2} + \gamma^2\theta^2\right). \tag{3.8}$$

The equation is essentially a description of the fundamental photon production. The transverse oscillation of electrons introduces higher harmonics into the motion. When the K-values become larger, e.g. $K \geq 1$, higher harmonics are going to be produced due to continued mixing of harmonic motions. The observed wavelength including higher harmonics can be described by the extended undulator equation,

$$\lambda_n = \frac{\lambda_u}{2\gamma^2 n}\left(1 + \frac{K^2}{2} + \gamma^2\theta^2\right). \tag{3.9}$$

When K continues increasing, this mixing will finally lead the system into a non-sinusoidal wiggler limit. The wigglers are essentially equal to the sum of separate x-ray sources like for a bending magnetic source. The wigglers produce a larger cone of radiation with intensity 2N times higher than that produced with a bending magnet because the electrons are bent 2N times in the wiggler in comparison with the bending magnets.

3.2 Time Resolved Signal Detection- Streak Camera

The time-resolved signal measurements can be achieved with a streak camera used for detection. A simplified scheme is shown in Figure 3.6. Streak cameras are instruments used for detecting electrons or photons with optimized ultrafast time resolution. Detection occurs within a short time window triggered by a photoconductive switch. X-rays enter the system through a beryllium window and hit a photocathode. A photoelectric current produced by the photocathode has intensity proportional to the x-ray light intensity. These photoelectrons are then accelerated in a 1-mm gap between the photocathode and a stainless steel foil with a 3-mm horizontal by 10-micron vertical slit in it. The acceleration was accomplished with an electric field produced by keeping the photocathode at -5kV and the stainless steel foil grounded. The electrons then go through sweeping plates subjected to a voltage ramp precisely synchronized with the moving electrons. Synchronization details will be discussed in the sections that follow. Electrons are deflected in the transverse direction with respect to the direction of electron movement. The deflected electrons are then focused to a CCD detection chip by an electron lens. By deflecting the electrons the photocurrent carried time-dependent information is mapped into spatial coordinates recorded by the CCD chip.[88-89]

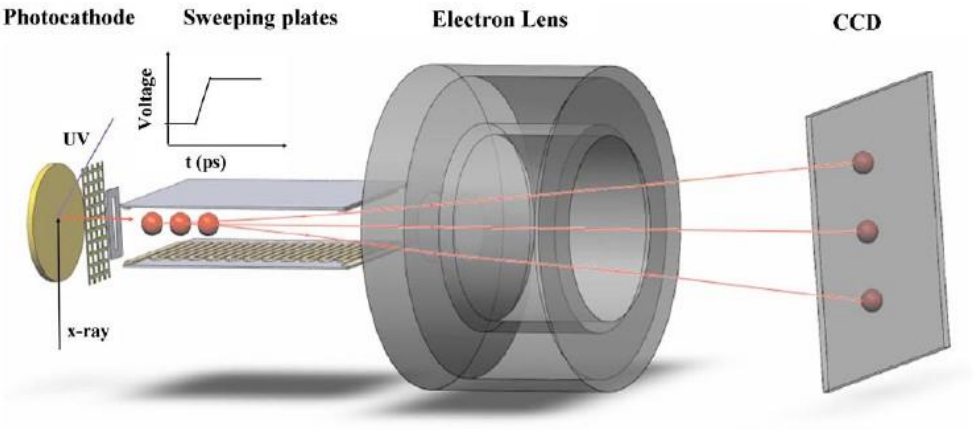

Figure 3.6 Scheme of Streak camera. Picture taken from Ref [88].

The time resolution and detected signal quality of the streak camera is greatly impacted by the choice of photocathode material. The time resolution is determined by the spectral bandwidth of the emitted photoelectrons. The signal statistics are determined by the photocathode quantum yield. In our experiments an alkali halide photocathode was used. The photocathode was made of a 120-nm cesium iodide film on 100-nm thick piece of aluminum, which is on a 100-nm Lexan thin foil. It was experimentally proven that this photocathode provides considerably higher secondary electron yield than metal photocathodes, like Al and Au, for photon energies between 1 and 10 keV. [90]

The deflection plates were made from a 1.74-mm thick FR4 circuit board with a 3.34-mm wide meandering microstrip as is shown on Figure 3.7.

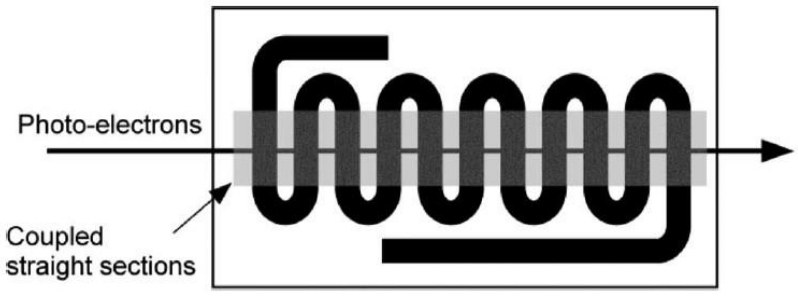

Figure 3.7 The meander microstrip line to create a deflection voltage with sweeping speed match the photoelectron propagation speed between the deflection plates. Picture taken from Ref [89].

The microstrip has an impedance of 50 Ω, and the effective permittivity was calculated to be 3.26 by the equation:

$$\varepsilon_e = \frac{\varepsilon_r+1}{2} + \frac{\varepsilon_r-1}{2}\left(1 + 12\frac{H}{W}\right)^{-1/2} \tag{3.10}$$

where ε_r is the substrate relative permittivity, H is the substrate height and W is the width of the microstrip. The electron propagation speed between these two plates was estimated to be ~$166*10^6$ m/s by dividing the speed of light by the square root of the relative dielectric coefficient of the medium. The signal propagation speed along the coupled straight sections of the strip lines was then calculated by dividing the propagation speed between the plates by 4, as the signals travels four times along the strip lines comparing to the distance between two coupled straight sections. The signal propagation along the coupled straight sections was estimated to have a speed of $42*10^6$ m/s, which matches the 5-keV photoelectron speed (0.14c). Photoelectrons arriving at the deflection plates at different times will be deflected into different angles along the vertical direction. Again, the deflection plates convert temporal into spatial information.

3.3 Optics and Timing Synchronization

3.3.1 X-ray Optics

In order to create the dynamics presented in this thesis (acoustic phonons in aqueous solution discussed in Chapter 5), the laser power density must be sufficiently high after conversion to 266 nm from the 800 nm radiation provided by APS. The laser beam must be focused to increase power density. It was found that the laser needed to be focused to a spot smaller than 100 μm. In order to guarantee that the x-rays probe the laser induced dynamics uniformly, the X-rays needed to be focused to an even smaller spot of ~30 μm. The limited size of the entrance slit of the streak camera add further restrictions on the x-ray spot. In our case, the slit was 25 μm high by 3 mm wide, located 75 cm downstream of the sample. Since the dimensions of the slit are quite different between the vertical and horizontal direction, the focusing of X-rays can be solved with different strategies. Another factor that must be taken into consideration is chromatic dispersion. There are some cases that an energy scan needs to be conducted over an energy range wider than 100 eV. The focal length of the lens must be adjusted for all of the X-ray wavelengths used in the scan. The overall scheme of the X-ray optics is shown in Figure 3.8.

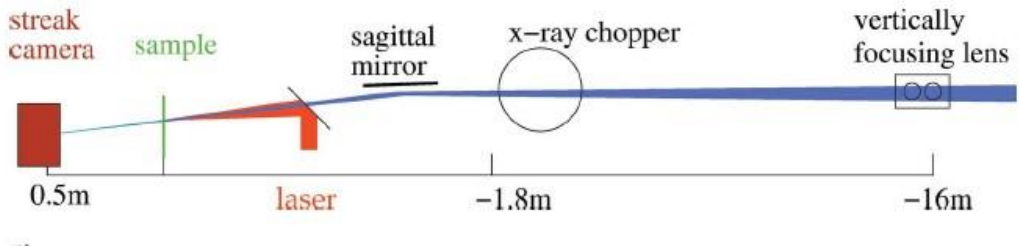

Figure 3.8 Illustration of the optical setup for x-rays. The most important components are a sagittal mirror, an x-ray chopper and a vertically focusing lens. From Ref [92].

The vertical focusing problem was tacked by using a cylindrical lens that consisted of a block of Be metal and two 1mm diameter cylindrical holes drilled into it. The lens was placed at distance of 16 m upstream from the sample, in the 7IDB hutch of APS. The scheme of the lens was shown in Figure 3.9. [91]

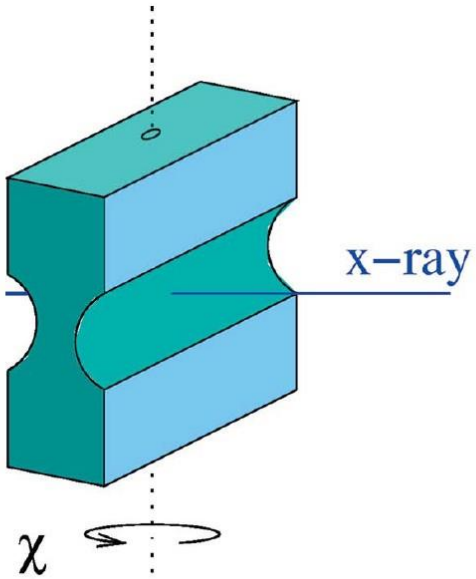

Figure 3.9 Schematic view of the lens used for focusing x-ray on the vertical direction. Taken from Ref [91].

When this cylindrical lens is rotated by an angle χ in the axis perpendicular to the X-rays and cylinder axis, a scaling factor 1/cosχ is induced in the amount of lens material in the beam. By rotating the lens the effective number of component lenses can be continuously varied. The vertical focus was optimized for sample location maintained when varying the X-ray photon energy.

The focusing of the X-ray beam in the horizontal direction was achieved by a sagittal mirror. The mirror was placed 1.2 m upstream from the sample. The mirror has a cylindrical surface with

a radius of curvature of 4 mm. The sagittal mirror is also used for suppressing third and higher harmonic photons nominally selected by the beamline monochromator.

In our experiments, the x-ray repetition rate from the synchrotron is much higher than the laser repletion rate. Therefore, most of the x-rays are not useful for accumulating data. The extra bunches of x-ray photons not overlapped with the laser pulses may introduce adverse effects, such as sample and streak camera photocathode degradation. An X-ray chopper that opens for 2 μs every 200 μs was used to produce a 5-KHz repetition rate single high-current x-ray pulse that is overlapped with laser pulse. The x-ray chopper was placed 1.8 m upstream from the sample between the two focusing elements.

3.3.2 Laser Optics and Streak Camera Triggering

In the experimental setup the laser serves to pump the sample and trigger the sweeping voltage between the deflection plates. The laser used consisted of a Ti:sapphire laser oscillator (Coherent Mira), and a Coherent Legend type regenerative amplifier pumped by a Coherent Evolution laser. The oscillator had an 88-MHz repetition rate, and was phase-locked to the APS master clock. The laser was placed in a separate room about 20 m from the experimental hutch. The setup scheme is shown in Figure 3.10.

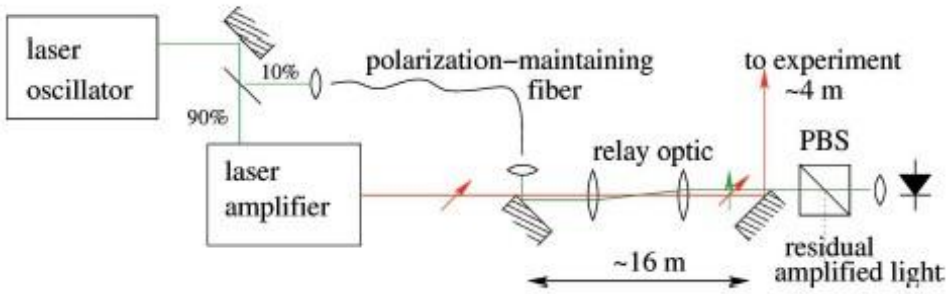

Figure 3.10 Scheme of the laser optics setup. Here, the main amplified laser pulses and 10% split pulses were not only geometrically separated, a PBS (polarizing beamsplitter) was also used to suppress the main laser signal on the photodiode. From Ref [92].

As shown in Figure 3.10, the laser was split into two parts. 90% of the oscillator beam was sent to amplifier. After regenerative amplification, the laser light was directed to the experimental hutch, frequency-tripped from 800nm to 266nm with two BBO crystals and then used for pumping the sample. The pulse was focused to a 70-μm spot with a pulse energy of 20 μJ.

In a previous design, a photoconductive switch was used to read about 30% of the laser pulse energy in order to trigger the voltage ramp applied to the deflection plates. Even though a large amount of laser energy was used to saturate the switch in order to reduce jitter from laser pulse energy fluctuation, there was still remaining jitter of up to 10ps. In the current experimental setup, 10% of pulse energy from oscillator is captured by a thin-plate polarizing beamsplitter, which does not significantly broaden the oscillator pulses before they enter the amplifier. The 10% pulses were focused into a polarization-maintaining fiber. The light in the fiber was sent to the experimental hutch in parallel with the 90% main laser pulse at a crossed polarization to it. The 10% pulse was passed through a spatial filter, the 90% pulse was suppressed with a polarizer and then the 10% pulse was focused onto a Teledyne Judson Technologies type No. J22-18I-R40U InGaAs photodiode. The photodiode has about 50-ps rise time and 40-μm diameter activate area. Even though the polarization-maintaining fiber broadened the laser pulses, the broadening was less than the photodiode resolution and the oscillator beam did not show any recognizable spatial-

mode or power fluctuations under normal operations. Signal from the photodiode was then amplified with a chain of microwave amplifiers ended with a pair of 30W broadband power amplifiers (RF Lambda model RAPA0M3GW50) used to drive the deflection plates. The amplified signal continued travelling through 50-Ω coaxial lines to a pair of 40 dB, 50 W attenuators with output to an oscilloscope to monitor the signal pulses. The setup for the streak camera deflection plates triggering was shown in Fig. 3.11 and the signal on the oscilloscope was shown in Figure 3.12. During operation, we found that a deflection voltage of $\pm 25\,V$ was

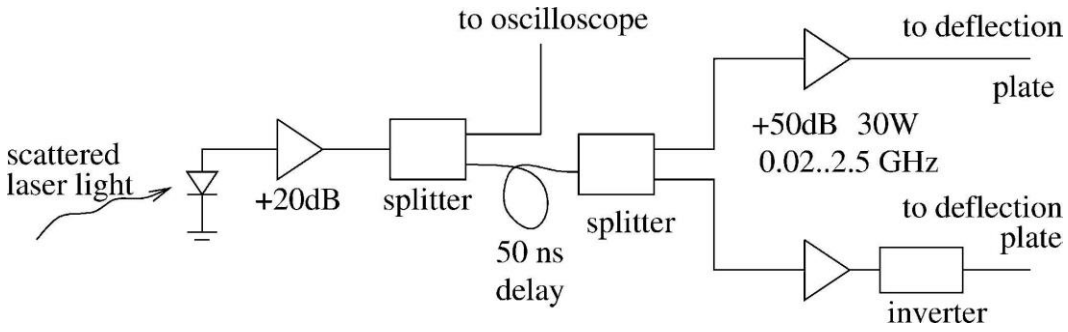

Figure 3.11 Scheme of the microwave amplifier collecting signal directly from laser oscillator and then trigger the streak camera deflection plate after microwave amplification. From Ref [92].

sufficient to deflect the 5-keV electrons from the photocathode.

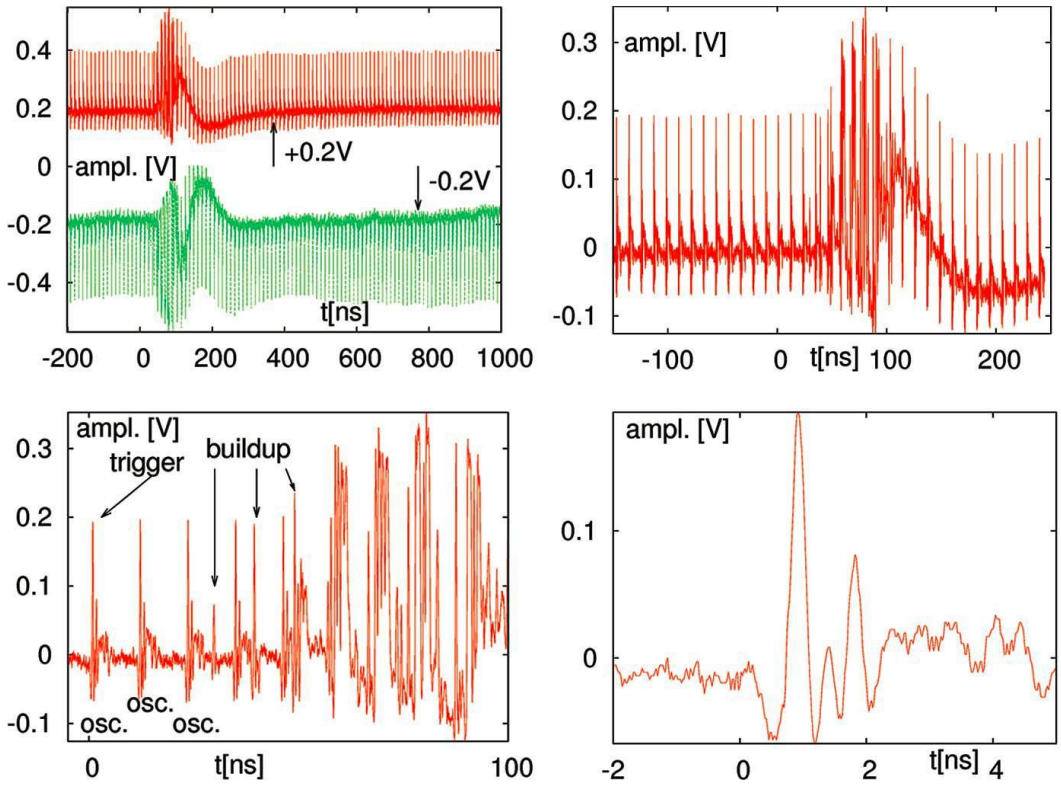

Figure 3.12 Signals presented by oscilloscope after deflection plate. Deflection voltages on both plates after attenuation were shown on the upper-left panel. More details were shown in the other three panels. From Ref [92].

In Figure 3.12 the signal is seen to have an 88-MHz repetition rate. The repetition rate is due to some residual light from the main laser beam reaching the photodiode even though spatial filtering and polarization suppression were conducted. The trace indicates that it is important to use one of the undisturbed oscillator pulses before the pulse overlapped with the x-rays, which is the reason why a cable worthy of 50 ns decay was used, as was shown in Figure 3.11.

3.3.3 Timing Consideration and Data Readout

The microwave signal from the APS master clock cannot can't fulfill the requirement of 2-ps time-resolution we want in our experiments, because the timing relationship between the laser and the APS RF is long-term stable to only 20 ps. The timing relationship between the laser-oscillator pulses driving the deflection plate and the laser used for pumping the sample is determined only by the optical path of the experimental setup, and is stable to better than 1ps. The timing relationship between the oscillator and amplified pulses was used in the experimental data acquisition. The x-ray pulses may drift relative to the laser pulses. This doesn't matter because all the drift does is changing the x-ray intensity of a fixed event sequence, and drift related artifacts can be eliminated by proper normalization of streaked signal traces. Streaked reference traces are used to normalize way drift artifacts, which will be discussed further. The schematic timing diagram is shown is Figure 3.13.

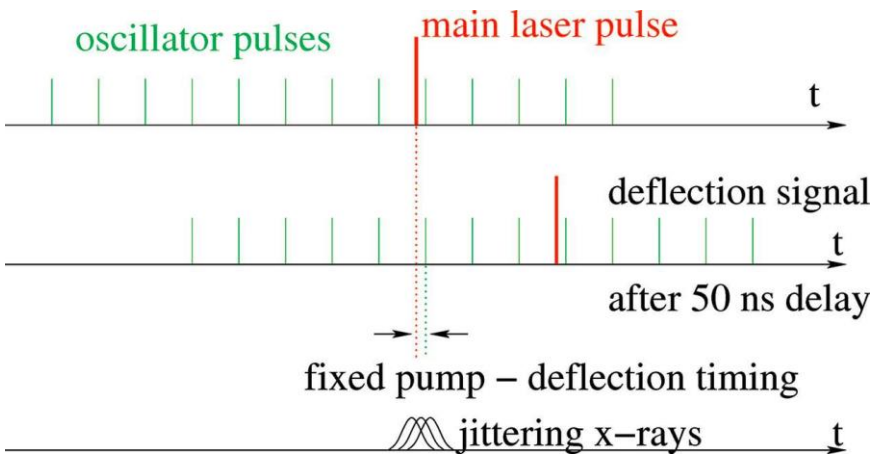

Figure 3.13 Timing diagram of signal pumping, streak camera deflection plates triggering and x-ray pulses. From Ref [92].

The aim of the timing is to synchronize the pump laser pulses, the deflection voltage pulses in the streak camera and the signal probing x-ray pulses. The laser oscillator is phase-locked to the

APS master RF clock using an adjustable phase shifter. The deflection of the streak camera is derived from the oscillator timing. The amplified pump laser pulses are also controlled by the oscillator timing because the optical path in the amplifier is fixed. The strategy to get temporal overlap for these three pulses is to adjust the electronic phase shifter, and derive the deflection voltage from oscillator pulses, to yield a well streaked X-ray pulse image. A well streaked x-ray pulse image is an indication that the laser oscillator pulses are overlapped with the arriving X-ray pulses. The schematic setup for temporal synchronization is shown in Figure 3.14.

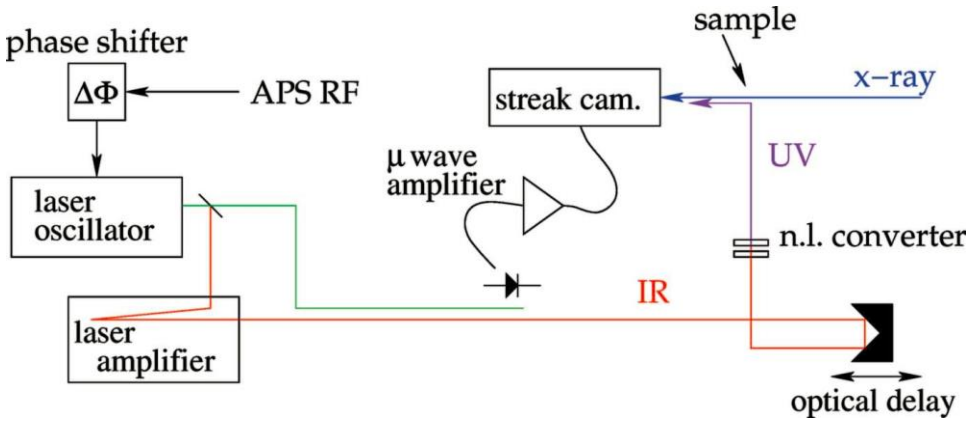

Figure 3.14 The schematic components for timing synchronization. From Ref [92].

More details need to be clarified about the optical path of the amplified pump laser since this is used for timing calibration in the data processing procedure. Before tripling the frequency of the amplified laser beam, the amplified laser beam was routed through an optical delay composed of a retroreflector on a translation stage shown in Figure 3.14. The delay can be adjusted to change the timing between the pump laser and the probing X-ray pulses at the sample location. The UV-light can also be streaked onto the streak camera. An example is shown in Figure 3.15.

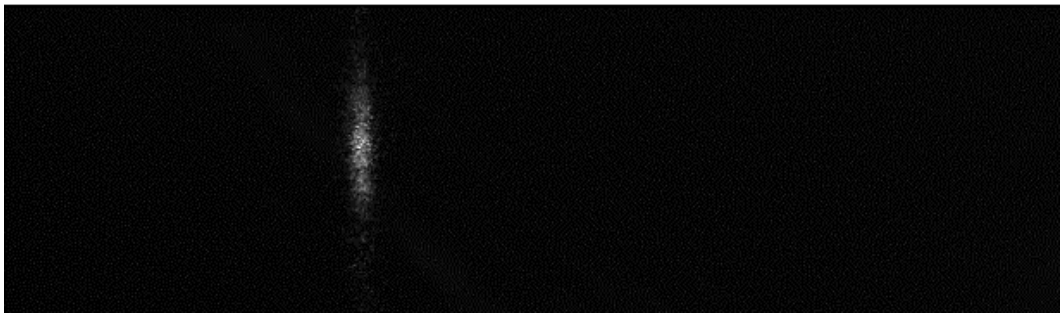

Figure 3.15 Streaked UV pulse, shown as a vertical line on the image. The position of this vertical line is a reflection of Timing of the pulse.

The position of this straight line in the image is an indication of the laser timing relative to the X-rays. With the proper alignment (discussed in Section 3.4), the laser and X-ray pulses traveled from the sample to the steak camera in a collinear way. As a consequence, the relative timing recorded on the streaked image is the same as the timing of laser and x-ray hitting the sample. The optical delay can be adjusted by moving the translation stage on which the retroreflector is placed. A change in the optical delay causes a change of the UV-pulse timing, which provides the time axis along the streak. A composite of streaked UV straight lines produced by moving the reflectometer in 1-mm steps (corresponding to a 6-ps time step) is shown in Figure 3.16.

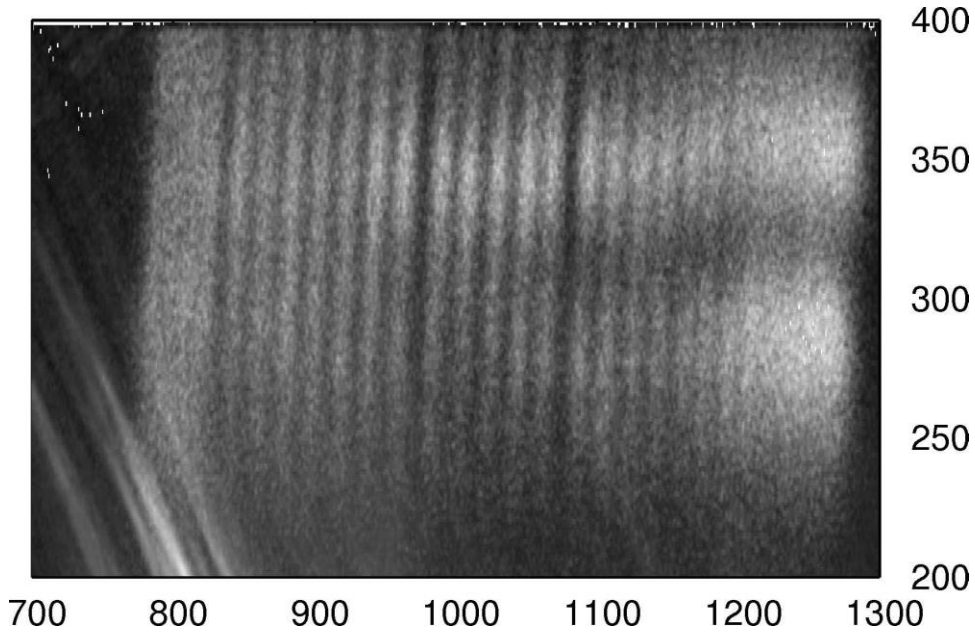

Figure 3.16 Composite of streaked UV pulses. Between two adjacent vertical straight lines, the time interval is calibrated to be 6ps. From Ref [92].

The acquisition of the streaked electrons in the streak camera was done with a thermos-electrically cooled Princeton Instruments Pixis 400B CCD camera, inside of which an in-vacuum back-illuminated CCD chip is directly exposed to the electrons. The streak camera system was able to detect a 0.1% transmittance change of the X-ray flux with data acquisition time of several minutes. The overall data acquisition scheme, with all important components shown, is summarized in Figure 3.17. [92]

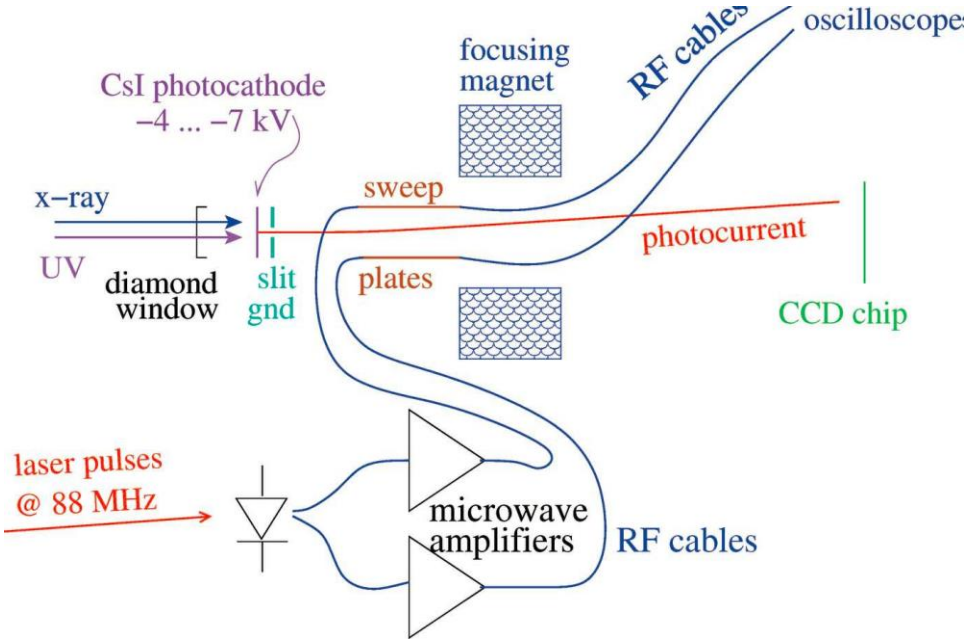

Figure 3.17 Overall Scheme for the data acquisition setup. From Ref [92].

Another factor that needs to be taken into consideration is gating-out unwanted X-rays. Gating is addressed by adding two secondary reflection units that can send electrons not required for data acquisition to a grounded metal plate. The main deflection unit used for streaking is located halfway between the entrance slit and the magnetic lens. The two secondary deflection units were installed 20 cm after the lens. The first secondary deflection mechanism is a pair of Helmholtz coils, and the second secondary deflection mechanism is a set of four electrostatic deflection plates. These plates were rotated 45° to account for the lens induced image rotation.

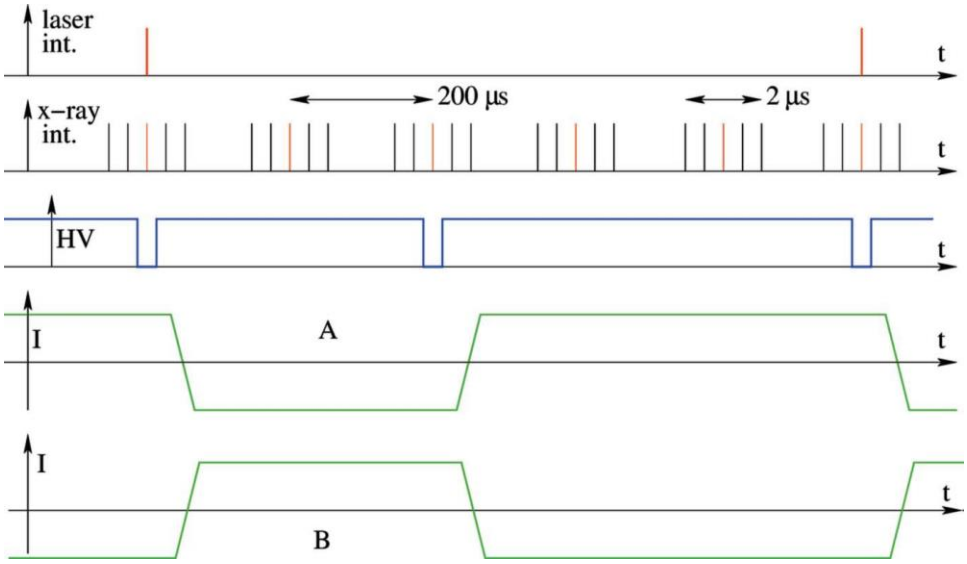

Figure 3.18 Timing diagram. Upper most is the laser pulses once per millisecond. Second one is the X-ray pulses passing the chopper, 2μs one bunch of X-ray pulses bursts for every 200μs. The third one is the High Voltage (HV) gate. Fourth and fifth one is the two patterns of current in the Helmholtz coil to switch the signal and reference streaks on the image. From Ref [92].

The secondary electrostatic deflection units are used for centering the streaked image position on the CCD chip as a static bias as well as gating during data acquisition process. Two of the secondary reflection plates are for bias along the streak and one for the transverse direction. These are operated at voltages between 100 and 200 V. The fourth plate is applied with 800-1000 V voltage and is used for shifting the whole streak away from the CCD chip and shoot all the electrons to the grounded plate. The probing X-rays for data collection are then gated in by setting the voltage to 0 V for 120 ns, which is less than the bunch spacing if 24-bunch mode of APS is assumed. The Helmholtz coil is used to deflect electrons into the direction orthogonal to the streak direction in order to create a reference streak. The creation of reference streaks is very important to detect reliably signal changes as small as 0.1%. When the image collection was done by taking successive exposures, the images suffered from statistical problems caused by subtle fluctuations, like the liquid jet flow thickness and possible x-ray flux fluctuation. These problems were settled by streaking the X-ray pulses almost simultaneously with the laser from otherwise

unused X-rays passed by the chopper in the same bunch. The timing strategy is shown in Figure 3.18.

As is shown in Fig. 3.18, the X-ray chopper opens and permits the passage of X-rays for 2 μs every 200 μs. Among the five pulses in each set of x-ray pulses allowed through the chopper, only one pulse is synchronized to the laser and carries a pump-probe signal. The other four pulses can then be used to create the reference streak. With this strategy, all possible fluctuation induced artifacts can be reduced and we successfully obtained signals that are going to be discussed in detail in Chapter 5 and Chapter 6.

To account for possible inhomogeneities on the CCD chip and slight differences between the upper and lower streaked traces, the Helmholtz coils were operated such that the 'signal streak' and 'reference streak' were altered periodically. All possibly remaining artifacts can be removed in the subsequent data processing step. One sample of a double streak image is shown in Fig. 3.19.

Figure 3.19 Sample data image with one streaked X-ray trace containing pump-probe signal and one streaked trace used as reference trace.

3.4 Instrument Atomization of Laser-X-ray Spatial Alignment

As is shown Fig. 3.8, the X-ray optics can be as far away from the sample as 16 m. The laser was located in a separate hutch 20 m away from the sample and the streak camera. In order to guarantee sufficient pumping intensity, the laser needed to be focused on the sample with a 70 by

70-µm spot, and the X-ray spot needed to be 30 by 30-µm to ensure that the X-ray spot was contained within the laser. These very small spot sizes in conjunction with the long laser and X-ray optical paths made the laser X-ray alignment very challenging Since all experiments were conducted in a closed beamline hutch, all the instruments had to be controlled remotely from outside the hutch. These challenges were addressed by the development of a laser steering system, a sample circulation chamber, and other components that could all be controlled by a computer running the LabVIEW software package. After the laser light was frequency tripled to 266 nm it was sent through a specifically designed periscope box that could steer the laser beam onto the sample. During the operation of the experimental apparatus the X-ray path was defined first. To this end, using the vertical lens, chopper, and sagittal mirror the X-ray path was adjusted until it was sent through the sample and well-streaked. Then the laser beam was adjusted until it propagated collinearly to the X-ray beam while passing through the sample. The overall Laser-X-ray beam overlapping optics is shown in Figure 3.20.

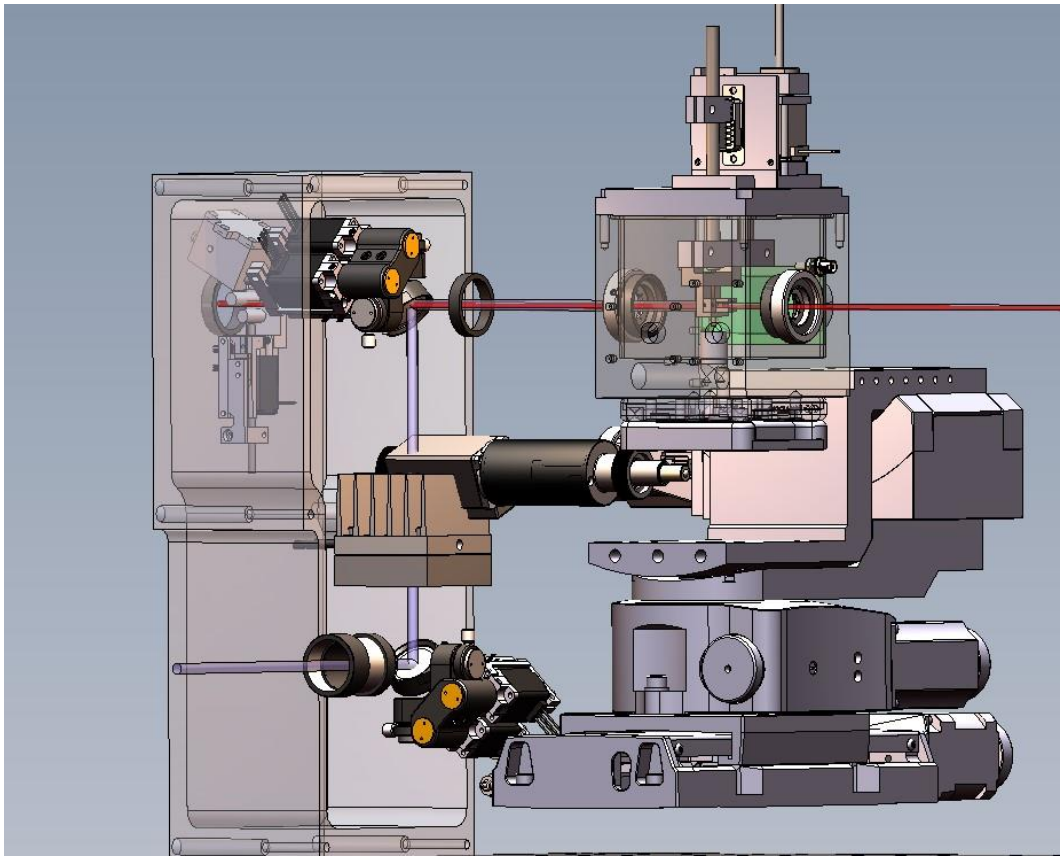

Figure 3.20 Scheme of the periscope box used for steering the laser beam path and the sample chamber. The Left components is the periscope box and the upper right component is the sample chamber inside of which the measured sample solution was circulated. The lower right component is the kinematic stage that the chamber sits on. The kinematic stage can be used to align the sample beam with the laser and x-ray.

In Figure 3.20 the purple light beam represents the laser and the red beam is the X-rays. By passing through two BBO crystals the 800-nm laser light was converted to 266 nm, the frequency tripled laser was then sent into the periscope box from the bottom of the box. The laser beam was reflected off of two mirrors and then aligned with the x-ray beam, which was then sent to the sample chamber shown at the right in Figure 3.20. These two mirrors were coupled to actuators that are mainly composed of stepper motors with accurately calipered moving steps. Each of four actuators could rotate one dimension of a mirror, which permitted the adjustment of location direction of the pump laser beam. The stepper motors were controlled by TRINAMIC TMCM-

6110 stepper motor control modules programmed with LabVIEW. The assembled periscope box is shown in Figure 3.21 and a screenshots of the LabVIEW user interface is shown in Figure 3.22.

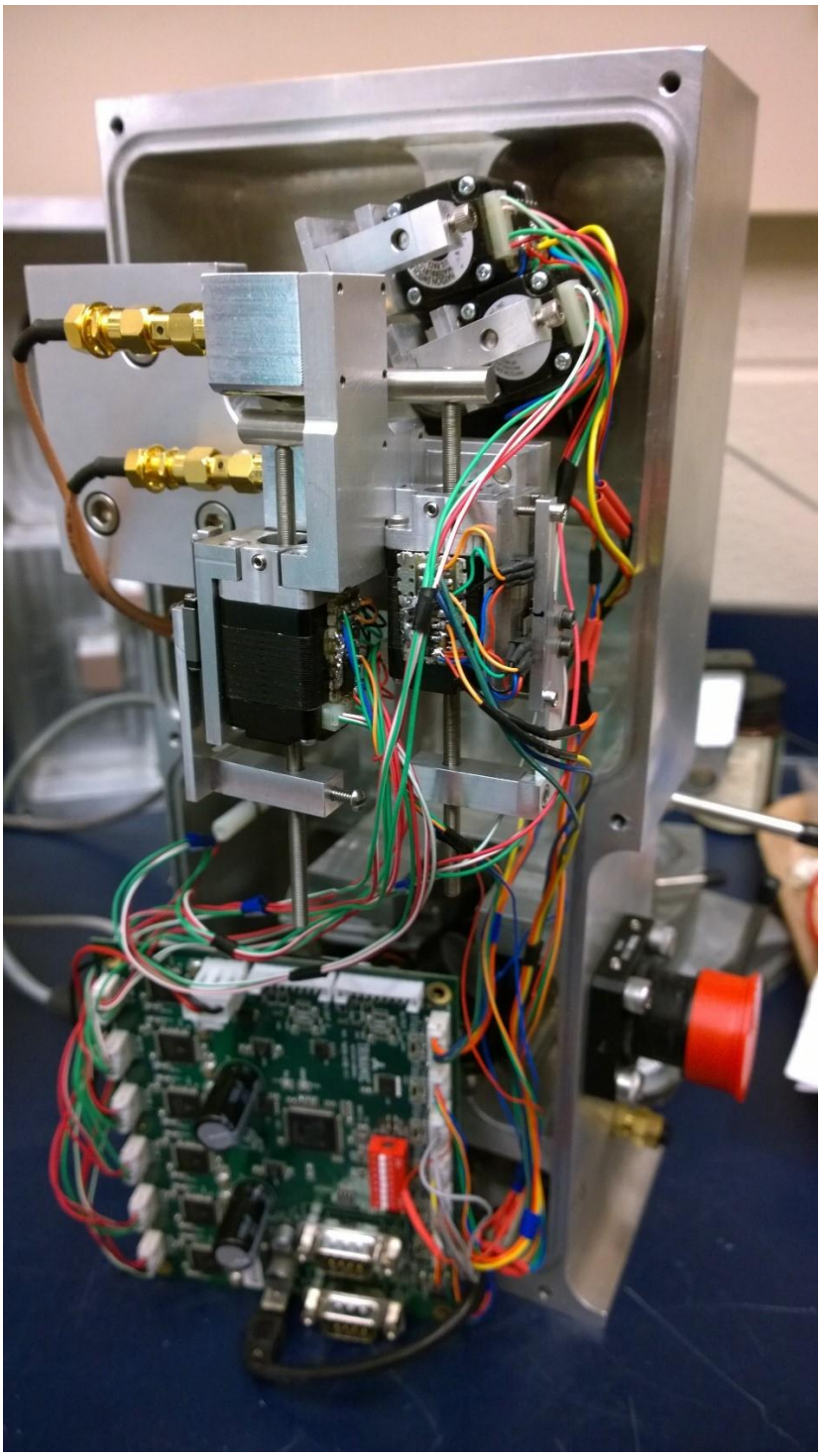

Figure 3.21 Photo of the assembled periscope box.

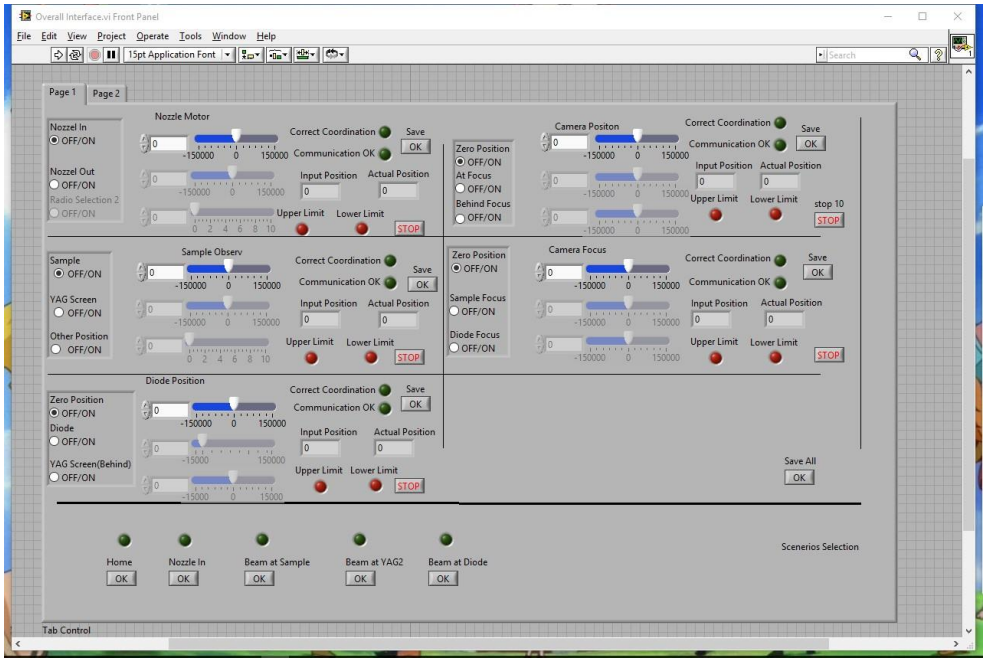

Figure 3.22 Screenshot of LabVIEW programming user interface.

Fig. 3.23 shows the components inside of the sample chamber from an aerial view, where the

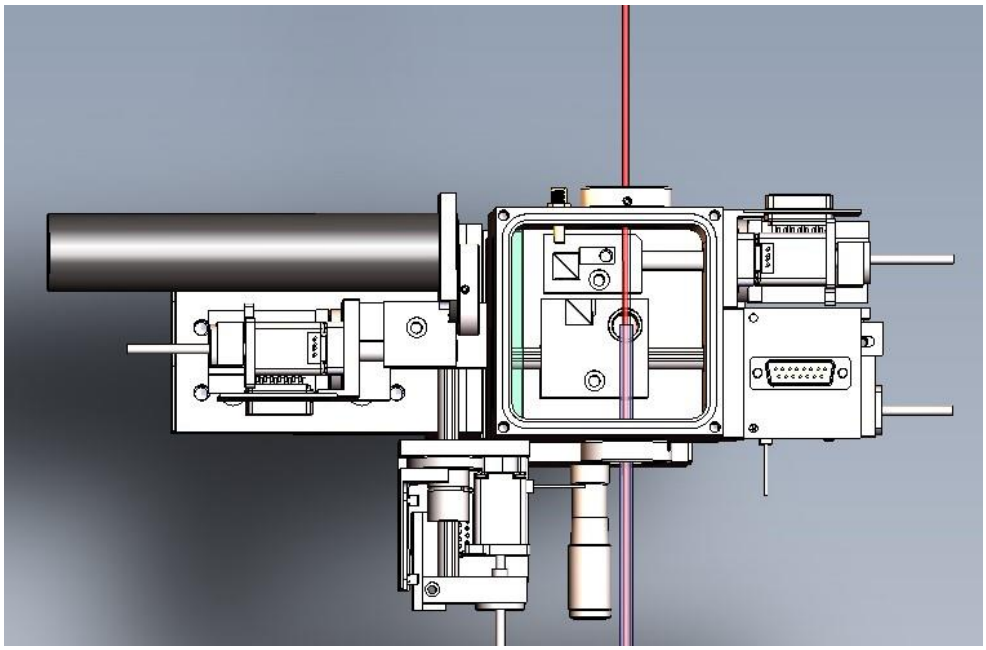

Figure 3.23 The sample chamber where the liquid sample is circulated inside. Inside of the chamber, laser and X-ray are crossed with each other on the liquid sample jet.

red line represents the X-ray and laser beam path. There are two actuators that are the same as the those used in the periscope box. The actuators in the sample chamber are coupled with stepper motors that can move the position of the components.

In the data acquisition process, the glass cylinder used to catch the liquid sample is moved to a position below the laser and X-ray beam path. For the laser-x-ray alignment process, two Cerium doped yttrium aluminum garnet (YAG:Ce) fluorescent screens were used to spectate the Laser and X-ray spot, one at the same location of the sample and one after. The X-ray and laser spot was imaged onto a camera sitting alongside of the chamber oriented vertically relative to the Laser and X-ray beam path. The two YAG screen spectators permitted quantitative movement of the turning mirror in the Laser-steering periscope box that could be accurately recorded and changed. This enabled precise control of laser beam path. Figure 3.24 shows an enlarged view of an actual recorded image. The larger spot is due to the laser and has a spot size of ~70 μm. The

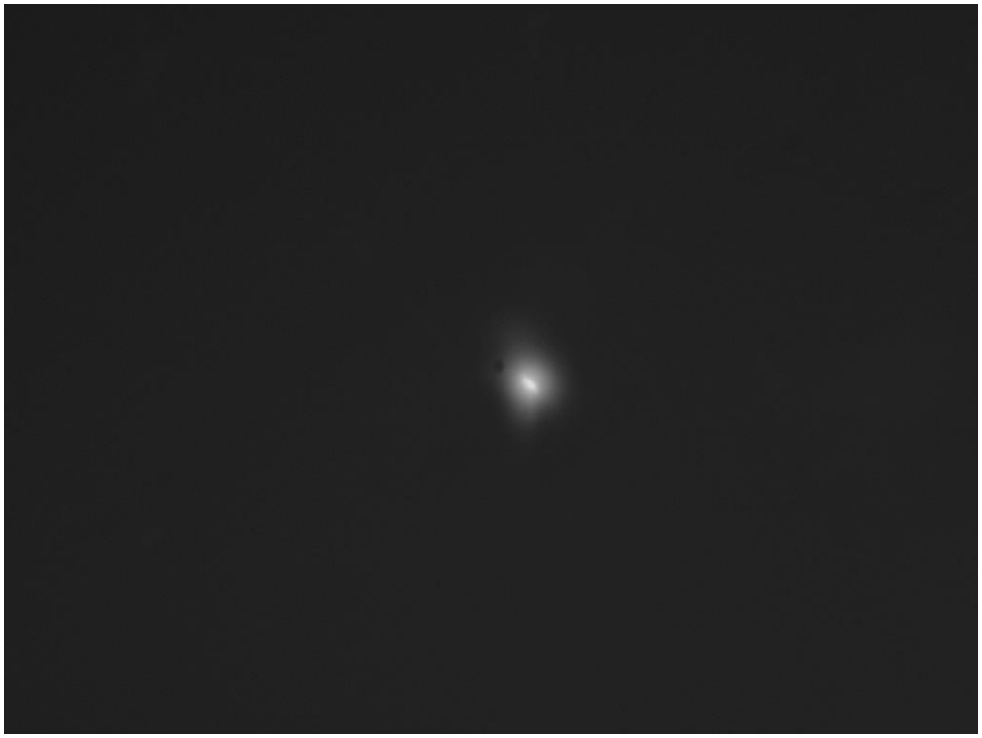

Figure 3.24 The X-ray laser overlapping imaged by YAG Screen fluorescence. The larger spot is laser and the smaller, brighter spot in the center is the X-ray spot.

X-ray spot size is ~30 μm.

3.5 Data Acquisition

The samples used in the experiments were a 50-mM potassium permanganate aqueous solution and a 50-mM potassium ferrohexacyanide solution. Potassium permanganate (ACS reagent, ⩾99.0%) and potassium hexacyanoferrate(II) trihydrate (ACS reagent, 98.5-102.0%) purchased from Sigma-Aldrich and distilled water provided by Argonne National Laboratory were used for preparing the aqueous solutions. A liquid pumping system was used to circulate the sample during the data acquisition process. Inside of the sample chamber where the laser and X-ray beams co-propagated, the liquid sample jet was produced by a stainless steel tube squished to an approximately rectangular shape. The liquid jet was measured to be 450 μm thick at the position where is intersected the laser and X-ray beams. During the data acquisition process, the periscope box and liquid chamber were flushed with nitrogen gas.

The laser light used for pumping the sample had a wavelength of 266 nm and a pulse length of 50 fs. The peak intensity on the sample was calculated to be $1.1*10^{13}$ W/cm^2. Some of the data presented in Chapter 6 were collected with a laser peak intensity of $4.3*10^{14}$ W/cm^2. The X-ray pulse was 150 ps long and monochromatic. The X-ray photon energy was selected with an X-ray monochromator with 1-eV bandwidth. The $KMnO_4$ data were collected at the pre-edge peak of Mn which has an energy of 6542.8 eV. The $K_4Fe(CN)_6$ data was collected at the Fe K edge, with energy centered at 7130 eV. Using the experimental setup discussed above, a 20-s exposure time was used. Each exposure captured 12k counts.

CHAPTER 4. THEORETICAL CALCULATION

4.1 Computation Methods

Single molecular geometries of MnO_4^- and $Fe(CN)_6^{4-}$ were calculated using Density Functional Theory (DFT) with the Gaussian software package.[93] All the calculations employed B3LYP functional exchange and correlation potential.[94] For the MnO_4^- molecule, the def2-TZVP basis sets were used for all atoms, and for $Fe(CN)_6^{4-}$ the TZVP basis sets were used.[95-96]

In addition to single molecule calculations, QM/MM Molecular Dynamics simulations were executed by our collaborator, Dr. Asmus O. Dohn. The DFT simulation started with ions initially structurally relaxed with using Grid-based Projector Augmented Wave code (GPAW).[97-98] The real grid spacing was set to 0.18 Å, and a complementary dzp-size basis of linear combinations of atomic orbitals was used to represent the pseudo wave functions. The PBE was used as functional.[99] The relaxed ion structure was then placed in 10 cubic simulation boxes. The boxes had 25-Å sides and were pre-equilibrated to 300 K in the NVT ensemble with a Langevin type thermostat and TIP3P force field.[100] The pre-equilibration was implemented in the Atomic Simulation Environment (ASE).[101] These simulation boxes were then re-equilibrated with electrostatically embedded QM/MM MD.[102-104] The parameters used in the structural relaxation process were also used to model the ion, except for an additional non-bonded force-field parameter applied with an additive QM/MM MD scheme. The parameters were from the UFF force field, and water molecules were modelled with TIP3P force field.[100, 105] The simulation boxes were then re-equilibrated to 300 K within 2 ps, using Langevin dynamics and a timestep of

2 fs. The total sampling time was around 10 ps for the MnO_4^- aqueous solution, and over 200 ps for the $Fe(CN)_6^{4-}$ aqueous solution. Equally spaced snapshots were taken and used as input into the FEFF9.6 software package for the calculation of X-ray Absorption spectra. Absorption spectra were calculated for both single solute molecules and solute molecules surrounding water solvent molecules.

Calculation of the XAS were executed with the FEFF9.6 software package.[23, 27-28] Full multiple scattering was done with self-consistent field atomic potentials.[23, 106] For both the FMS and SCF calculations a sphere radius of 6.0 Å around the metal center was used. The Hedin-Lundqvist electron self-energy was used for the energy dependent exchange correlation potentials in the XANES calculation. The amplitude reduction factor (S_0^2) was set to 1 uniformly in all the calculations in order to account for many-body interaction effects.

4.2 XAS of $KMnO_4$

4.2.1 The Solvent Effects on The Spectra of $KMnO_4$

In order to check the solvent's effect on the XAS, the absorption spectra for single MnO_4^- and MnO_4^- solute with equilibrated water solvent molecules were calculated and are plotted in Figure 4.1.

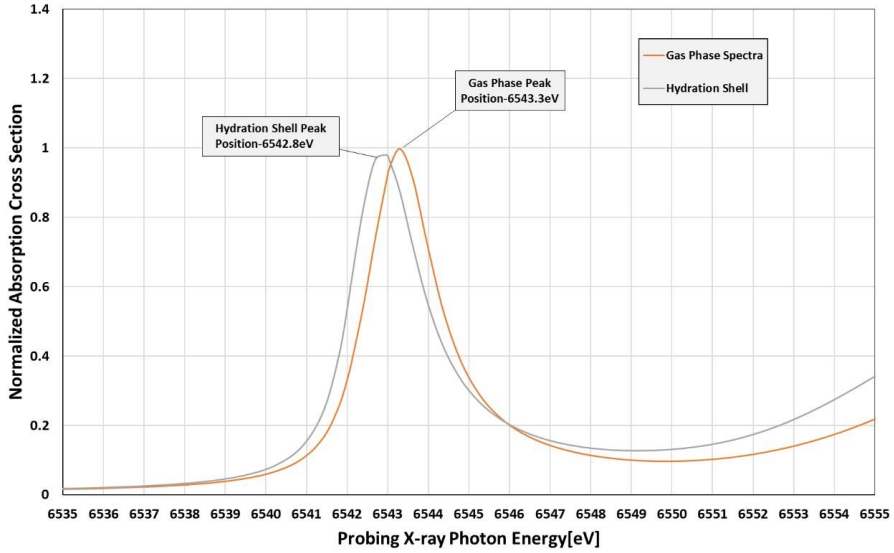

Figure 4.1 The theoretically calculated XAS of Permanganate molecule, with pre-edge region shown on the graph.

By adding water solvent molecules into the XAS FEFF calculation, there is a 0.5-eV blueshift in the XAS pre-edge peak position. This blueshift can be explained by analysis of the absorption mechanism. In the pre-edge absorption process, the Mn 1s core electron makes a transition to the 3d orbital in the MnO_4 molecule. The 1s→3d transition is symmetry-forbidden for the dipole operator, making the transition probability small. For MnO_4, and many other tetrahedral metal complexes, the Td molecular structure enables mixing of the 4p and 3d orbitals, increasing the dipole transition probability for the 1s→3d transition. The increased probability of transition due to orbital mixing is responsible for the pre-edge peak at 6542.8 eV shown in Figure 4.1. In the transition end state, the solvent water molecule orbitals overlap with the LUMO of the anion complex, and are involved in multiple scattering processes during X-ray absorption. Therefore, solvent molecules affect the solute absorption cross section. This effect was previously reported with aqueous nitrate and nitrite XAS. [107]

4.2.2 Geometry Changing Effect of Solute Molecule to The XAS

In order to investigate the geometry-induced effects on the XAS, the perfect Td molecular shape was changed systematically and then entered into FEFF to calculate the spectra. These spectra then were compared with the original spectra produced from the Gaussian optimized (unchanged) molecular structure. Comparison of the calculated spectra permitted the correlation of molecular geometry to changes in the XAS such as peak position and amplitude.

The O-Mn-O bond angle was changed from original 109.5°, and the XAS was calculated for each configuration. The range of bond angle changes was from -9.5 to +13.5 degrees. The calculated spectra are shown in Figure 4.2.

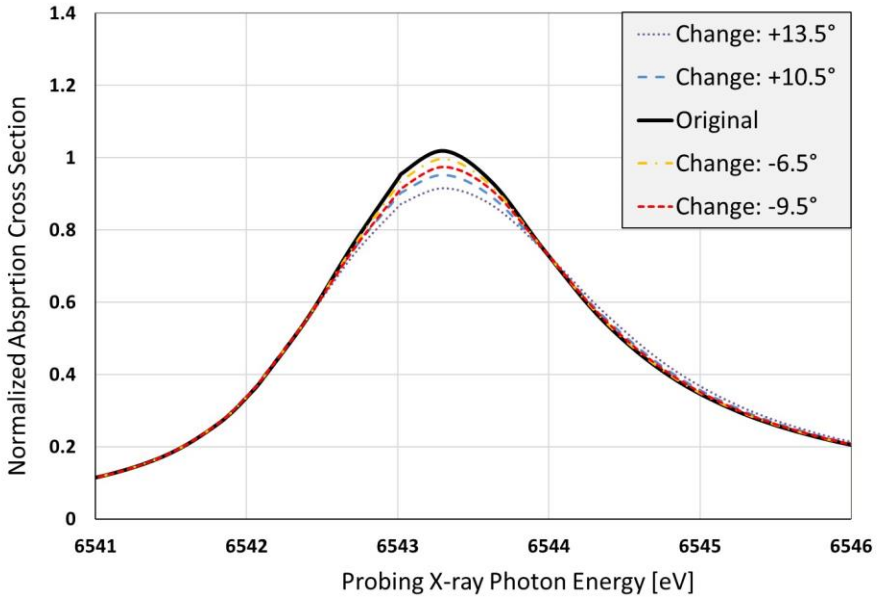

Figure 4.2 The XAS of MnO4- molecule with O-Mn-O bond angle changed with specific degrees.

The change of absorption peak position and amplitude relative to the tetrahedral structure are shown in Fig 4.3.

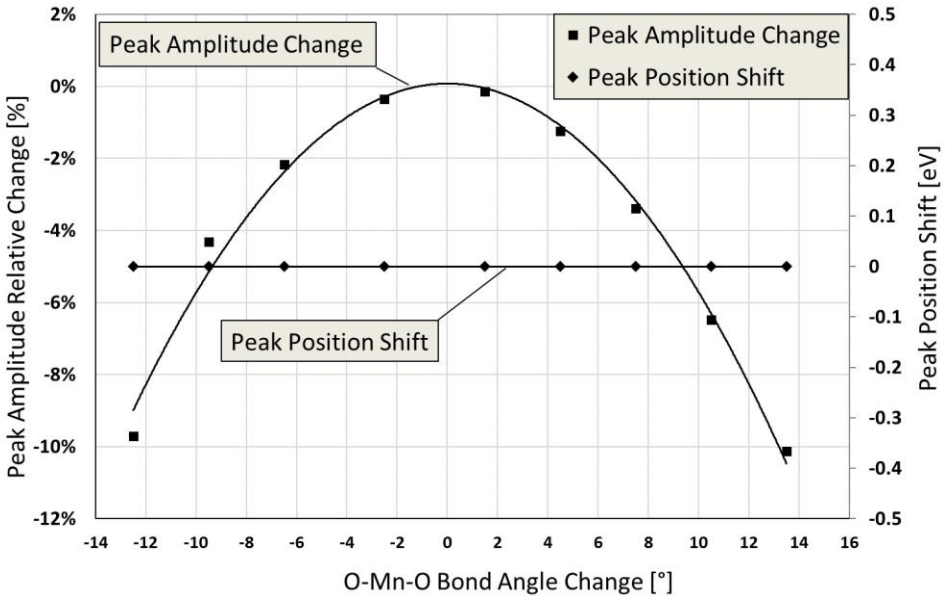

Figure 4.3 The absorption peak amplitude changes in percentage and peak position shift relative to the tetrahedral structure.

Changing the O-Mn-O bond angle does not shift the absorption peak position, but does change the absorption peak amplitude.

To investigate bond length induced effects on XAS, the Mn-O bond length was changed in increments of 5 to 7 picometers from the equilibrium value. The XAS are shown in Figure 4.4. Figure 4.5 shows that the change in Mn-O bond length shifts the absorption peak position as well as the peak amplitude.

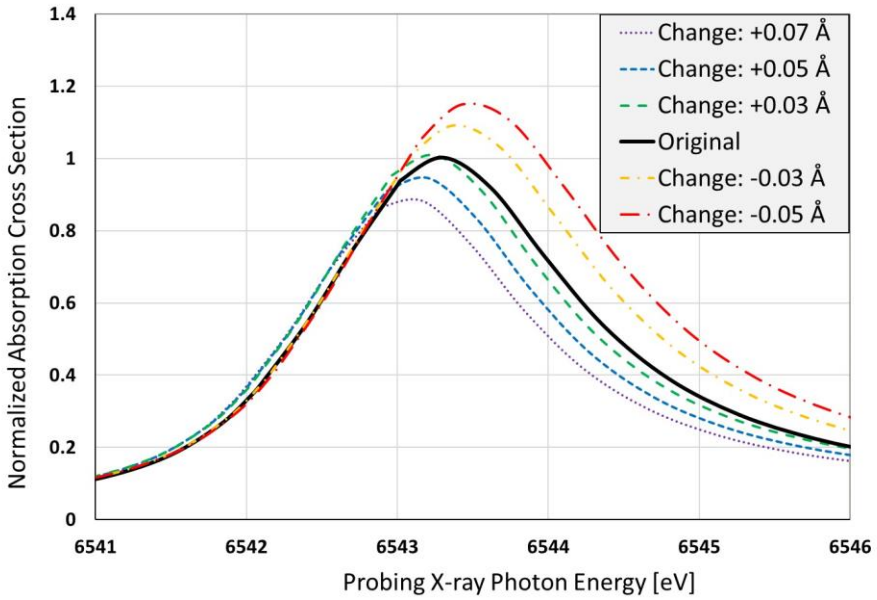

Figure 4.4 The XAS of different molecular structure from Mn-O bond length change.

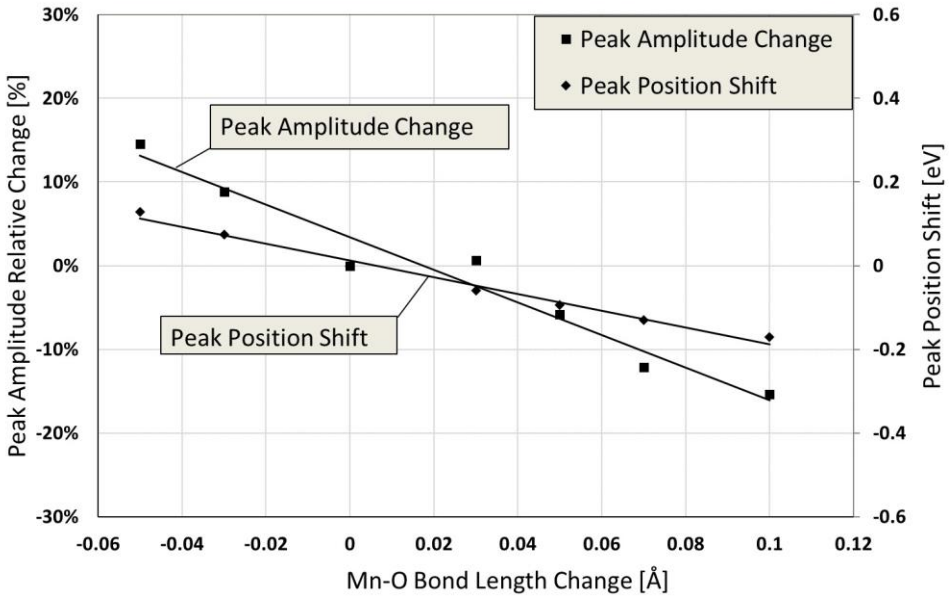

Figure 4.5 The Mn-O bond length change induced absorption peak amplitude change and peak position shift.

Finally, an average was taken from equally spaced snapshots of the MD simulation results in order to get the equilibrated solvated molecular structure. This average solvated solute structure deviates from the perfect tetrahedral shape in the O-Mn-O angle by ~2°. Also, one Mn-O bond length is altered by 1 pm. This solute structure was entered into FEFF in order to calculate the XAS and determine how the solvation-induced molecular deviations from perfect Td structure influence the absorption spectra. In order to better illustrate this effect, some intermediate structures between the gas phase and solvated structures were generated and the absorption spectra calculated. The gas phase, solvated and intermediate calculated spectra are shown in Figure 4.6 and Figure 4.7.

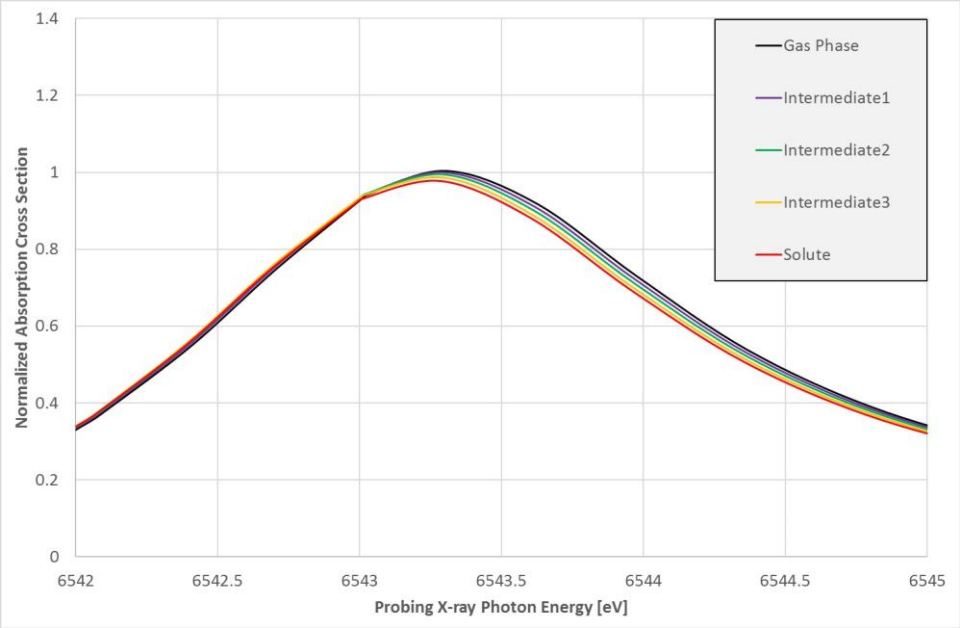

Figure 4.6 The spectra of molecules changing from tetrahedral (gas-phase optimized structure) to solvated molecular structure.

The solvation process causes almost no peak position shift, yet the peak amplitude is reduced by 2.5%.

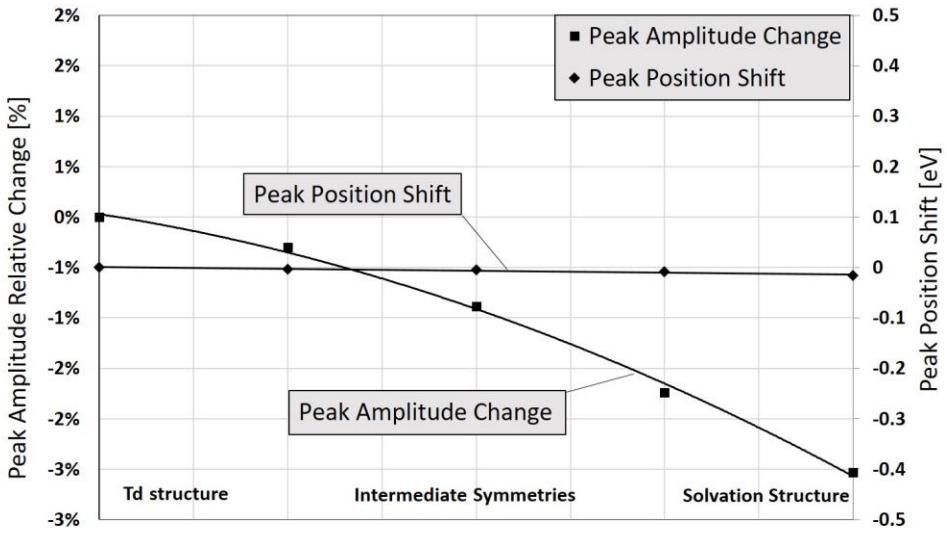

Figure 4.7 The absorption peak amplitude change and peak position shift with molecular structure changing from perfect tetrahedral to solvated molecular structure.

4.2.3 Solvent Shell Radius Change Effect

To determine the effects that solvent shell changes may induce in the XAS water molecules around the solute were moved uniformly by changing the distance between the solute and solvent molecules. XAS were then calculated and plotted in Figure 4.8.

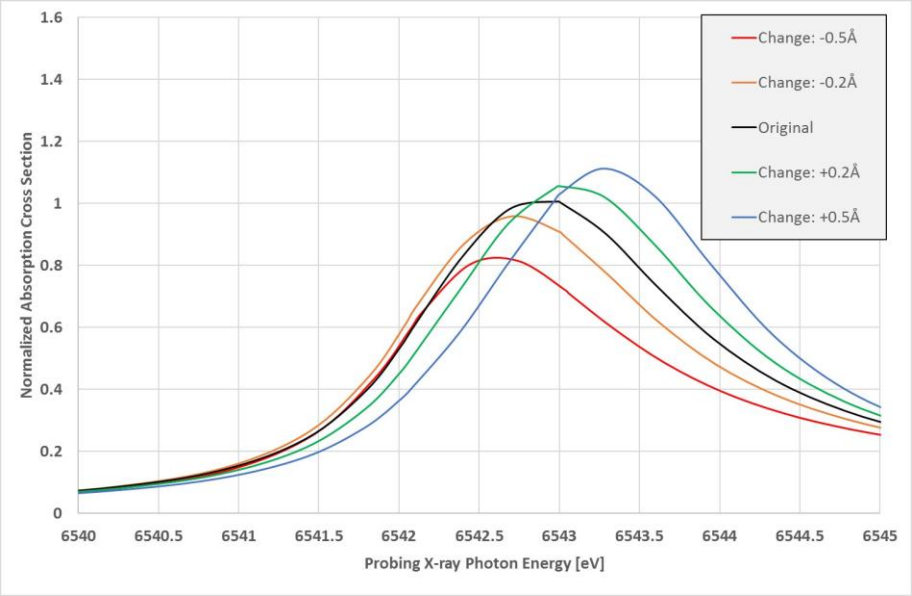

Figure 4.8 XAS of different configurations with solvent shell radius change from the equilibrated solvation structure.

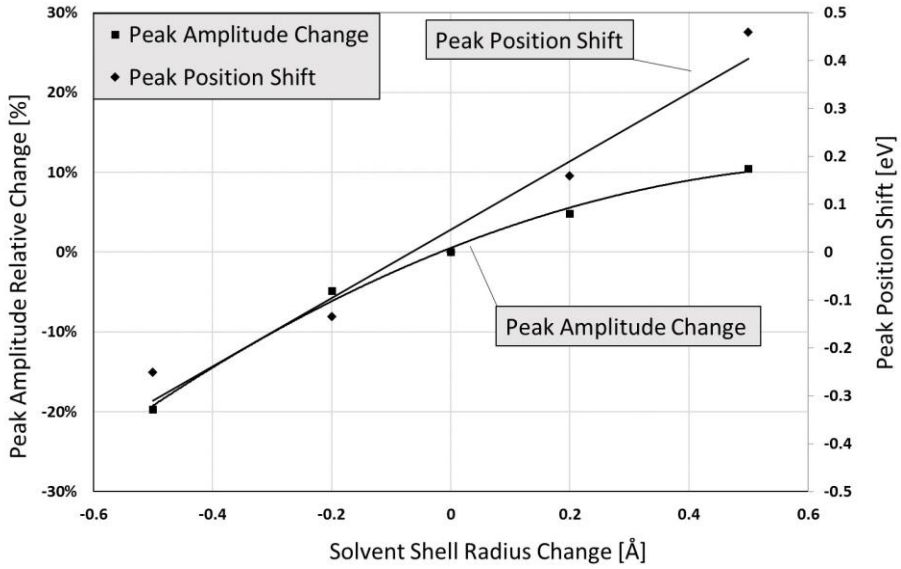

Figure 4.9 The absorption peak position relative shift and the peak amplitude relative change due to solvent shell shrinking and expansion.

The relative shift of absorption peak position and change of peak amplitude due to solvent shell radius change is shown in Figure 4.9. It is seen that upon solvation shell expansion the peak's amplitude change levels off, while its position still varies proportionally to the solvation shell radius.

4.3 XAS of $K_4Fe(CN)_6$

Similarly to what was done for the permanganate data, the XAS of $Fe(CN)_6^{4-}$ were also calculated with FEFF.

4.3.1 The Solvent Effect to XAS

The XAS of a single solute molecule optimized with the Gaussian software package and the XAS of a solute molecule with water solvent molecules around it are shown in Figure 4.10.

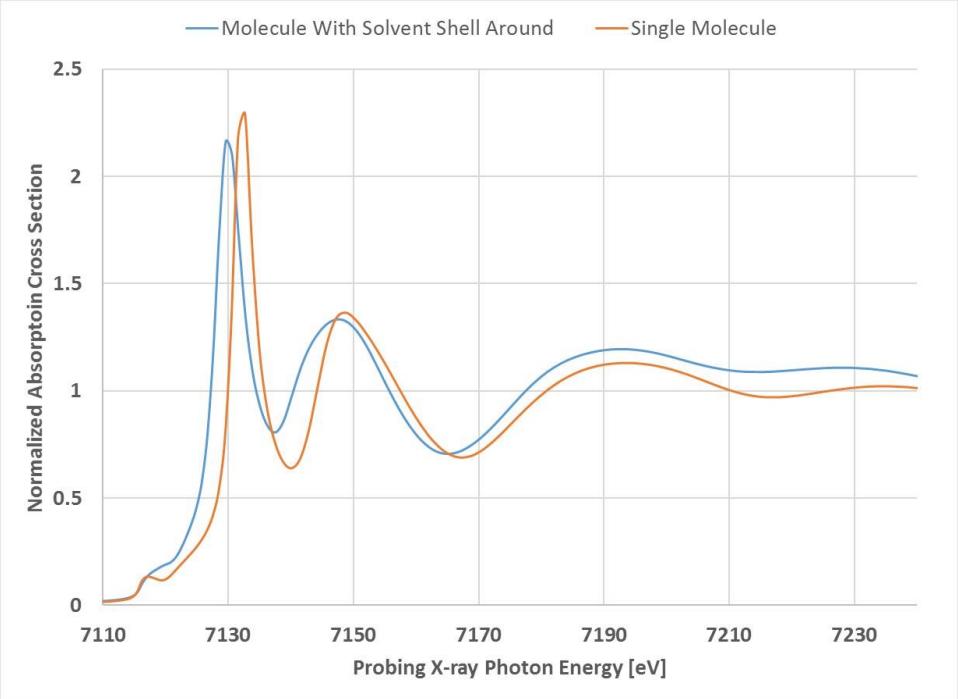

Figure 4.10 The XAS of single molecule and XAS with water solvent molecules around of ferrohexacyanide.

The solvent not only affects the absorption peak amplitude but also induces a ~1.5-eV redshift in peak position.

4.3.2 Geometric Changing Effect of Solute Molecule to XAS

The Fe-C bond length was changed systematically and XAS calculated with these configurations. The XAS are shown in Figure 4.11.

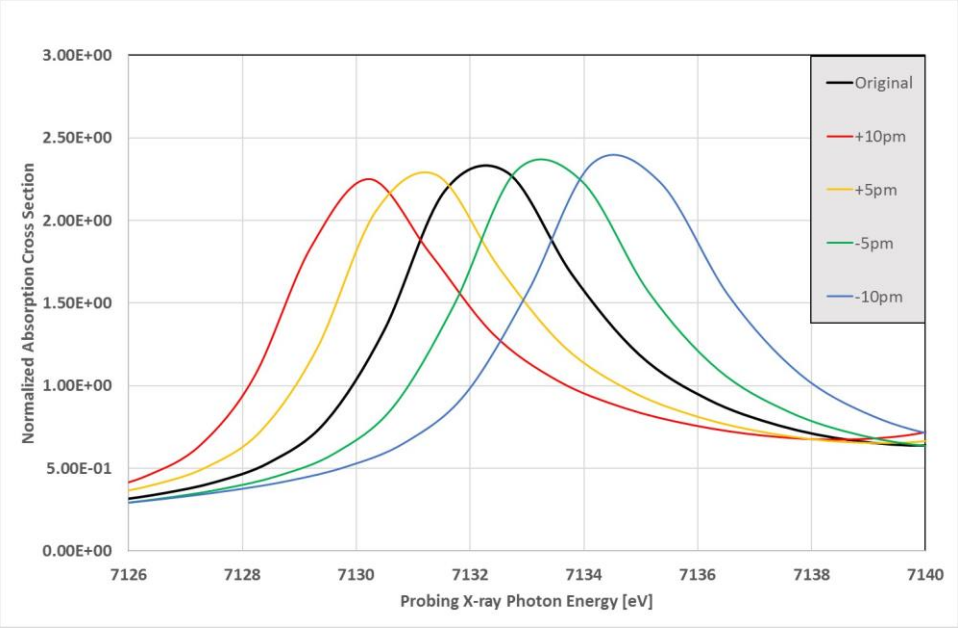

Figure 4.11 The XAS of ferrohexacyanide with Fe-C distance changing for 5 and 10 picometers.

The absorption peak relative amplitude change and position shift due to changes in Fe-C distance change are shown in Figure 4.12.

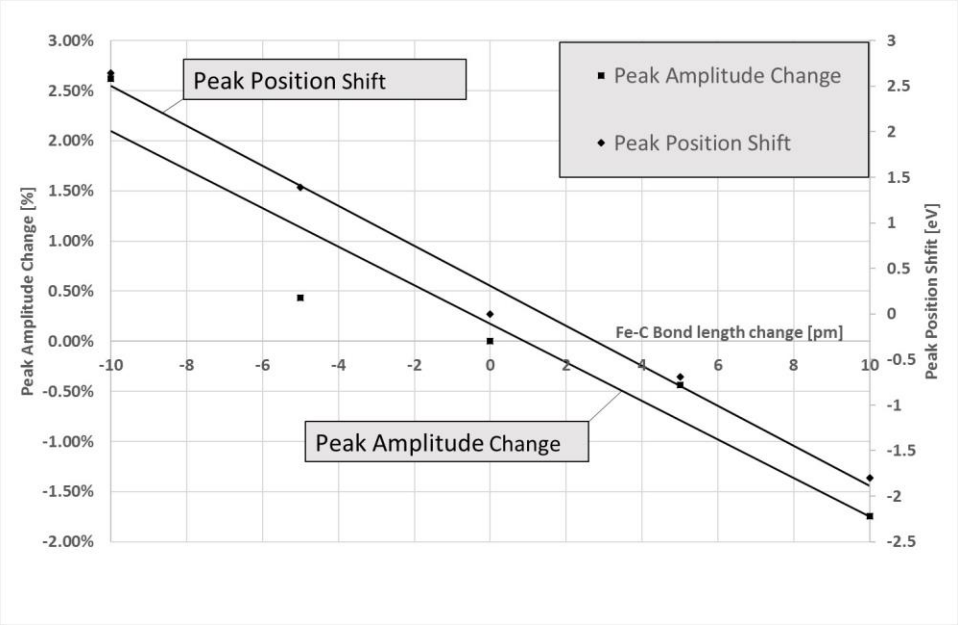

Figure 4.12 The absorption peak position shifts and peak amplitude relative change due to the change of Fe-C distances.

The bond angle was also changed from the octahedral structure. Changes in bond angle were executed by changing the C-Fe-C angle and Fe-C-N angle. XAS for each configuration was calculated, and the relative shift of absorption peak position and relative change of peak amplitude are shown in Figures 4.13 to 4.16. The C-Fe-C and Fe-C-N angles were also changed simultaneously, and the resultant spectra and relative changes are shown in Figure 4.17 and Figure 4.18.

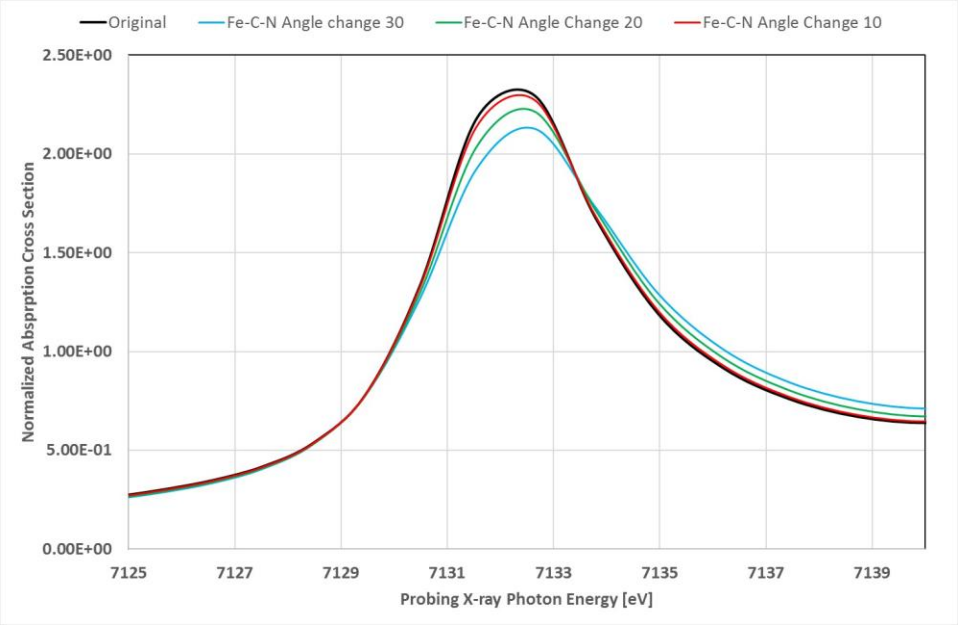

Figure 4.13 The XAS of molecular structures with Fe-C-N changing to some specific degrees.

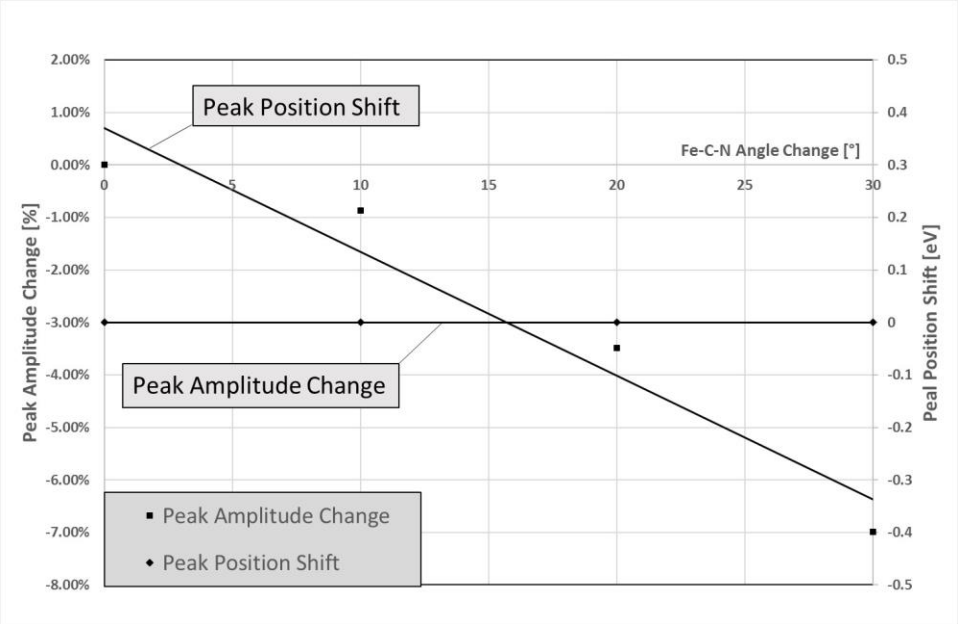

Figure 4.14 The absorption peak position shifts and peak amplitude relative change due to Fe-C-N bond angle change.

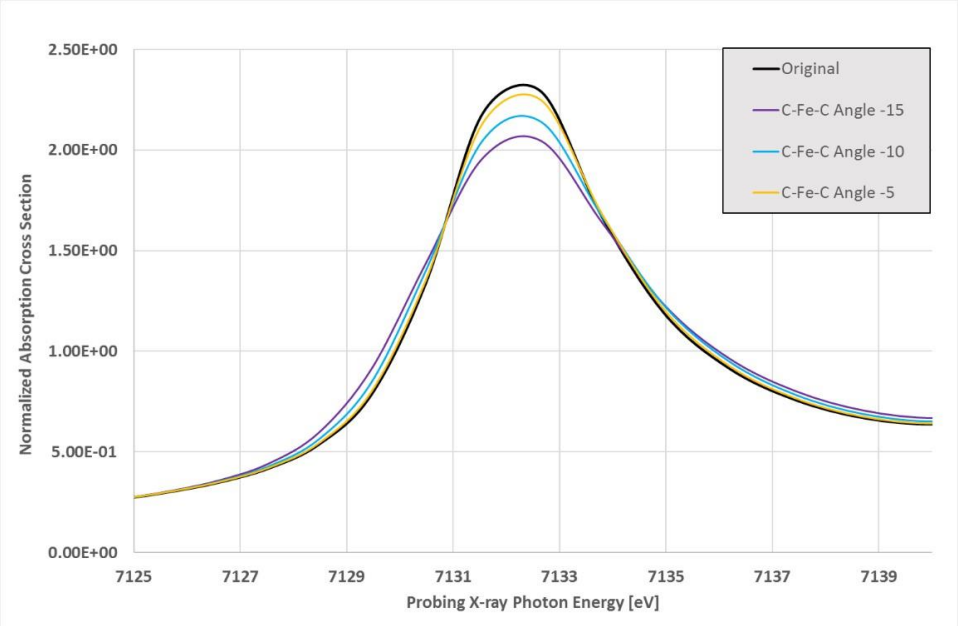

Figure 4.15 The XAS of molecular structure with C-Fe-C bond angle changed to some specific degrees.

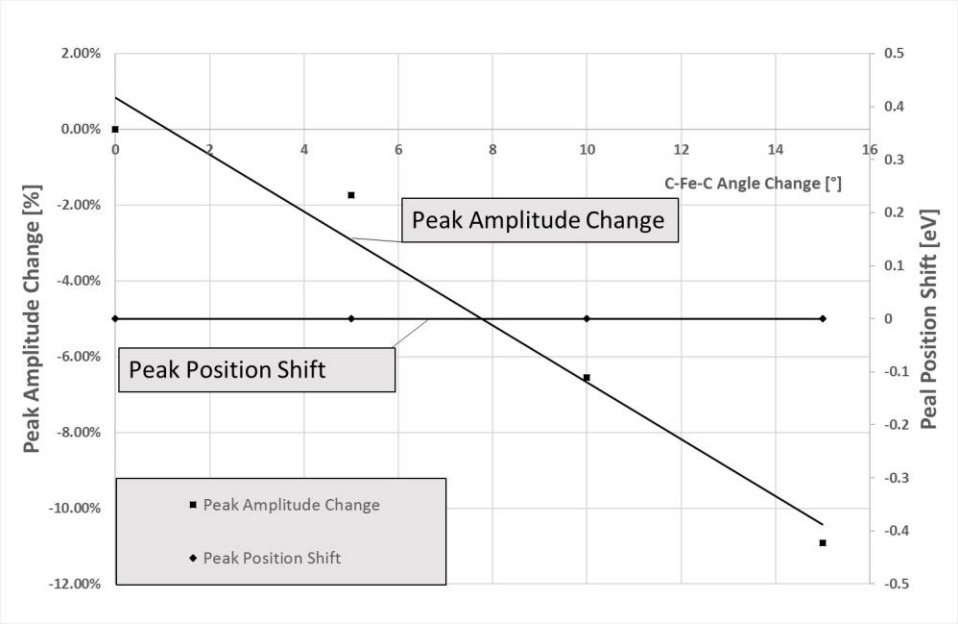

Figure 4.16 The absorption peak position shift and peak amplitude change due to C-Fe-C bond angle change.

The Fe-C-N angle was changed by 10 and 20° while C-Fe-C angle was kept at 80° (10° deviation from octahedral structure). The XAS and changes in peak position and amplitude are shown in Fig. 4.17 and Fig. 4.18.

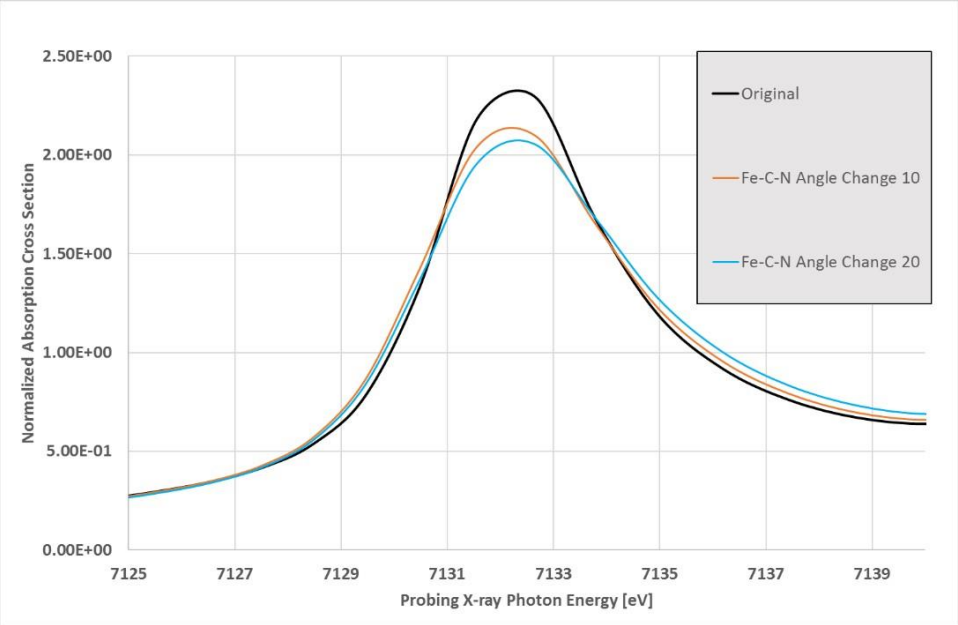

Figure 4.17 XAS of molecular structures with Fe-C-N and C-Fe-C bond angle change.

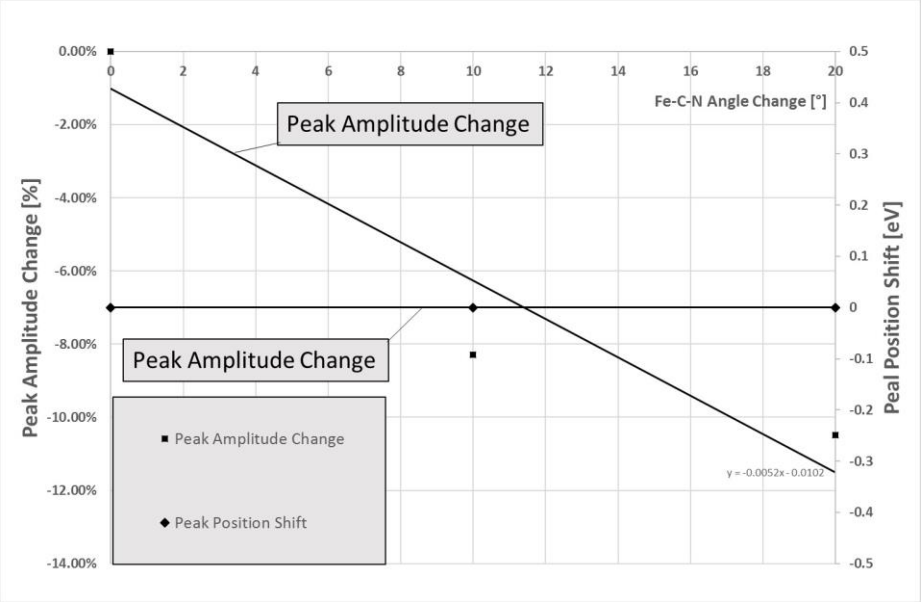

Figure 4.18 Absorption peak position shift and peak amplitude change due to both C-Fe-C and Fe-C-N angle changing from perfect Td Structure. Here, the C-Fe-C angle was kept constant at 80° and Fe-C-N was varied for specific degrees as shown.

4.3.3 Solvent Shell Changing Effects

The solvent shell about ferrohexacyanide was modified by uniformly varying the distance between the solvent water molecules and the solute molecule center. XAS of these different

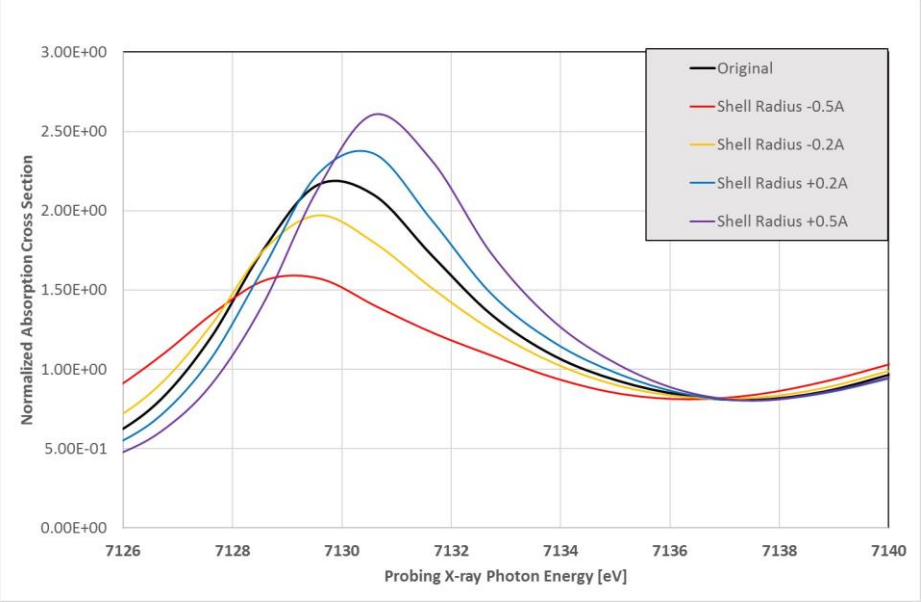

Figure 4.19 XAS of configurations with different solvent shell radius.

configurations were calculated and are shown in Fig. 4.19 and 4.20.

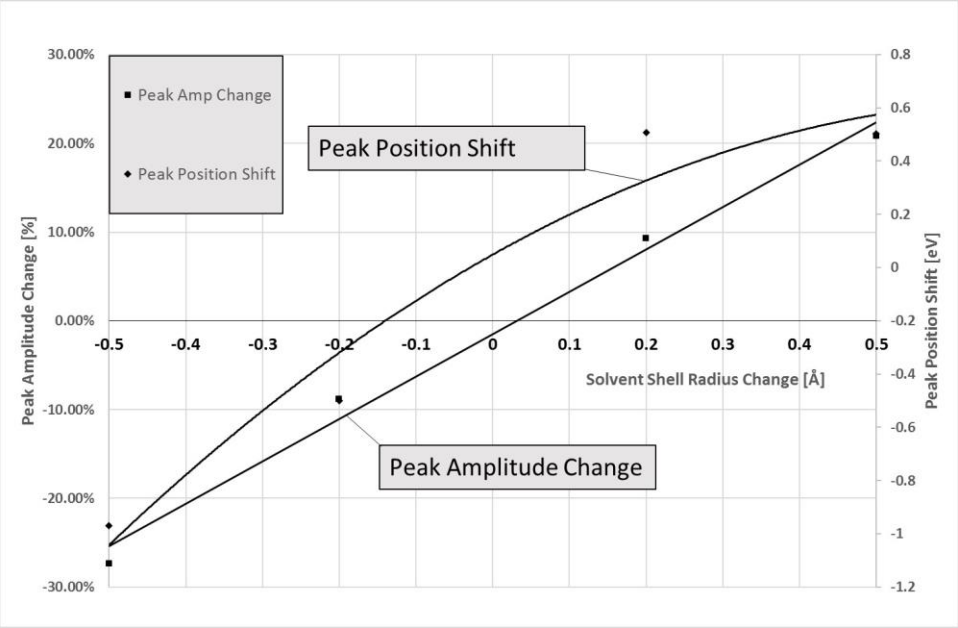

Figure 4.20 Absorption peak position shift and the peak amplitude relative change due to solvent shell radius change.

4.4 Summary of the Calculation Results

From the above graphs, some conclusions can be drawn. First, changes in the solvent shell radius modulate the absorption peak profile by shifting the peak position up to ~1.5 eV, and changing the peak's absorption cross section by as much as 20%. This strategy is presented in Chapter 5 and Chapter 6.

For both permanganate and ferrohexacyanide, the change of metal-ligand bond lengths shifts the peak position and changes the peak height The only molecular geometric change that does not shift the absorption peak position is the change of bond angles. This feature is of special importance because it can be used for the identification of structural dynamics, as will be discussed in Chapter 5.

CHAPTER 5. SECOND HARMONIC GENERATION OF ACOUSTIC PHONONS

5.1 Physical and Photochemical Dynamics of Aqueous Permanganate Solution

The solvation shell dynamics of potassium permanganate in water were measured at 30°C. The MnO_4^- anions served as probes for measuring the response of the sample to impulsive photo excitation of the 50-mM solution with 266-nm, 50-fs laser pulses. The pre-edge absorption line of water solvated permanganate anion is at 6542.8 eV. In order to collect as much information as possible about the absorption profile, three probing X-ray photon energies were selected around the absorption peak maximum at 6542.0 eV, namely 6542.8 and 6543.5 eV.

Of all the dynamics that was going to be initiated upon laser excitation, the photoexcitation of MnO_4^- is the most straightforward and obvious process to consider. Based on literature data, MnO_4^- excited by 266-nm UV-light is promoted to the 3^1T_2 excited state.[108-110] The photo-excited state is either going to relax to the ground state or forms a Mn(V) peroxo complex intermediate with C_{2v} geometry. Figures 5.1 and 5.2 depict the relevant chemistry and geometries. The intermediate was characterized by a kinetic study to have a relatively long life due to a symmetry barrier, and will either transform back to the permanganate ground state ion or form MnO_2^- with the release of an oxygen molecule.

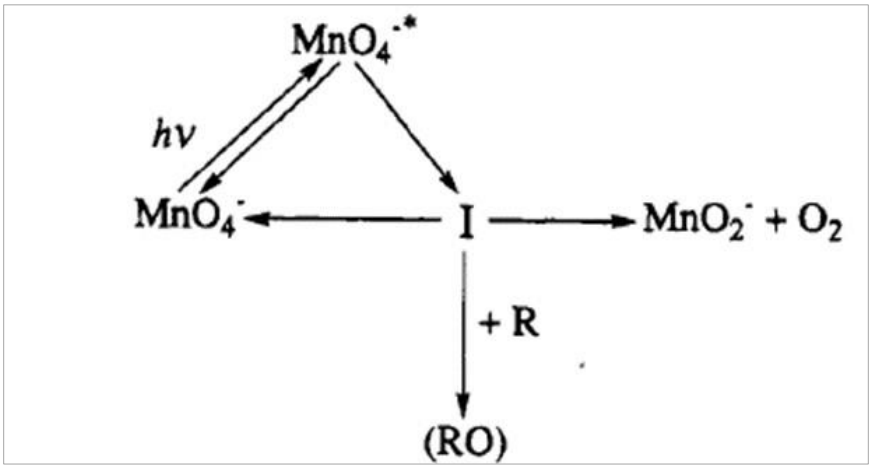

Figure 5.1 Chemical scheme of photoexcited permanganate anion. Picture taken from Ref [109].

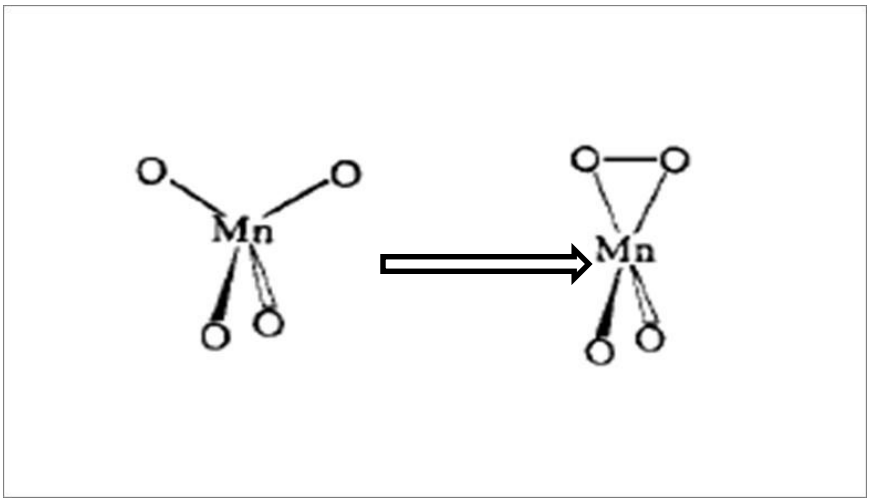

Figure 5.2 Transformation from tetrahedral structure to C_{2v} Mn peroxo complex, molecular structure taken from Ref [109].

The photochemical process is not the focus of this study. No matter whether the ion is in the peroxo form or the photochemical MnO_2 product, when the tetrahedral structure is broken, the pre-edge absorption peak vanishes. Thus, any photochemical products in the solution do not contribute to the recorded absorption signal except for a minor baseline shift that can be subtracted in the data fitting process.

Instead of photochemical processes, the photophysical processes induced by the strong electric field of the pump laser are emphasized in this work. Based on our laser conditions discussed in Chapter 3 the peak intensity can be calculated to be about 10^{13} W/cm^2. The electric field produced by such a high intensity laser intensity is going to induce substantial nonlinear effects, like electrostriction.[111-112] These nonlinear effects induced scattering, which is most intense in the backward direction. This is called Stimulated Brillouin Backscattering.[113-114] The backscattered light is going to interfere with the incoming light, creating an interference transient grating with wavelength:

$$\lambda_{grating} = \frac{\lambda_{laser}}{2n} \tag{5.1}$$

with n as the refractive index of the sample. The transient grating produced by the strong electric field accelerates the polarized molecules and transfers momentum to the sample. The resulting Stokes phonons have the same wavelength as the transient grating period. The phonons are not spatially coherent because they are generated at random positions in the sample. Importantly, the phonons are coherent in time because they are produced with a femtosecond pulse. The advantage of using solute molecules as local probes to detect phonons is that local probes do not require spatial coherence of the phonons for detection.

To summarize Chapter 4 and the current section of Chapter 5, theoretical calculations indicate that solvent shell movement is reflected in the solute XAS. The sensitivity of XAS to solvent effects is due to hydrogen bonding of the solute complex to the surrounding water molecules. The use of solute molecules to probe phonons in the surrounding solvent is advantageous in that the local environment of the solute is probed and does not require spatial coherence of the phonons.

5.2 Experimental Data and Analysis

The transmittance changes $\Delta T(t)$ with respect to time measured at the energy points at 6542.0, 6542.8 and 6543.5 eV are shown in Figure 5.3. Time zero is defined as the time when the laser pulse hit the sample.

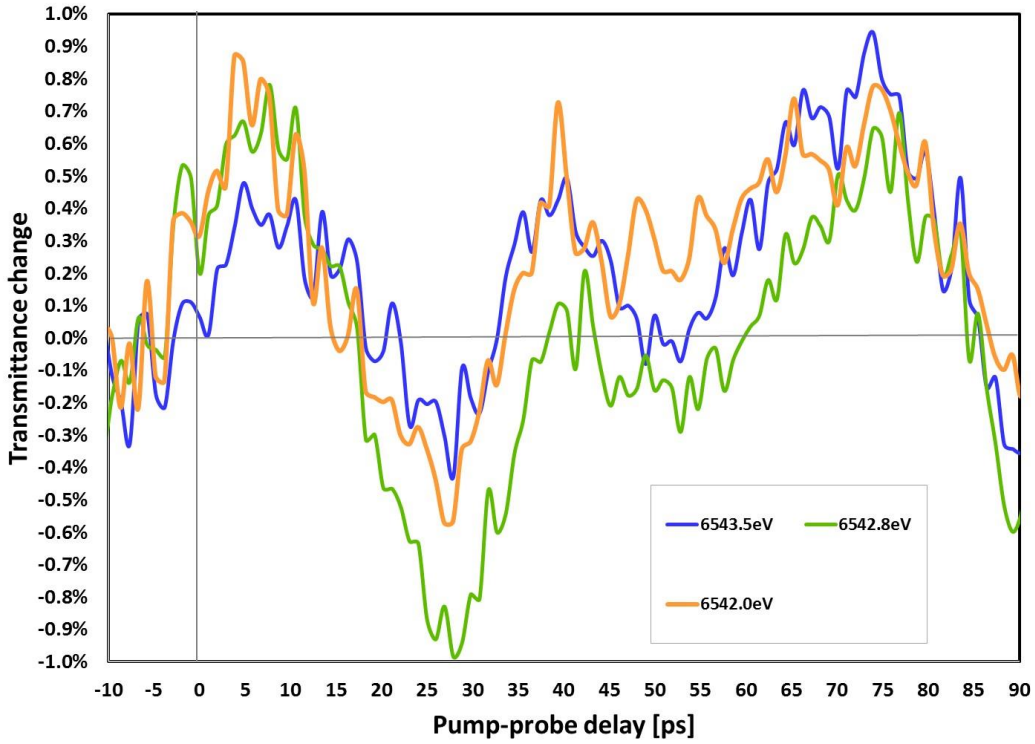

Figure 5.3 The Transmittance change with respect to time measured at three energy points around the pre-edge peak.

The three kinetic traces shown in Figure 5.3 have similar features. An average was taken for these three traces in order to achieve better statistics. The averaged kinetic trace is shown in Figure 5.4. In this figure, the transmittance change every 1.3ps is shown, along with a fit of the data points.

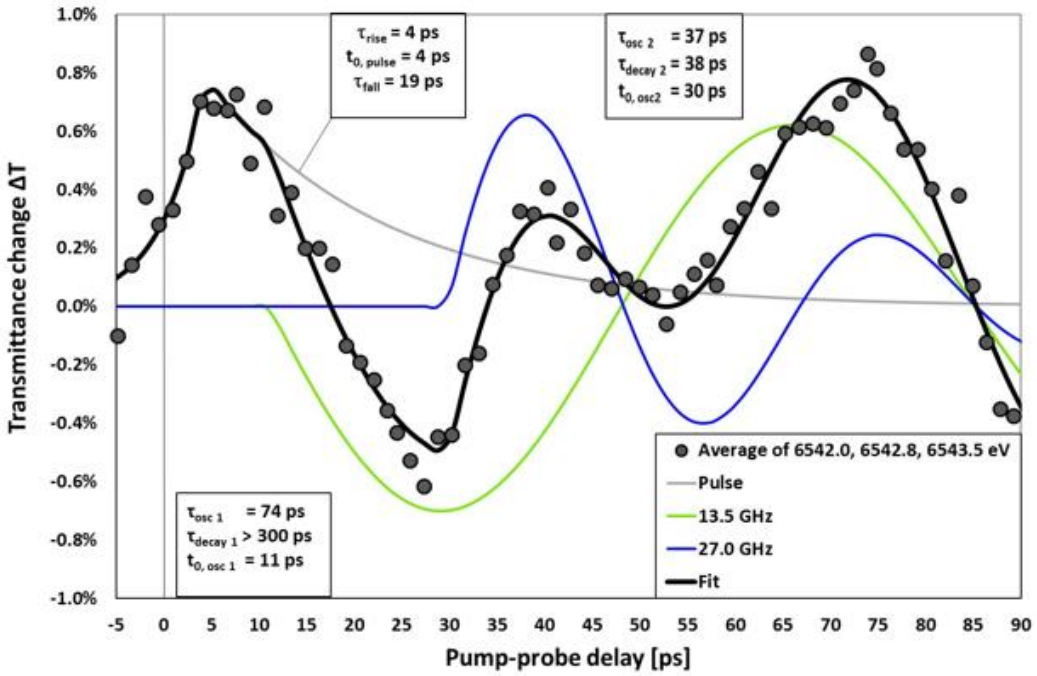

Figure 5.4 Changes of the X-ray transmittance at the manganese pre-edge absorption line vs. time after laser excitation. A fit to the data points is shown in black.

The fit is the summation of three functions., one double-exponential rise and decay and two damped oscillatory functions.

$$\Delta T(t) = T_{pulse} \cdot Pulse(t) + T_{osc1} \cdot Oscillation_1(t) + T_{osc2} \cdot Oscillation_2(t)$$

$$with \quad Pulse(t) = \begin{cases} e^{\left(\frac{t - t_{0,\,pulse}}{\tau_{rise}}\right)} & for\ t \le t_{0,\,pulse} \\ e^{-\left(\frac{t - t_{0,\,pulse}}{\tau_{fall}}\right)} & for\ t > t_{0,\,pulse} \end{cases} \tag{5.2}$$

$$and\ for\ i = 1,2 \quad Oscillation_i(t) = \begin{cases} 0 & for\ t \le t_{0,\,osc\ i} \\ e^{-\left(\frac{t - t_{0,osc\ i}}{\tau_{decay\ i}}\right)} \cdot \sin\left(2\pi \frac{t - t_{0,\,osc\ i}}{\tau_{period\ i}}\right) & for\ t > t_{0,\,osc\ i} \end{cases}$$

There is a nearly instrument-limited rise at time zero with rise time constant of 4 ps followed by an exponential decay with a time constant of 19 ps. At 11 ps after excitation, a 13.5-GHz wave is produced. 20 ps after this wave is launched, a quarter period later, a wave with twice the frequency is produced. These waves both have decay time scales of at least tens of picosecond, indicating a long coherent time of these oscillatory features. The long coherence time is an indication of the existence of acoustic phonons. Specifically, these oscillations are identified as fundamental and second harmonic (SH) phonons. A full list of the fitting parameters is in Table 5.1.

5.3 Interpretation and Discussion

The phonons are produced by the intense pump laser pulse which may induce strong

Pulse Peak Amplitude [%]	0.78
Pulse Peak Rise Time [ps]	4.45
Pulse Decay Time [ps]	18.52
Oscillation 1 Amplitude [%]	-0.74
Oscillation 1 Frequency [GHz]	13.5
Oscillation 1 Initiation Time [ps]	11.02
Oscillation 1 Decay Time [ps]	304.16
Oscillation 2 Amplitude [%]	0.83
Oscillation 2 Frequency [GHz]	27.0
Oscillation 2 Initiation Time [ps]	29.74
Oscillation 2 Decay Time [ps]	37.46

Table 5.1 A full list of parameters of the fitted functions of the averaged kinetic traces measured around 6542.8eV.

electrostriction, sample heating or photochemical processes as discussed in Section 5.1. The phonons generated after laser excitation are the focus of this thesis. Other excitation features cannot be resolved due to the temporal resolution of the experimental setup, and are therefore not discussed here.

The fundamental phonon frequency of 13.5 GHz corresponds to a wave-number of 0.062 nm^{-1} for a sound speed of 1360 m/s. In order to reproduce 13.5-GHz Brillouin backscattering according to the $\lambda_{grating} = \lambda_{laser} / 2n$ relationship, a refractive index of water n = 1.33 at 266 nm is used in this equation to create an interference period of 100 nm. The second harmonic oscillation with 27-GHz frequency decays with a time constant of 38 ps. This is much faster than the fundamental oscillation decay time of 300 ps. Thus, the coupling between these two oscillations decays with time. This effect is attributed to the structural dynamics of hydrogen bond network, as will be discussed in the following section.

In order to extract more information, the measured spectra at the three energy points were fitted simultaneously with a time and energy-dependent X-ray transmittance function. The results are shown in the Figures 5.5 to 5.7. The fitting equations are defined as:

$$\Delta T_{Emeasure}(t) = \underbrace{\frac{T_1}{\sqrt{2\pi}\sigma} e^{-\frac{1}{2}\left(\frac{E_{measure}-E_1}{\sigma}\right)^2}}_{\text{Pulse and fundamental oscillation}} + \underbrace{\frac{T_2}{\sqrt{2\pi}\sigma} e^{-\frac{1}{2}\left(\frac{E_{meausre}-E_2}{\sigma}\right)^2}}_{\text{Second Harmoinc Oscillation}} \quad with$$

Parameter equations	*Fit - parameters*
$T_1 = T_{pulse} Pulse(t) + T_{osc1} Oscillation_1(t)$	$T_{pulse},\ t_{0,\,pulse},\ \tau_{rise},\ \tau_{fall},\ T_{osc1},\ t_{0,\,osc1},\ \tau_{osc1},\ \tau_{decay1}$
$E_1 = E_0 + E_{osc1} Oscillation_1(t) + E_{\log} Logistic(t)$	$E_{osc1}, E_{\log},\ t_{0,\log}, \tau_{\log}$
$T_2 = T_{osc2} Oscillation_2(t)$	$T_{osc2}, \tau_{osc2}, \tau_{decay2}$
$E_2 = E_0 + E_{osc2} Oscillation_2(t) + E_{\log} Logistic(t)$	E_{osc2}
$\sigma = const$	σ
$E_0 = 6542.8eV$	
$Logistic(t) = \frac{1}{1+e^{-\frac{t-t0,\log}{\tau_{\log}}}}$	

(5.3)

The profile was written as the sum of two Gaussian curves with the first dependent on the time-zero pulse and the fundamental oscillation, and the second only dependent on the second harmonic oscillation. These dependence relationships are applied in order to allow the second harmonic waves to influence the X-ray absorption spectrum differently than the fundamental waves. The Gaussian peaks were defined by their common peak center energy E_0, their common peak width σ, separate amplitudes (T_1 and T_2), and energy positions (E_1 and E_2). In order to account for the time-dependent features of these Gaussian parameters amplitudes T_{pulse}, T_{osc1}, and T_{osc2}, describing the transmittance change the same way as in equation (5.2), peak energy position shifts E_{osc1} and E_{osc2}, and time-dependent fit functions Pulse(t) and Oscillation(t) were defined as shown in the equations. Finally, a function *Logistic(t)* was used to describe the spectral shifts that may result from possible solvent shell reorganization and expansion caused by solute molecule electronic excitation, vibrational relaxation and a sudden system temperature jump after laser excitation.[110]

The resulting fit for the measurements at the three X-ray energies are shown in Fig. 5.5, 5.6 and 5.7.

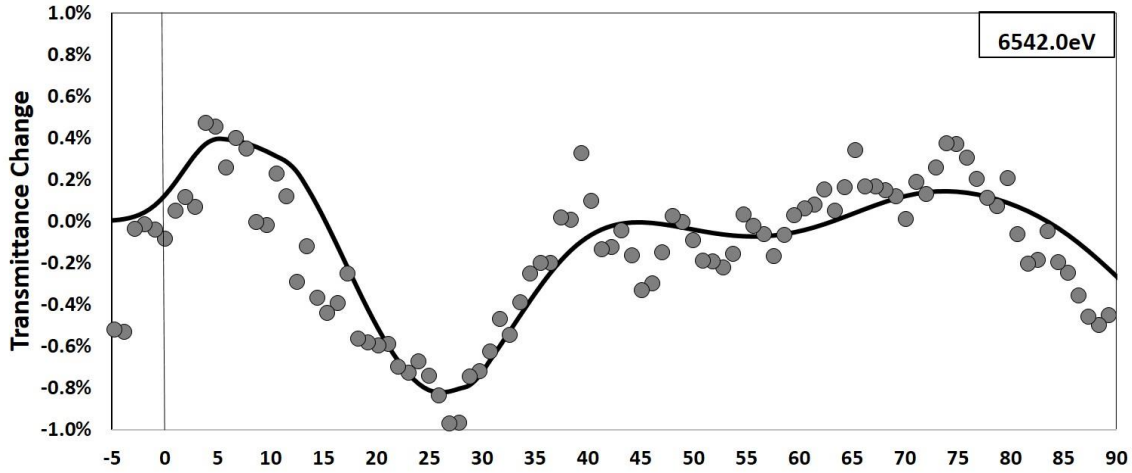

Figure 5.5 The fitting result of the spectra measured at 6542.0eV. The dots are the measured data and the black line is the fitting.

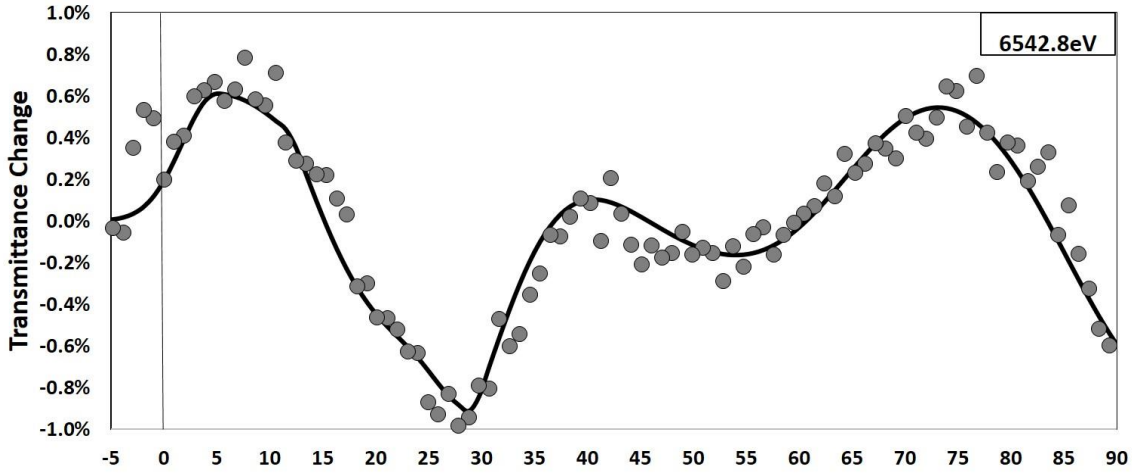

Figure 5.6 The fitting result of the spectra measured at 6542.8eV. The dots are the measured data and the black line is the fitting.

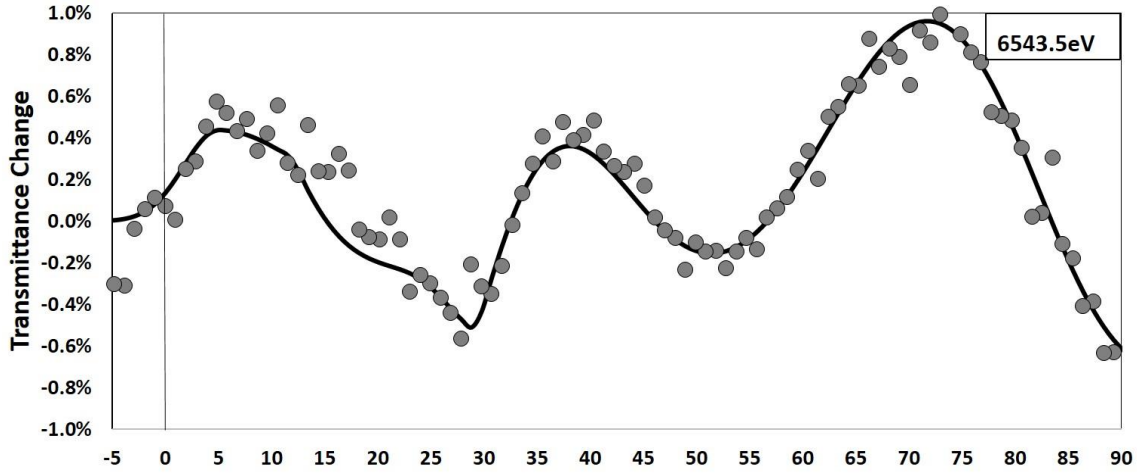

Figure 5.7 The fitting result of the spectra measured at 6543.5eV. The dots are the measured data and the black line is the fitting.

The time-dependent profiles of T_1, T_2, E_1, E_2, and E_{log} are shown in Figure 5.8 and a full list of fit-parameters is in the Table 5.2.

A_{pulse}	1.31%		
$t_{0,pulse}$	5.0 ps		
τ_{rise}	4.7 ps		
τ_{fall}	11.3 ps		
A_{osc1}	-2.15%	A_{osc2}	2.50%
τ_{osc1}	71.7 ps	τ_{osc2}	35.8 ps
$1 / t_{0,osc1}$	13.9 GHz	$1 / t_{0,osc2}$	27.9 GHz
$t_{0,osc1}$	12.0 ps	$t_{0,osc2}$	29.2 ps
τ_{decay1}	>1 ns	τ_{decay2}	37.4 ps
E_{log}	0.63 eV		
τ_{log}	1.6 ps		
$t_{0,log}$	26.0 ps		
E_{osc1}	-0.83 eV	E_{osc2}	-0.16 eV
σ	0.27 eV		
fwhm	2.02 eV		

Table 5.2 Full list of parameters for the time-dependent profiles from fitting of the individual spectra.

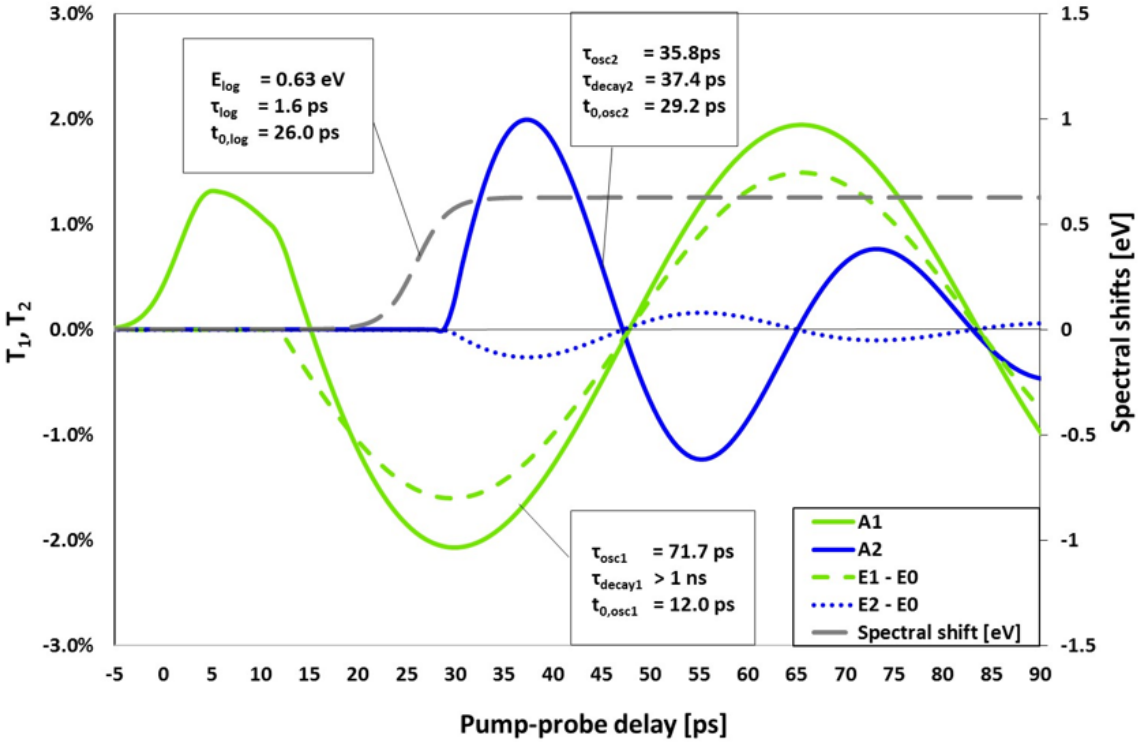

Figure 5.8 The time-dependence of fitting parameters.

From the fitting presented in Figure 5.8, it is seen that the X-ray line amplitude oscillates at the 13.5-GHz fundamental frequency. In addition, the line position exhibits an oscillatory deviation with 1 eV amplitude from the initial line position at 6542.8 eV. The lines shift by about 0.7 eV at 25 ps. This time is in agreement with the 1/e time of the pulse decay shown as a grey curve in Fig. 5.4. This observed shift is interpreted as a solvation shell radius increase. Section 4.2 our simulations showed that simultaneous absorption peak amplitude and position changes are caused by solvation shell radius changes (Figure 4.9). Changes in solvation shell radius cause slight Mn-O bond length changes via the hydrogen bonds between the solute and solvent molecules (Figure 4.5). The solid and dashed curves with 13.7-GHz frequency in Figure 5.8 oscillate simultaneously and in phase, indicating that the simultaneous oscillation of the Mn-O bond lengths and the solvation shell radius. The 27-GHz curves in Figure 5.8 are 90° phase shifted relative to the fundamental wave, as is expected for a 2nd harmonic wave. Its amplitude decay is shown in Figure 5.4. The peak position (dotted line) barely oscillates. The calculations

presented in Section 4.2 show that the only dynamics that changes line amplitude without changing line position is associated with permanganate symmetry deformations and not radial motions. Since the complex is hydrogen-bonded to the surrounding water, the complex deformation is due to transversal water motions, which in turn suggests that the SH wave is a transverse acoustic wave. Combining the amplitude of the X-ray absorption line position oscillation with our simulations, we estimate that the solvation shell radius oscillates with an amplitude of about 0.8 Å. Taking the compressibility of water into consideration, this diameter corresponds to a pressure oscillation of about 1 GPa. Such high pressures can lead make the stress-strain tensor non-linearity, which, in turn, could be the reason for the 2nd harmonic generation.

It is noted that this is the first discovery of SHG of phonons in the vicinity of ions in aqueous solution. This discovery provides new information about the structural properties of the HB network. The decay of the SH wave could be the result of reductions in pressure oscillation amplitude, or a decrease in the solution density. This, however, would be reflected in the simultaneous reduction of the fundamental amplitude and the shift of fitted Logistic(t) function shown in Figure 5.8, which is not the case. An alternative explanation is that the structural changes of the HB network in the domain around our solute diminish the coupling between fundamental and the SH wave, leading to the observed decay of SH phonon. One such coupling mechanism could be the short-lived existence of ice-like stiffness in the electrolyte. This is likely because liquids, such as neat water, do only support transversal waves above a wavenumber of $4 nm^{-1}$.[60] The 27-GHz phonons reported here have wavenumbers of 0.126 nm^{-1} assuming a normal sound speed of 1.36 km/s and 0.063 nm^{-1} assuming a fast sound speed of 2.7 km/s. Neither value is lower than the minimum wavenumber required for transversal waves. Thus, the existence of the transversal phonons indicates that the domains have ice-like stiffness and the measured 37-ps decay of the SH wave may serve as an indicator of the lower limit of the lifetime of ice-like

stiffness in the domains. Having ice-like stiffness, the waves are possible to propagate with a fast sound speed of 2.7 km/s.

Assuming a sound speed of 2.7 km/s and the maximum domain diameter equal to the propagation length of the SH phonons, the diameter of the ice-like domains can be roughly estimated. Again, the 37-ps decay time of the SH phonons is the minimum lifetime of the ice-like structures. It may be even longer because a decay also occurs when the phonons leave the domains, which is where they are detected with the greatest sensitivity. The propagation length of this phonon during this time is estimated to be as large as 100 nm, which is therefore the approximate domain diameter. This diameter is in agreement with the DLS measured domain size distribution. A quantitative estimate of how much the solutes affect the formation of these domains is hard to obtain. As will be discussed in the next Chapter, under identical laser excitation condition, the direct generation of 27.6-GHz phonons is observed in aqueous 30-mM ferrohexacyanide solution. The Brillouin scattering equation can be used to calculate propagation speed of the generated phonons to be 2760 m/s. The fast-sound speed in ferrohexacyanide and the presence of ice-like domain discussed above, supports the hypothesis that the SH waves in permanganate solution also propagate at fast-sound speed.

In conclusion, SH phonons were successfully generated and observed in an aqueous permanganate solution using picosecond time resolved X-ray absorption spectroscopy. In addition, longitudinal and transverse phonons can be unambiguously identified by comparison with theoretically calculated XAS.[115] The decay of the SH conversion efficiency lead to the hypothesis that ice-like structures exist around the solutes. The size of these structures, or domains, are in qualitative agreement with the DLS and SLS measured results.

CHAPTER 6. DIRECT GENERATION OF FAST SOUND PHONONS

6.1 Photochemical Dynamics of Ferrohexacyanide

The pioneering work in the study of ferrohexacyanide photochemical properties was done by Shirom and Stein.[116-117] They identified two primary routes for chemical process, namely, Charge Transfer To Solvent (CTTS) and photoaquation. At excitation laser wavelengths longer than 313nm the dominant process is the formation of photoproducts via the so-called photoaquation channel:

$$[Fe(CN)_6]^{4-} + H_2O \xrightarrow{h\nu} [Fe(CN)_6]^{4-*} + H_2O \rightarrow [Fe(CN)_5OH_2]^{3-} + CN^-.$$

At excitation wavelengths below 313nm the dominant process is photooxidation of the solute via the CTTS. A single ferric electron is ejected into the solvent forming a solvated electron:

$$[Fe(CN)_6]^{4-} \xrightarrow{h\nu} [Fe(CN)_6]^{3-} + e^-_{aq} .$$

There are multiple transitions that may be associated with this process, and which occur upon excitation at different laser wavelengths. The transitions from the ground $^1A_{1g}$ state to the $^3T_{1g}$, $^1T_{1g}$, $^1T_{2g}$, and $^1T_{1u}$ states have probability maxima at 422nm, 322.5nm, 270nm and 218nm respectively[116, 118].

Since the laser excitation wavelength in our experiments was 266nm the products will be excited to the $^1T_{2g}$ state. with two competition process following. The short-lived $^1T_{2g}$ spate is proposed to decay into the lowest singlet state that leads to an aquation process, or go into a

CTTS state which may yield a hydrated electron. These two paths for the excited complex are shown in Figure 6.1.

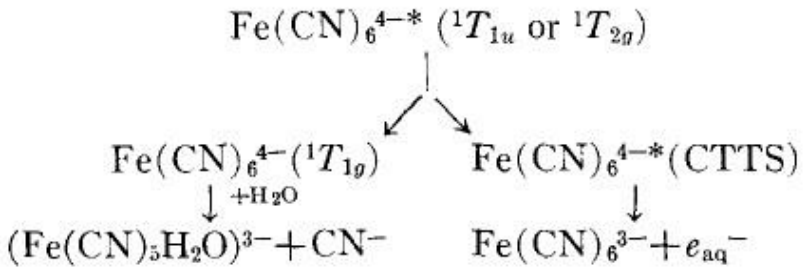

Figure 6.1 The photoexcited state of ferrohexacyanide reaction scheme. Picture taken from Ref [117].

The CTTS process is more dominant than photoaquation, and the quantum yield was found by Reinhard *et al.* to be 3.75%.[119]

Even though photoproducts formation is not dominant under relatively short laser excitation wavelengths, product formation according to Figure 6.1 still occurs. The quantum yield of photoproducts at 254nm was found to be half of that measured at 313 and 365nm. Possible photoproducts were identified as $[Fe(CN)_5H_20]^{3-}$ and $[Fe_2(CN)_{10}]^{6-}$.[117] The work of Reinhard *et al.* supports this statement. They collected spectra around the K-edge of iron complexes (ferrohexacyanide and ferric Hexacyanide solvated in water) at 70ps and 650ps after 266 and 355nm laser excitation. In the analysis of the dynamics initiated by 266nm excitation the static spectra due to different photooxidation products were subtracted from the collected transient spectra. The residual spectra contained features due to non-photooxidation products, and lead them to conclude that 266nm excitation of aqueous ferrohexacyanide leads to the sole production of photooxidates and aquated species. The evolution of spectra between 70ps and

650ps indicates that the evolution of photoproducts can be on the time scale of hundreds of picoseconds.[119]

This Chapter delineates a series of experiments identical to those presented in the previous Chapter that were conducted on aqueous ferrohexacyanide, producing phonons a laser induced transient grating.

6.2 Experimental Data and Analysis

The measured energy spectra are plotted in Figure 6.2. The transmittance change at a specific probing x-ray energy is shown with respect to time. Time zero is defined as the time the laser hit the sample.

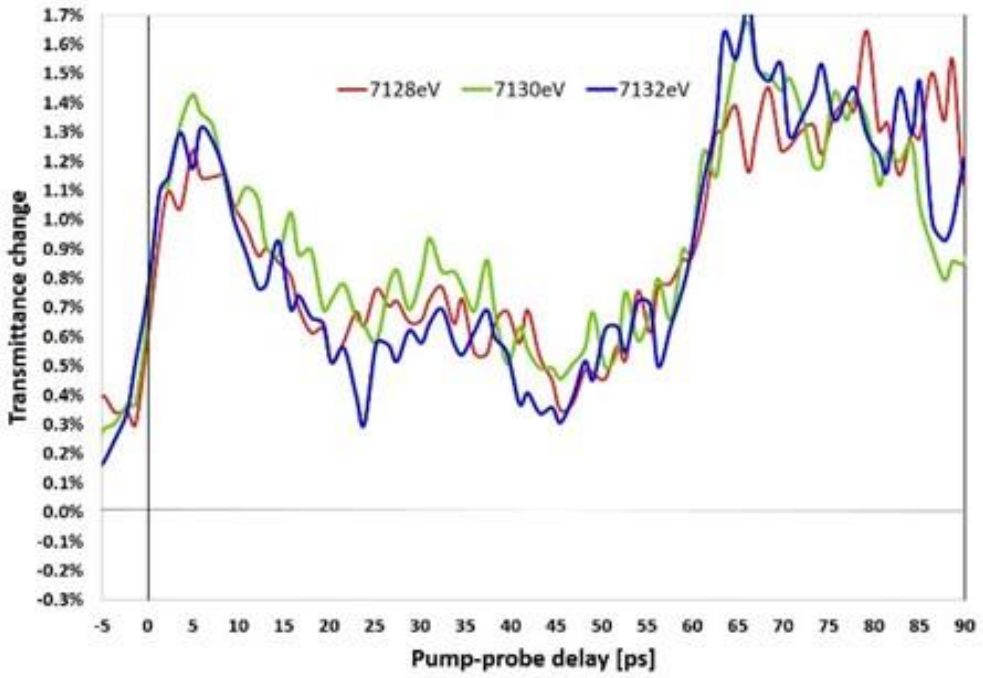

Figure 6.2 Measured transmittance change with respect to time at three probe energy points of 7128, 7130 and 7132eV.

The three kinetic traces show very similar behavior in time domain. When comparing the transmittance changes at early time points, the trace at 7130eV energy has the highest initial transmittance increase, indicating that the absorption cross section change at this point is having the largest negative value. This is in agreement with previous discussed ferrohexacyanide CTTS effect. Lee *et al.* showed with both experimental and theoretical approaches that CTTS causes a blueshift in the K-edge of the sample and a very largest negative change in absorption spectrum at 7130eV.[120]

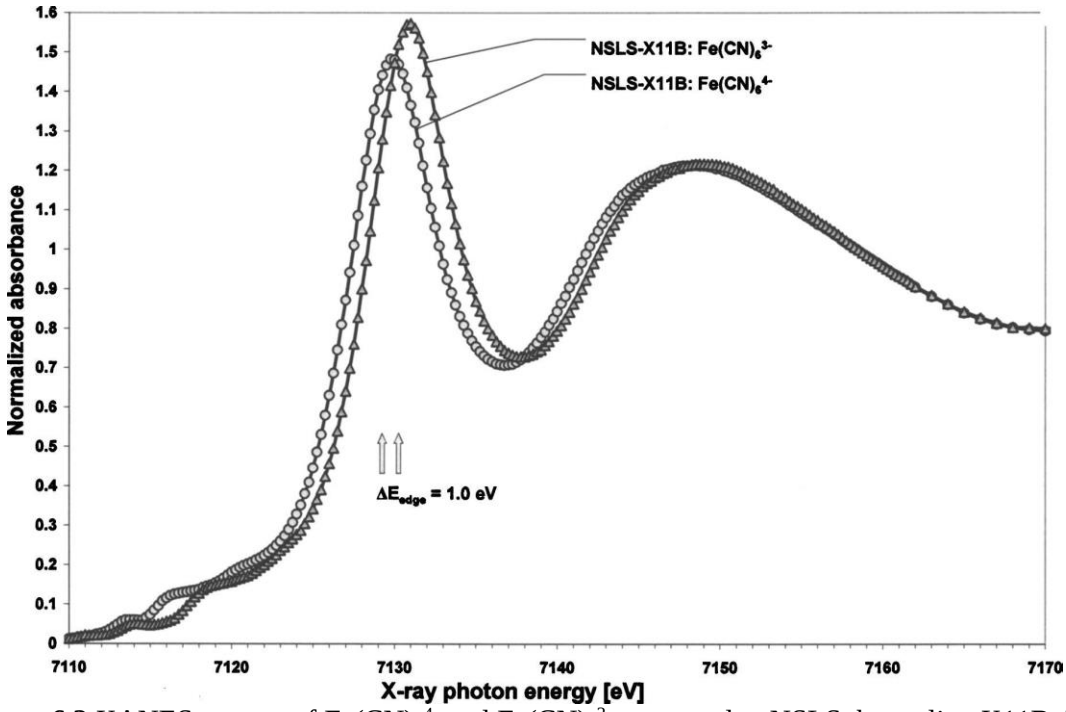

Figure 6.3 XANES spectra of $Fe(CN)_6^{4-}$ and $Fe(CN)_6^{3-}$ measured at NSLS, beam line X11B. The picture is taken from Ref [120].

After 50ps the spectra at 7130 eV no longer has the greatest change in transmittance. The spectra in this time regime is interpreted in terms of photoproduct formation after solute molecule photoexcitation. The quantitative reason why the relative ordering of transmittance changes by probe energy is not in agreement before and after 50ps is difficult to understand due to the

various photoaquation products that may be formed and the precise distribution of these products. The photochemical processes are not the focus of this section. Rather, the common feature of these spectra and the physical dynamic processes are going to be analyzed. Similarly to how the data was processed in Chapter 5, an average was taken for over the spectra taken at the three probing energies to increase data quality and extract the common dynamic process. The averaged kinetic trace is shown in Figure 6.4. The data were fitted with an exponential rise and decay, two oscillations and a product rising peak. The fitting function is shown in Equation 6.1 and a full list of fitting parameters is presented in Table 6.1.

$$\Delta T(t) = A_{pulse} \cdot Pulse(t) + A_{osc\,1} \cdot Oscillation_1(t) + A_{osc\,2} \cdot Oscillation_2(t) + A_{product} \cdot Sigmoidal(t)$$

$$\text{with} \qquad Pulse(t) = \begin{cases} e^{\left(\frac{t-t_{0,pulse}}{\tau_{rise}}\right)} & for\ \ t \le t_{0,pulse} \\ e^{-\left(\frac{t-t_{0,pulse}}{\tau_{fall}}\right)} & for\ \ t > t_{0,pulse} \end{cases}$$

$$\text{and for } i = 1,2 \qquad Oscillation_i(t) = \begin{cases} 0 & for\ \ t \le t_{0,osc\,i} \\ e^{-\left(\frac{t_{0,osc\,i}-t}{\tau_{decay\,i}}\right)} sin\left(2\pi \frac{t-t_{0,osc\,i}}{\tau_{period\,i}}\right) & for\ \ t > t_{0,osc\,i} \end{cases} \qquad (6.1)$$

$$Sigmoidal(t) = \begin{cases} 0 & for\ \ t \le t_{0,product} \\ 1 - e^{-\left(\frac{t-t_{0,product}}{\tau_{rise}}\right)^2} & for\ \ t > t_{0,product} \end{cases}$$

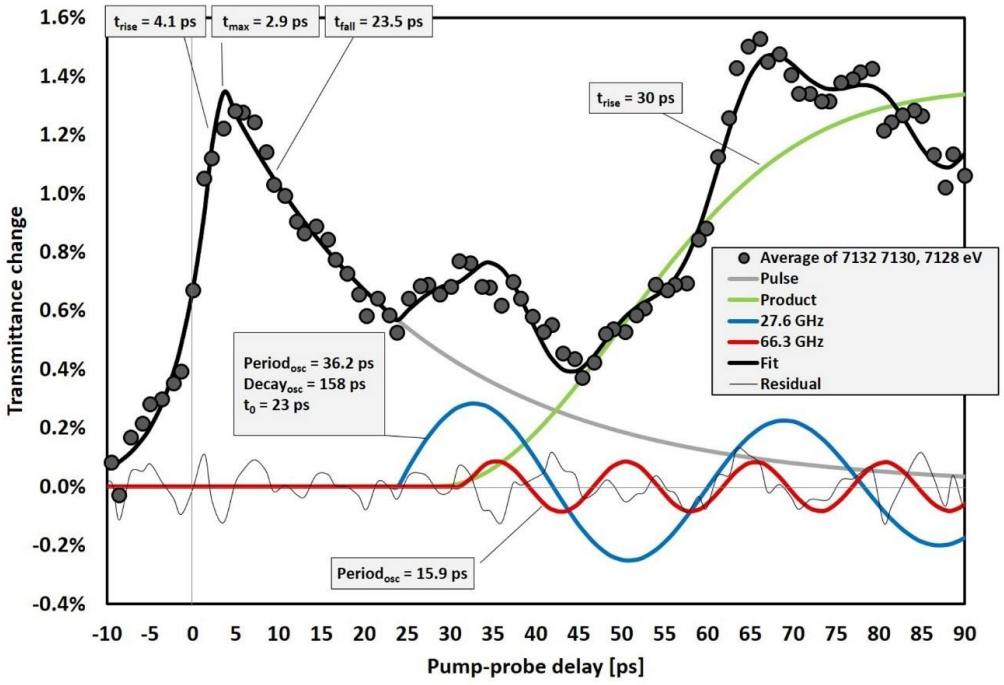

Figure 6.4 Average of transmittance change with respect to time at three probe energy points.

Figure 6.4 contains the transmittances changes averaged over the K-edge peak maximum (7130 eV) as well as 2eV above and below this peak. At zero probing time delay the transmittance rises with a time constant of 4.1 ps, which actually almost reach the instrument-limited resolution. The transmittance change increase is followed by a 23.5 ps time constant decay. At 23 ps a 27.6 GHz oscillation was initiated at with a lifetime of 158 ps. There is a higher frequency oscillation identified from the fitting process. The oscillation amplitude is so small that it is statistically insignificant, and therefore not attributed to a physical process. There is a final transmittance change increase tens of picoseconds after laser excitation. The increased transmittance change cannot be classified as an isolated increase or as a component of an oscillatory feature, because of the temporal observation window size. However, an increasing function used to describe formation of photoproducts fits the data well.

This increase is interpreted as $[Fe(CN)_5H_2O]^{3-}$ and $[Fe_2(CN)_{10}]^{6-}$ photoproduct formation as presented in Section 6.1. These photoproducts have been theoretically calculated by Lee *et al*. to have lower absorption cross sections at the experimentally measured points, causing the increase of transmittance signal shown in Figure 6.5.[120]

Pulse Peak Amplitude [%]	1.38
Pulse Peak Rise Time [ps]	4.12
Pulse Decay Time [ps]	23.48
Oscillation 1 Amplitude [%]	0.30
Oscillation 1 Frequency [GHz]	27.6
Oscillation 1 Initiation Time [ps]	23.85
Oscillation 1 Decay Time [ps]	158.04
Oscillation 2 Amplitude [%]	0.09
Oscillation 2 Frequency [GHz]	66.3
Oscillation 2 Initiation Time [ps]	31.59
Oscillation 2 Decay Time [ps]	1000
Photoaquation Products Peak Rise Time [ps]	29.89
Photoaquation Products Peak Initiation Time [ps]	28.53

Table 6.1 A full list of parameters of the fitted functions of the averaged kinetic traces measured around 7130eV.

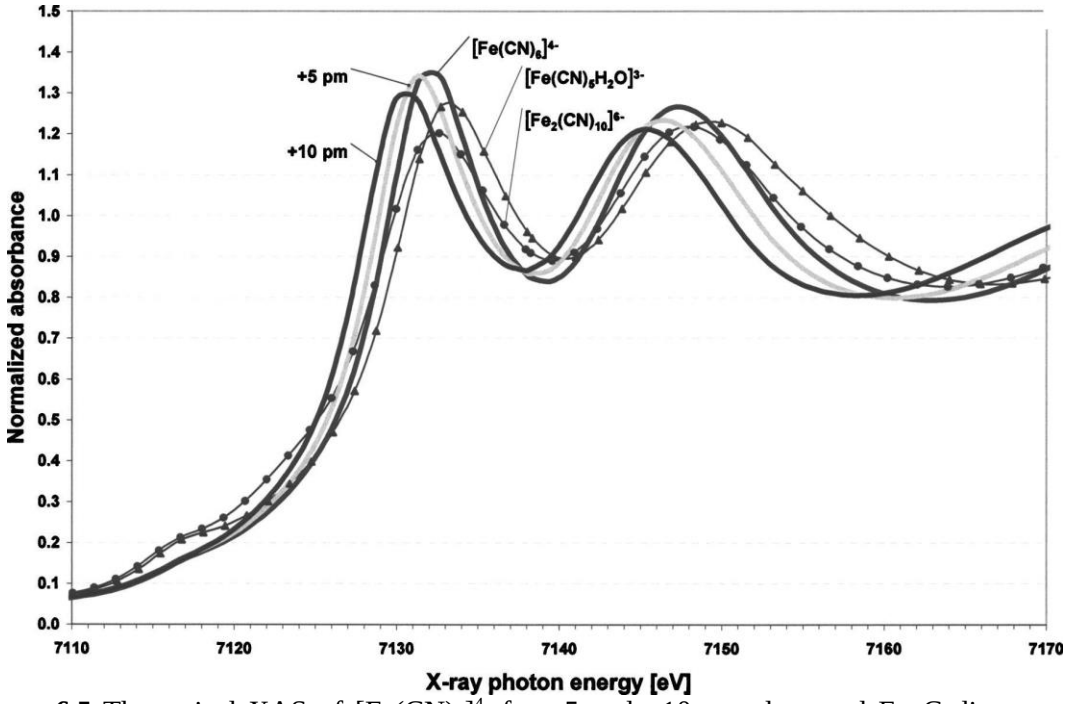

Figure 6.5 Theoretical XAS of $[Fe(CN)_6]^{4-}$ for +5 and +10 pm elongated Fe–C distances but fixed C–N bond length. Additionally, theoretical XANES spectra for the two possible photoaquation product complexes shown. Picture taken from Ref [120].

The pulse response around 3ps is due to the strong laser pumping. High laser intensities will induce substantial electrostriction, excite the solute molecule into photoexcitation states, and may temporarily shift the energies of the molecular orbitals out of the spectral X-ray window under probing.[112, 119] These effects lower the solutes X-ray absorption cross section at our probe energies, thereby increasing the observed X-ray transmittance of the sample. The details for these initial processes cannot be obtained under the current experimental setup, yet some physical processes can still be expected. Undoubtedly, the initial excitation will result in thermal excitation of the solute that will increases the Debye-Waller factor of the X-ray absorption spectrum. As a consequence, transmittance at the K-edge increases. It then decreases as the solute thermally relaxes with a time constant of 23.5ps, which is in agreement with typical thermal relaxation time of this solute in aqueous solution.[121]

The 27.6-GHz oscillation is too slow to correspond to any normal mode of the solute. An oscillation of this frequency was observed in permanganate aqueous solution as well, indicating the general existence of coherent oscillations of groups of molecules in the solvent shell that are coupled to the solute. These coherent oscillations, with hundreds of correlation time, indicates the existence of phonons induced by laser pumping. Using an index of refraction n of 1.33 at the laser wavelength λ_{laser} and the equation presented in Chapter 5, the period of the transient grating $\lambda_{grating}$ is equal to 100nm, which is also the acoustic phonon wavelength. This wavelength multiplied by the measured 27.6 GHz oscillation frequency yields a phono propagation speed of 2760m/s. This value is close but not equal to the literature's high-frequency sound speed $c\infty$ = 3150 m/s below 300 K.[122] It is noted that phonons in water at room temperature do not propagate at the high-frequency sound speeds unless they have large wavenumbers, i.e. high frequencies. In those measurements, c_∞ is, along with the adiabatic sound speed, a parameter that is used to fit the actually measured sound speed. In the domains understudy here, we directly measured that the phonons propagate with the high-frequency sound speed c_∞. The high-frequency limit is reached when the inverse angular frequency τ of the phonons is much smaller than the structural relaxation time constant. Here $\tau = 1/(2\pi * 27.6\ \text{GHz}) = 5.8$ ps. This is much smaller than the observed decay time of 158 ps, which is the lower limit for the lifetime of the ice-like domain structures, as will be discussed below.

The high frequency sound speed c_∞ is related to the bulk modulus K and the mass density ρ through

$$K = c^2 \rho \tag{6.2}$$

Thus, for a given sound speed the modulus is lowest for the lowest density. Light scattering experiments have shown that the domains have a higher density than the surrounding solution, let alone neat water.[11] Therefore, the lower limit of a solutions' bulk modulus, i.e. its lowest possible value, is that of neat water. The density of water at room temperature (996.6 g/L) and the

measured c_∞ = 2760 m/s can then be inserted into eq. (6.2) and the domains' lowest possible bulk modulus can be obtained to be 7.6 GPa. This value is 3.5 times larger than water's low-frequency value. Obviously, the domains have ice-like, high-frequency stiffness at room temperature. A more realistic estimation of the lower limit of the domains' lower bulk modulus can be further made by remembering that adiabatic moduli increase with increasing ionic strength of the solutions, in particular for $K_4Fe(CN)_6$.[123] Santucci *et al.* reported a high-frequency sound speed in neat water $c_{\infty,water,<300K}$ = 3150 m/s below ~300K.[122] Eq. (6.2) implies a high-frequency bulk modulus of neat water $K_{\infty,water,<300K}$ between 9.1 GPa and 9.9 GPa when using the density of ice (916.7 g/L) or liquid water, respectively. These moduli for neat water were taken as the minimum values for the solution domains understudy. These values also are used below to estimate the lower limit of the solute concentrations in the domains.

The relation between the concentration C in mmol/L of ferrocyanide solution and its mass density in g/cm³ can be experimentally measured, as shown in Figure 6.6 and equation (6.3).

$$\rho = 2.27 \cdot 10^{-4}\, C + 1.0 \tag{6.3}$$

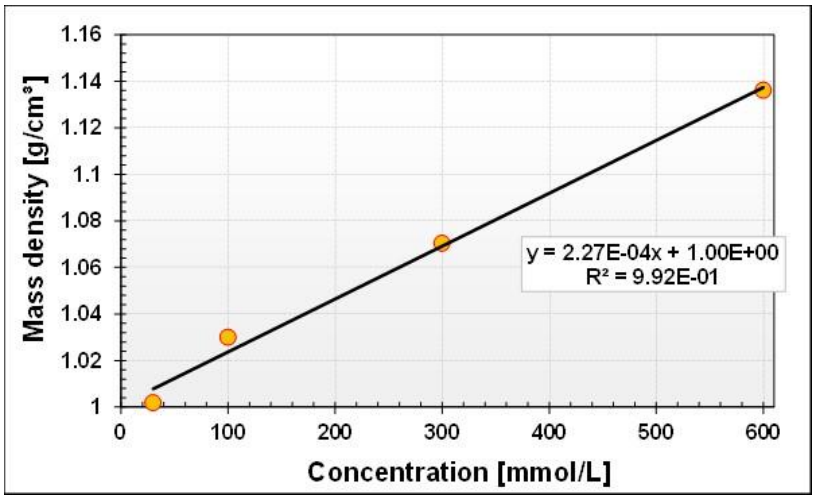

Figure 6.6 Measured densities of aqueous solution iron hexacyanide at room temperature.

Combining eqs. (6.2) and (6.3), an equation that relates the measured sound speed and the bulk modulus to the solute concentration in the domains can be obtained.

$$C = 4405.3\left(\frac{K}{c^2} - 1\right) \tag{6.4}$$

While the exact values of the solutions' moduli on the picosecond timescales are not known, they will be higher than those for neat water. Thus, inserting the lower limits of the bulk moduli $K_{\infty,water,<300K}$ and the measured sound speed into eq. (6.4) yields the lower limit for the domains' concentration C to be between 877 mM and 1350 mM. It can be seen that the domains' concentrations are at least 30 times higher than the average solution concentration. The domains' densities ρ are calculated from eq. (6.3) to be between 1195 g/cm³ and 1298 g/cm³.

The measured 158 ps decay time of the SBS-induced oscillation is limited by the lifetime of the domains' ice-like stiffness and their diameter. While their relative contributions to the decay time are unknown, their lower limits can be calculated. The lower limit of the average domain diameter is estimated for the case that the life-time is not limiting the measured signal. Then the amplitude decays when the phonons are leaving the domains. During this time, they propagate 435 nm, which is therefore the minimum average domain diameter. This value is in agreement with domain diameters measured by SLS and DLS.[12] Only a small fraction of the waves is reflected at the domains' boundaries. Using the density and the measured sound speed, the specific acoustic impedance Z = ρc can be calculated to be $2.9 \cdot 10^6$ kg/m²s and is 2 times higher than that of neat water. The resulting pressure ratio of the reflected and the outgoing waves is 33%. It is likely the impedance transition between the domains and their surroundings is gradual, the back-reflection will be less than that and can thus be ignored. If the domains' diameters are not the limiting factors, the measured decay time is the lower limit of the lifetime of the domains' ice-like stiffness. Thus, the domains are of at least 435-nm diameter and retain their stiffness for at least 158 ps.

In order to check whether the phonon generation effects can be further enhanced, the sample solution was pumped with higher laser intensity in comparison with the Figure 6.4 laser pump peak intensity. The laser peak intensity was increased to $4.3*10^{14}$ W/cm^2. The data is shown in Figure 6.7 and a full list of fitting parameters for this spectra is presented in Table 6.2.

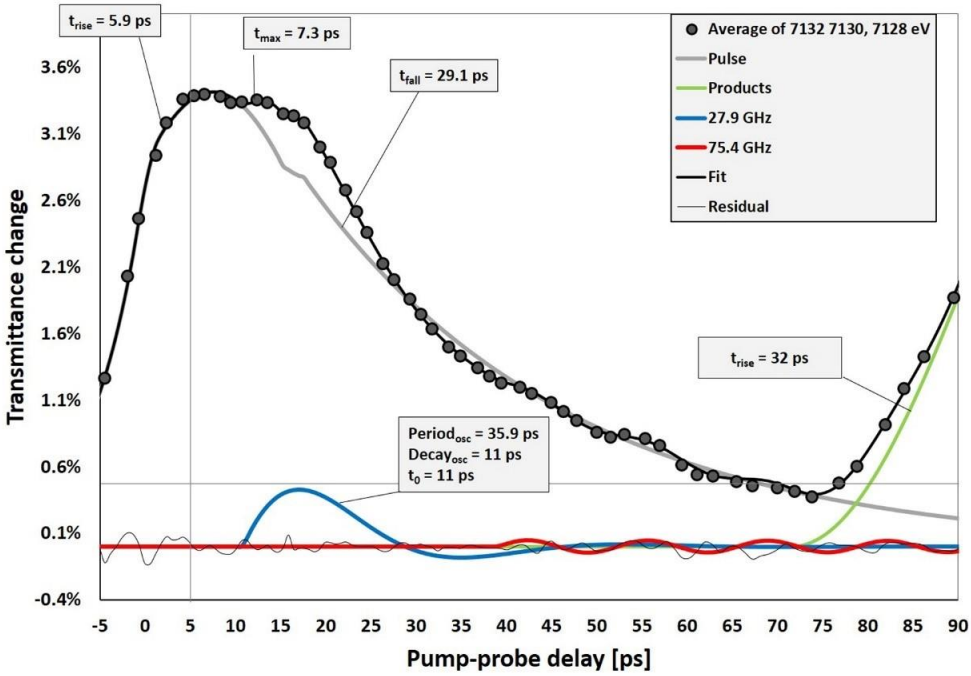

Figure 6.7 Transmittance change with respect to time under higher laser pumping energy.

From Figure 6.7, when the pump laser intensity is increased, the laser induced pulse shape is three times higher than the one in Figure 6.4. There is a saturation effect at the position of the transmittance change global maxima. The thermal decay time is longer than the time in Figure 6.4, possibility due to higher solute vibrational energy. The saturation effect at the maxima was fit with a Gaussian shape and the others features were fitted with the same functions shown in Equation 6.1. The fitting equation in its entirety is shown in Equation 6.5 and a full list of fitting results is presented in Table 6.2.

$$\Delta T(t) = Pulse(t) + A_{osc\,1} \cdot Oscillation_1(t) + A_{osc\,2} \cdot Oscillation_2(t) + A_{product} \cdot Sigmoidal(t)$$

with

$$Pulse(t) = \begin{cases} A_{pulse,rise} \cdot e^{\left(\frac{t-t_{1,pulse}}{\tau_{rise}}\right)} & for\ \ t \le t_{rise,pulse} \\ A_{pulse,saturation} \cdot e^{-\frac{1}{2}\left(\frac{t-t_{pulse,saturation}}{\sigma}\right)^2} & for\ \ t_{rise,pulse} < t \le t_{fall,pulse} \\ A_{pulse,fall} \cdot e^{-\left(\frac{t-t_{2,pulse}}{\tau_{fall}}\right)} & for\ \ t > t_{fall,pulse} \end{cases}$$

and for $i = 1,2$

$$Oscillation_i(t) = \begin{cases} 0 & for\ \ t \le t_{0,osc\,i} \\ e^{-\left(\frac{t_{0,osc\,i}-t}{\tau_{decay\,i}}\right)} sin\left(2\pi \frac{t - t_{0,osc\,i}}{\tau_{period\,i}}\right) & for\ \ t > t_{0,osc\,i} \end{cases}$$

$$Sigmoidal(t) = \begin{cases} 0 & for\ \ t \le t_{0,product} \\ 1 - e^{-\left(\frac{t-t_{0,product}}{\tau_{rise}}\right)^2} & for\ \ t > t_{0,product} \end{cases}$$

(6.5)

Pulse Peak Rise Time [ps]	5.86
Rise end Time [ps]	0.18
Saturation Peak Amplitude [%]	3.44
Saturation Peak Center [ps]	7.25
Pulse Decay Start Time [ps]	16.27
Pulse Decay Time [ps]	29.08
Oscillation 1 Amplitude [%]	0.86
Oscillation 1 Frequency [GHz]	27.9
Oscillation 1 Initiation Time [ps]	10.84
Oscillation Decay Time [ps]	10.94
Oscillation 2 Amplitude [%]	0.05
Oscillation 2 Frequency [GHz]	75.4
Oscillation 2 Initiation Time [ps]	39.46
Oscillation 2 Decay Time [ps]	405.83
Product Rise Time [ps]	31.80
Product Initiation Time [ps]	71.55

Table 6.2 A full list of parameters of the fitted functions of the averaged kinetic trace, pumping with higher laser energy.

The fitting reveals a phonon with a 27.9-GHz frequency. This is almost the same frequency as shown in Figure 6.4. the oscillation amplitude increased from 0.4% to 0.86% by increasing pump laser intensity. The lifetime of phonons produced with higher pump energy is greatly reduced. The decay time changed from 158 to 12ps, indicating that the phonon propagation length is greatly reduced. This may be explained by the fact that at sufficiently high laser energies water splits due to multiphoton absorption producing a high concentration of solvated electrons, as

discussed in the Section 2.2. These solvated electrons will exist on the scale of nanoseconds and form local cavities surrounded by water molecules. The cavities about the solvated electrons break the geometric regularities of bulk water.[124-126]

The photoaquation product formation is delayed by ~20ps relative to lower excitation energy. This may also be because the HB network is perturbed, and therefore the mobility necessary for photoproduct formation is changed. Photoproduct formation initiation on the time scale of tens to hundreds of picoseconds is still in agreement with the work of Reinhard *et al*.[119]

The oscillation decay time of the 27 GHz acoustic phonons generated in 50-mM $KMnO_4$ was 40 ps. This is much shorter than the decay time observed for phonons of the same frequency generated in ferrohexacyanide solution. A possible explanation is that the ionic strength of $K_4Fe(CN)_6$ is six times higher than that of $KMnO_4$, leading to a more rigid HB network. A higher anionic charge also decreases the mobility of water molecules in the solvation shells.[127] The HB rearrangement proceeds through jumps and rotations of groups of hydrogen bonded water molecules, which is the so-called frame tumbling.[5] The jump frequency has a slight dependence on anion concentration. Frame-tumbling has a relatively stronger dependence on anion charge, and slows down with increasing charge.[128] $[Fe(CN)_6]^{4-}$ orients water molecules up to a radius of 1 nm,[129] i.e. a volume that containing about 140 water molecules. This number is equal to the ratio of $[Fe(CN)_6]^{4-}$ and H_2O at our estimated domain minimum concentration. Thus, even ignoring all K^+ cations the anions' solvation shells overlap, which results in a substantial increase of frame tumbling times and a longer decay time for the hexacyanide domains. The quantitative connection between the results here and thermodynamics quantities, like the solvation entropy change of ions, cannot be obtained. The results presented do indicate that the use of solute molecules as molecular dynamic probes provides a new approach to the study of ion "structure making/breaking" effects. This solute probe technique measures effects on the hundreds of nanometer, or mesoscopic spatial scale.

In summary, phonons propagating at “fast-sound” speed with lifetimes of ~160ps were detected. This time is the lower limit of the lifetime of ice-like stiffness of high solute concentration domains in the sample. The domain diameter is at least 400 nm. The solute concentration inside the domains was estimated to be one order of magnitude higher than the average concentration of the solution.[130]

6.3 2D Surface Creation and Analysis

A systematic variation of the probing X-ray photon energy was done, and time-dependent kinetic traces were combined into a 2D surface. Transmittance change is expressed as a function of x-ray probing photon energy and time. The surface is shown in Figure 6.8.

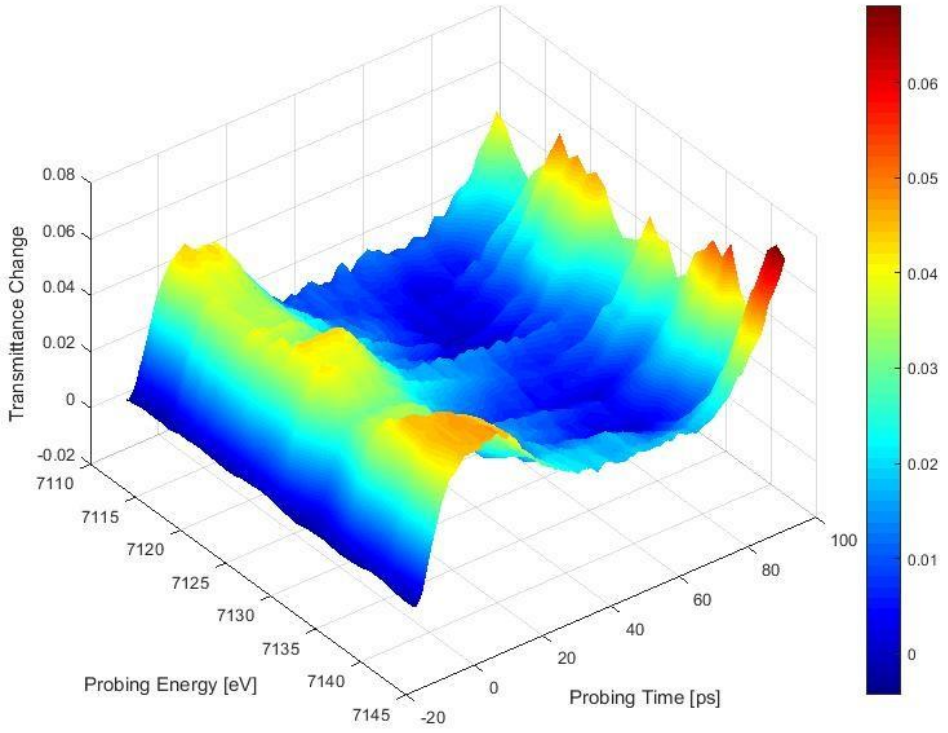

Figure 6.8 2D Surface for the analysis of the photophysical and photochemical dynamics. Here, the transmittance change is plotted with respect to the Probing x-ray photon energy and probing time after laser hit the sample.

The surface contains information characteristic of the CTTS, transient grating induced acoustic phonons and photoproduct formation. A very accurate quantification of this surface turns out to be a challenging problem and has not been completed as part of this thesis. As is discussed in the Chapter 3, the laser and X-ray sources are both tens of meters away from the sample. A very slight drift in an optical element upstream induces large drifts in beam pointing at the sample. Even though a beam pointing stabilizer was used, there was still some laser pointing drift when the pump-probe data collection would span a few hours. For longer data acquisition times, on the order of several days as needed for this surface, acquisition had to be paused, and the laser-x-ray spatial overlap had to be adjusted/checked. Therefore, the surface data shown are composed of

several individual scans done over several days. The uncertainty of physical conditions between these scans caused the statistics between different scans to fluctuate, making a global fit challenging. Further work with our theoretical collaborator is being planned.

CHAPTER 7. CHEMICAL PROPERTY STUDY OF CLATHRATE HYDRATES-PROJECT ONGOING

7.1 Experimental Procedures of Electrochemical Study of Clathrate Hydrates

Clathrate hydrates are aqueous cage structures that may host a guest molecule. Carbon dioxide has an increased solubility in clathrate hydrate relative to liquid water. Clathrates were used as an electrolyte solution in an electrochemical cell with the intention of providing a higher CO_2 density to the working electrode.

Clathrate were made with a 0.1M $KHCO_3$ aqueous solution that was 10% THF by mass. A custom designed clathrate hydrate batch reactor was constructed, and is shown in Figure 7.1.

Figure 7.1 Batch reactor constructed for making the clathrate electrolyte solution. The inner chamber contains a helical Teflon pedal that continuously stir the electrolyte solution. The entire vessel is gas tight and placed under CO_2 pressure slightly higher than 1 atm. The whole system temperature was controlled by a chiller to be constantly 2°C.

The electrolyte solution containing THF was placed into the batch reactor and mechanically stirred at 130 rpm. The reactor temperature was kept at 2°C. The formed clathrate hydrates are presented in Figure 7.2.

Figure 7.2 Picture of Clathrate Hydrates made with the bath reactor.

Electrolysis was performed with an H-type cell made of Teflon. The two compartments of the cell were separated by a Nafion proton-exchange membrane (Nafion 117, DuPont). The cell was designed with the aim of maximizing the conductivity of the whole electrolysis system by making the Nafion membrane area as large as possible. The working electrode was a planar piece of copper, held at -1.3V vs Ag/AgCl., In order to maximize the concentration of the product gas, the void space above the liquid surface was minimized. To guarantee that clathrate hydrates were in contact with the working electrode a pedal driven by a rotating shaft was used to stir the solution.

The entire cell was placed in an aluminum housing coupled to a cooler. The cooler maintained the electrochemical cell at 2°C to guarantee the existence of clathrate hydrates.

A custom GC-mass spectrometer coupled system was used to quantify the gas-phase electrochemical products. A Varian 3900 GC equipped with a carbon plot column was. The FID detector enabled detection of hydrocarbon products to ~5ppm accuracy. Inside of the GC column oven, a Y-branch was used to separate the sample gas into two fractions. The first fraction of the gas sample was routed to the FID detector for hydrocarbon identification. The second fraction of the gas sample was routed to a SRS 200 mass spectrometer for the detection of H_2 and CO. The detection limit for H_2 and CO was found to be ~50ppm. Figure 7.3 shows a 15ppm gas mixture calibration spectra containing different hydrocarbon products. The different products appear at different elution times and are labeled accordingly.

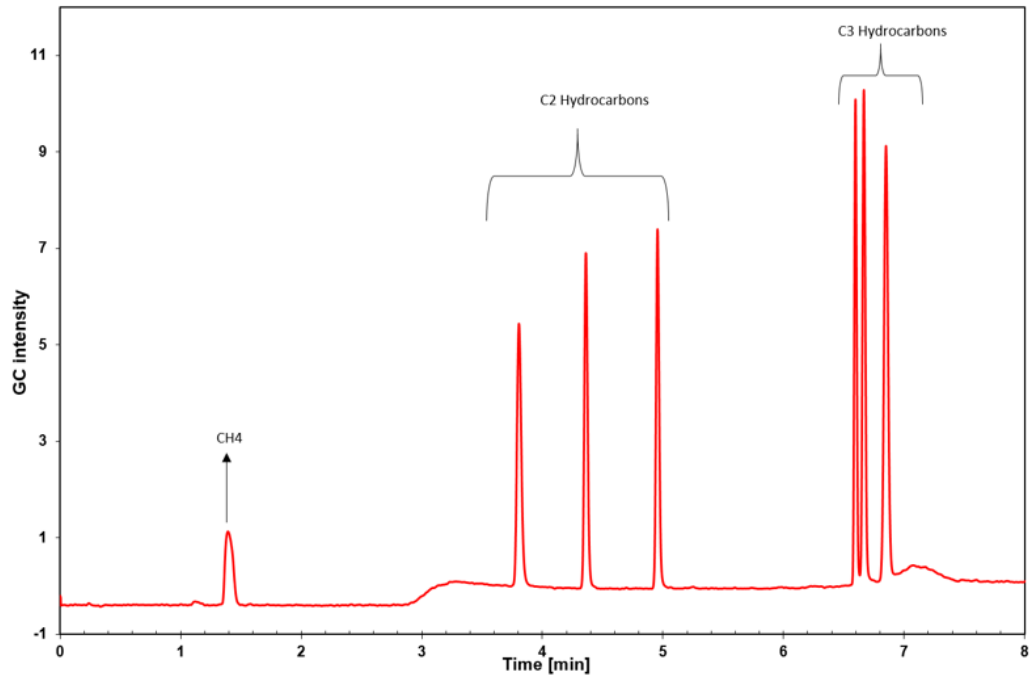

Figure 7.3 Gas Calibration with mixture of 15ppm Hydrocarbons gases. The gases were separated based on their retention times in the GC column, with C1 gas peak at 1.4min, C2 gases between 4 and 5min and C3 gases between 6.5 and 7min.

7.2 Preliminary Results

Figure 7.4 shows the GC spectra of gaseous products produced by electrolysis with an electrolyte solution devoid of clathrate hydrates. The electrolyte solution is chemically identical to the clathrate containing solution save for the presence of ice-like cages. Figure 7.5 contains the GC spectra of gaseous products produced by electrolysis with a clathrate containing electrolyte solution.

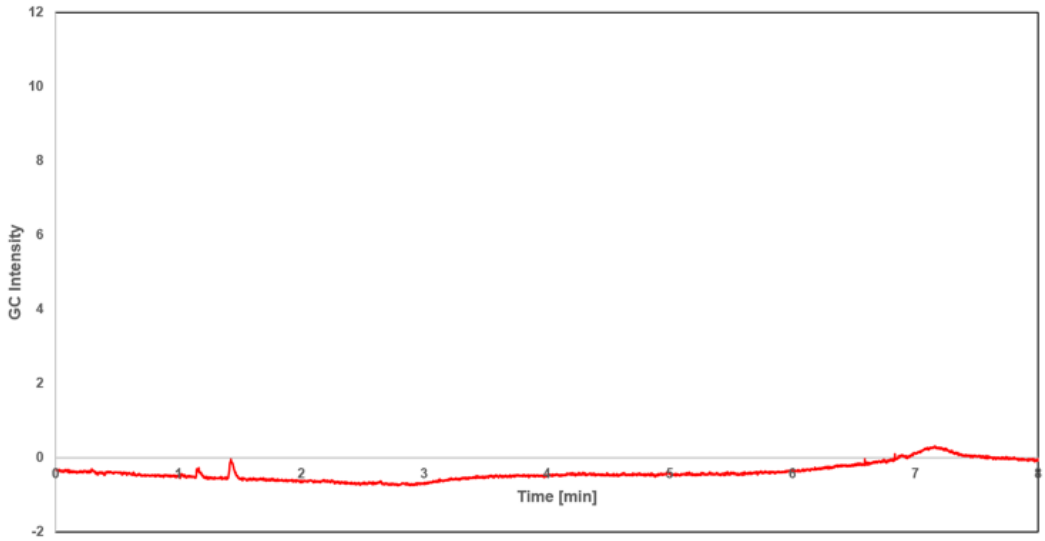

Figure 7.4 The GC spectra of the electrolysis gas products without Clathrate Hydrates. Under the current experimental condition, there seems to be only one peak indicating the existence of CH_4.

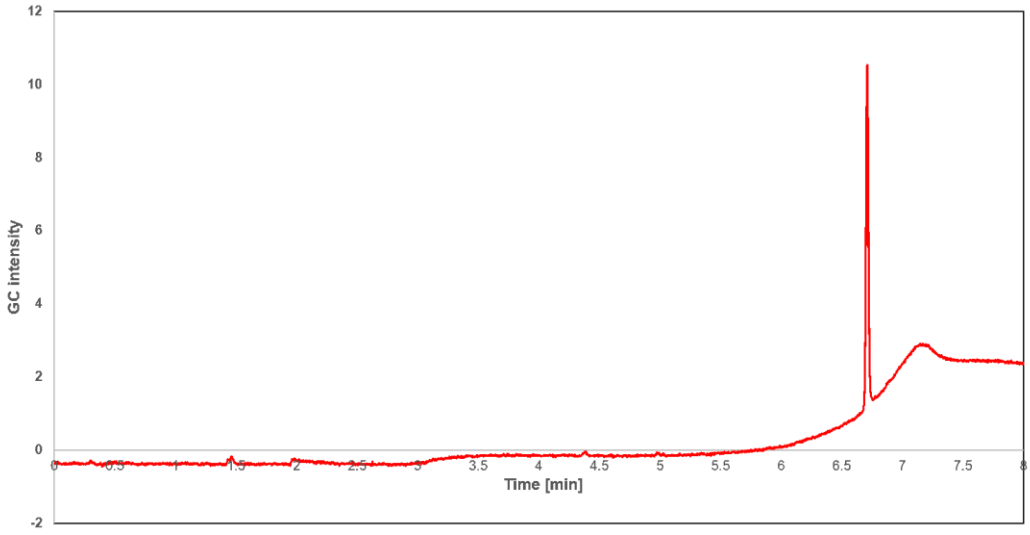

Figure 7.5 The GC spectra of the electrolysis gas products with Clathrate Hydrates. Under the current experimental condition, a very large peak around 6.8min shows up, indicating a relatively high yield of C3 hydrocarbon products.

I would like to emphasize that these results are just preliminary, not conclusive. Comparing Figure 7.4 and Figure 7.5, the presence of clathrate hydrates seems to not only suppress the formation of C1 and C2 hydrocarbons, but promote C3 hydrocarbon formation under the given electrochemical conditions. We speculate that the nanoscale clathrate hydrate cages serve as a delivery mechanism of high concentration CO_2 to the immediate vicinity of the working electrode, and may even be directly involved in the reduction reaction. The clathrate cages could be involved in the reaction through their contact with the electrode, and the electrochemical reaction could even happen inside of the cage. The cages may also inhibit intermediates from diffusing freely, the so-called “caging” effects, promoting the formation of C3 hydrocarbon gaseous products.

A systematic variation of reduction potentials and analysis of the resulting products for the purpose of calculating reaction Faraday efficiencies is ongoing. We are also investigating the potential for conducting theoretical calculations to simulate electrochemical experiments using clathrate hydrates.

CHAPTER 8. CONCLUSIONS AND OUTLOOK

The results of the x-ray work presented in this thesis elucidate ion-induced effects on aqueous solution structures by experimentally confirming the generation and propagation of phonons in these systems. The results may be summarized; Phonons can be created through the generation of a transient grating, and can be detected using solute molecules as a probe. This method enables the detection of locally propagating phonons that are difficult to detect via scattering techniques. The presence of second harmonic, transversal phonons suggests the existence of ice like domains in aqueous solutions. The domain sizes were estimated to be on the hundred nanometer scale, and are dependent on the charge and ionic strength of solutes in the aqueous solution.

27-GHz phonons were detected in the experiments described in Chapter 5 and Chapter 6. This frequency is strongly reminiscence of the Debye relaxation frequency. To better understanding of the periodic features seen in the absorption spectra, a Fourier transformation of the fitted damped oscillatory feature from Figure 6.4 was conducted. The resultant curve in the frequency domain is shown below:

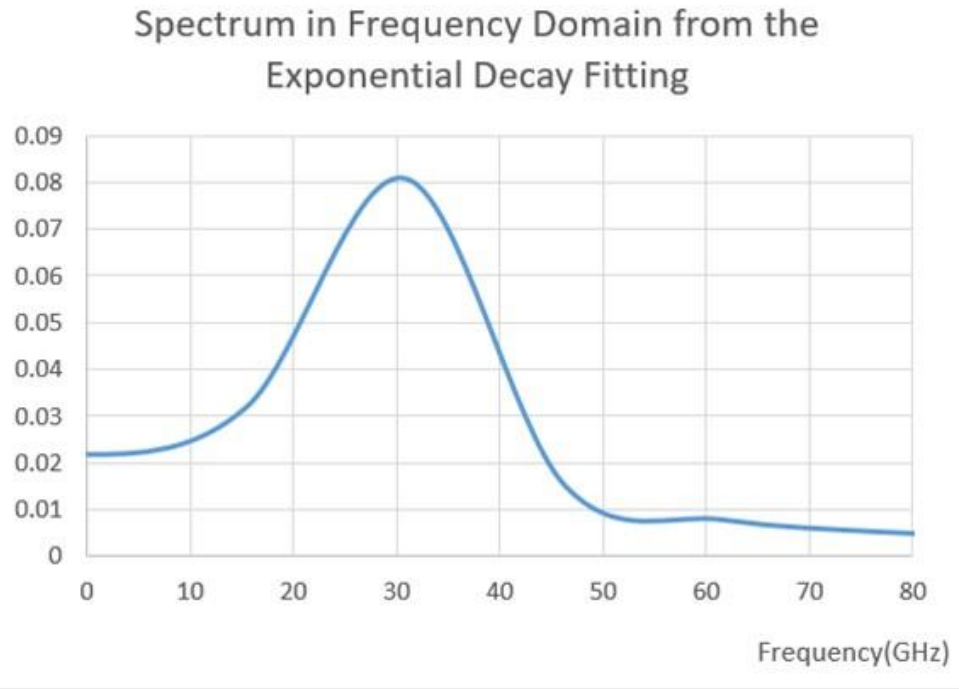

Figure 8.1 The FFT result of the 28-GHz damped oscillatory feature shown in Figure 6.4.

The maxima of the frequency spectrum shown in Figure 6.4 is located similarly to the maxima in the dielectric loss spectra of a NaCl The dielectric loss spectra of a NaCl solution is shown in Figure 8.2.[131]

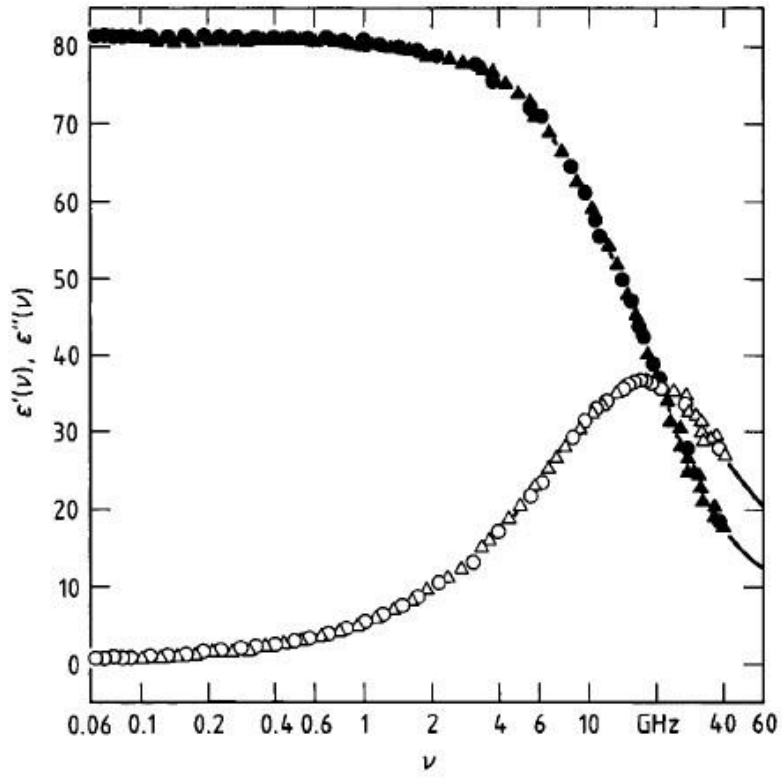

Figure 8.2 The dielectric spectra of 0.051M aqueous solution of NaCl at 20 °C, with closed symbols representing the real part and open symbols representing imaginary part. The picture is taken from Ref [131].

The presence of a 27-GHz phonon in each of the salt solutions discussed in this thesis, and the similarity between the FFT of the function used to fit this oscillatory feature and the dielectric loss spectra of NaCl solution suggests that there are structural features of the HB network in the local environment of solute molecules that are independent of solute identity and concentration. In order to remove the speculation in this claim a number of subsequent experiments could be carried out. Phonon frequency is strongly dependent upon the transient grating frequency, so the effect of varying grating fringe spacing on phonon generation could be studied by changing the pump laser wavelength. Systematic variation of ion strength, charge, and concentration as well as temperature would also elucidate solute effects on the surrounding HB network.

With regard to the electrochemical reduction of CO_2, the use of a platinum working electrode instead of copper could further indicate the significance of the role clathrates play in the promotion of higher hydrocarbon production. The use of platinum for the reduction of carbon oxide is limited by electrode poisoning. When carbon monoxide is produced, it is forms a monolayer on the electrode surface preventing further carbon reduction from occurring and promote the hydrogen evolution reaction[132,133]. If the reduction of carbon dioxide occurs inside of the clathrate cages electrode poisoning should be irrelevant. Experiments utilizing a platinum working electrode are being conducted presently.

REFERENCES

1. Agmon, N., Tetrahedral Displacement: The Molecular Mechanism behind the Debye Relaxation in Water. *J. Phys. Chem.* **1997,** *100*, 1072-1080.

2. Cunsolo, A.; Ruocco, G.; Sette, F.; Masciovecchio, C.; Mermet, A.; Monaco, G.; Sampoli, M.; Verbeni, R., Experimental Determination of the Structural Relaxation in Liquid Water. *Phys. Rev. Lett.* **1999,** *82*, 775-778.

3. Ronne, C.; Thrane, L.; Åstrand, P.-O.; Wallqvist, A.; Mikkelsen, K. V.; Keiding, S. R., Investigation of the temperature dependence of dielectric relaxation in liquid water by THz reflection spectroscopy and Molecular Dynamics simulation. *J. Chem. Phys.* **1997,** *107*.

4. Laage, D.; Hynes, J. T., On the molecular mechanism of water reorientation. *J. Phys. Chem. B* **2008,** *112*, 14230-14242.

5. Laage, D.; Stirnemann, G.; Sterpone, F.; Rey, R.; Hynes, J. T., Reorientation and Allied Dynamics in Water and Aqueous Solutions. *Annu. Rev. Phys. Chem.* **2011,** *62*, 395-416.

6. Kropman, M. F.; Bakker, H. J., Dynamics of Water Molecules in Aqueous Solvation Shells. *Science* **2001,** *291*, 2118-2120.

7. Omta, A. W.; Kropman, M. F.; Woutersen, S.; Bakker, H. J., Influence of ions on the hydrogen-bond structure in liquid water. *J. Chem. Phys.* **2003,** *119*, 12457.

8. Omta, A. W.; Kropman, M. F.; Woutersen, S.; Bakker, H. J., Negligible Effect of Ions on the Hydrogen-Bond Structure in Liquid Water. *Science* **2003,** *301* (5631), 347-349.

9. Chen, Y.; Okur, H. I.; Gomopoulos, N.; Macias-Romero, C.; Cremer, P. S.; Petersen, P. B.; Tocci, G.; Wilkins, D. M.; Liang, C.; Ceriotti, M.; Roke, S., Electrolytes induce long-range

orientational order and free energy changes in the H-bond network of bulk water. *Science Advances* **2016,** *2*, e1501891.

10. Shelton, D. P., Long-range orientation correlation in water. *J. Chem. Phys.* **2014,** *141*, 224506.

11. Sedlak, M., Large-Scale Supramolecular Structure in Solutions of Low Molar Mass Compounds and Mixtures of Liquids: I. Light Scattering Characterization. *J. Phys. Chem. B* **2006,** *110*, 4329-4338.

12. Georgalis, Y.; Kierzek, A. M.; Saenger, W., Cluster Formation in Aqueous Electrolyte Solutions Observed by Dynamic Light Scattering. *J. Phys. Chem. B* **2000,** *104*, 3405-3406.

13. Sedlak, M., Large-Scale Supramolecular Structure in Solutions of Low Molar Mass Compounds and Mixtures of Liquids. III. Correlation with Molecular Properties and Interactions. *J. Phys. Chem. B* **2006,** *110*, 13976-13984.

14. Sedlak, M., Large-Scale Supramolecular Structure in Solutions of Low Molar Mass Compounds and Mixtures of Liquids: II. Kinetics of the Formation and Long-Time Stability. *J. Phys. Chem. B* **2006,** *110*, 4339-4345.

15. Elton, D. C.; Fernandez-Serra, M., The hydrogen-bond network of water supports propagating optical phonon-like modes. *Nat. Commun.* **2015,** *7*, 10193.

16. Sloan, E. D.; Koh, C. A., *Clathrate Hydrates of Natural Gases*. Third ed.; CRC Press: Boca Raton, FL, 2008.

17. DeCiccio, D.; Ahn, S. T.; Senb, S.; Schunk, F.; Palmore, G. T. R.; Rose-Petruck, C., Electrochemical reduction of CO2 with clathrate hydrate electrolytes and copper foam electrodes. *Electrochem. Commun.* **2015,** *52*, 13-16.

18. Sayers, D. E.; Stern, E. A.; Lytle, F. W., New Technique for Investigating Noncrystalline Structures: Fourier Analysis of the Extended X-Ray- Absorptin Fine Structure. *Phys. Rev. Lett.* **1971,** *27*, 1204.

19. Bressler, C.; Chergui, M., Ultrafast X-ray Absorption Spectroscopy. *Chem. Rev.* **2004,** *104*, 1781-1812.

20. Campbell, L.; Hedin, L.; Rehr, J. J.; Bardyszewsk, W., Interference between extrinsic and intrinsic losses in x-ray absorption fine structure. *Phys. Rev. B* **2002,** *65*, 064107.

21. Stern, E. A., Theory of EXAFS. In *X-ray Absorption: Principles, Applications, Techniques of EXAFS, SEXAFS and XANES*, Koningsberger, D. C.; Prins, R., Eds. John Wiley & Sons: Now York, 1988; Vol. 92.

22. Vanko, F. D. G. G.; Glatzel, P., The 1s x-ray absorption pre-edge structures in transition metal oxides. *J. Phys.: Condens. Matter* **2009,** *21*.

23. Rehr, J. J.; Albers, R. C., Theoretical Approaches to X-ray Absorption Fine Structure. *Rev. Mod. Phys.* **2000,** *72*, 621-654.

24. Ankudinov, A. L.; Ravel, B.; Rehr, J. J.; Conradson, S. D., Real-space multiple-scattering calculation and interpretation of x-ray-absorption near-edge structure. *Phys. Rev. B* **1998,** *58*, 7565-7576.

25. Durham, P. J., Theory of XANES. In *X-ray Absorption: Principles, Applications, Techniques of EXAFS, SEXAFS and XANES*, Koningsberger, D. C.; Prins, R., Eds. Johns Wiley & Sons: New York, 1988; Vol. 91.

26. Gyorffy, B. L.; Stott, M. J., In *Band Structure Spectroscopy of Metals and Alloys*, Fabian, D. J.; Watson, L. M., Eds. Academic: London, 1973.

27. Rehr, J. J.; Kas, J. J.; Vila, F. D.; Prange, M. P.; Jorissen, K., Parameter-free calculations of x-ray spectra with FEFF9. *PCCP* **2010,** *12*, 5503-5513.

28. Rehr, J. J.; Kas, J. J.; Prange, M. P.; Sorini, A. P.; Takimoto, Y.; Vila, F. D., Ab initio theory and calculations of X-ray spectra. *Comptes Rendus Physique* **2009,** *10* (6), 548-559.

29. Kropman, M. F.; Nienhuys, H. K.; Bakker, H. J., Real-Time Measurement of the Orientational Dynamics of Aqueous Solvation Shells in Bulk Liquid Water. *Phys. Rev. Lett.* **2002,** *88*, 077601.

30. Bakker, H. J.; Woutersen, S.; Nienhuys, H.-K., Reorientational motion and hydrogen-bond stretching dynamics in liquid water. *Chem. Phys.* **2000,** *258*, 233-245.

31. Laage, D.; Hynes, J. T., A Molecular Jump Mechanism of Water Reorientation. *Science* **2006,** *311*, 832-835.

32. Bakker, H. J.; Rezus, Y. L. A.; Timmer, R. L. A., Molecular Reorientation of Liquid Water Studied with Femtosecond Midinfrared Spectroscopy. *J. Phys. Chem. A* **2008,** *112*, 11523-11534.

33. Buchner, R.; Hefter, G., Interactions and dynamics in electrolyte solutions by dielectric spectroscopy. *PCCP* **2009,** *11*, 8984-8999.

34. Fukasawa, T.; Sato, T.; Watanabe, J.; Hama, Y.; Kunz, W.; Buchner, R., Relation between Dielectric and Low-Frequency Raman Spectra of Hydrogen-Bond Liquids. *Phys. Rev. Lett.* **2005,** *95*.

35. Barthel, J.; Buchner, R.; Wurm, B., The dynamics of liquid formamide, N-methylformamide, N,N-dimethylformamide, and N,N-dimethylacetamide. A dielectric relaxation study. *J. Mol. Liq.* **2002,** *98-99*, 51-69.

36. Barthel, J.; Kleebauer, M.; Buchner, R., Dielectric relaxation of electrolyte solutions in acetonitrile. *J. Solution Chem.* **1995,** *24*, 1-17.

37. Buchner, R.; Barthel, J.; Stauber, J., The dielectric relaxation of water between 0°C and 35°C. *Chem. Phys. Lett.* **1999,** *306*, 57-63.

38. Kaatze, U., The dielectric properties of water in its different states of interaction. *J. Solution Chem.* **1997,** *26*, 1049-1112.

39. Buchner, R.; Hölzl, C.; Staubera, J.; Barthel, J., Dielectric spectroscopy of ion-pairing and hydration in aqueous tetra-n-alkylammonium halide solutions. *PCCP* **2002,** *4*, 2169-2179.

40. Wachter, W.; Buchner, R., Hydration of Tetraphenylphosphonium and Tetraphenylborate Ions by Dielectric Relaxation Spectroscopy. *J. Phys. Chem. B* **2006,** *110*, 5147-5154.

41. Buchner, R., Complexity in "simple" Electrolyte Solutions: Ion Pairing in MgSO4(aq). *J. Phys. Chem. B* **2004,** *108*, 2365-2375.

42. Baar, C.; Buchner, R.; Kunz, W., Dielectric Relaxation of Cationic Surfactants in Aqueous Solution. 1. Solvent Relaxation. *J. Phys. Chem. B* **2001,** *105*, 2906-2913.

43. Hofer, T. S.; Pribil, A. B.; Randolf, B. R., Capabilities of chemical simulation methods in the elucidation of structure and dynamics of solutions. *Pure Appl. Chem.* **2008,** *80*, 1195-1210.

44. Hofer, T. S.; Randolf, B. R.; Rode, B. M., Influence of polarization and many body quantum effects on the solvation shell of Al(III) in dilute aqueous solution-extended ab initio QM/MM MD simulations. *PCCP* **2005,** *7*, 1382-1387.

45. Schrodle, S.; Rudolph, W. W.; Hefter, G.; Buchner, R., Ion association and hydration in 3:2 electrolyte solutions by dielectric spectroscopy: Aluminum sulfate. *Geochim. Cosmochim. Acta* **2007,** *71*, 5287-5300.

46. Buchner, R., What can be learnt from dielectric relaxation spectroscopy about ion solvation and association? *Pure Appl. Chem.* **2008,** *80*, 1239-1252.

47. Buchner, R.; Hefter, G. T.; Barthel, J., Dielectric relaxation of aqueous NaF and KF solutions. *Journal of Chemical Society, Faraday Transactions* **1994,** *90*, 2475-2479.

48. Chen, T.; Hefter, G., Dielectric Spectroscopy of Aqueous Solutions of KCl and CsCl. *J. Phys. Chem. A* **2003,** *107*, 4025-4031.

49. Wachter, W.; Fernandez, Š.; Buchner, R., Ion Association and Hydration in Aqueous Solutions of LiCl and Li2SO4 by Dielectric Spectroscopy. *J. Phys. Chem. B* **2007,** *111*, 9010-9017.

50. Wachter, W.; Kunz, W.; Buchner, R., Is There an Anionic Hofmeister Effect on Water Dynamics? Dielectric Spectroscopy of Aqueous Solutions of NaBr, NaI, NaNO3, NaClO4, and NaSCN. *J. Phys. Chem. A* **2005,** *109*, 8675-8686.

51. Shelton, D. P., Electric field of Ions in solution probed by hyper-Rayleigh scattering. *J. Chem. Phys.* **2009,** *130*, 114501.

52. Roke, S.; Gonella, G., Nonlinear light scattering and spectroscopy of particles and droplets in liquids. *Annu. Rev. Phys. Chem.* **2012,** *63*, 353-378.

53. Beer, A. G. F. d.; Roke, S.; J. I. Dadap, Theory of optical second-harmonic and sum-frequency scattering from arbitrarily shaped particles. *J. Opt. Soc. Am. B* **2011,** *28*, 1374-1384.

54. Joseph, S.; Aluru, N. R., Pumping of Confined Water in Carbon Nanotubes by Rotation-Translation Coupling. *Phys. Rev. Lett.* **2008,** *101*, 064502.

55. Carey, D. M.; Korenowski, G. M., Measurement of the Raman spectrum of liquid wate. *J. Chem. Phys.* **1998,** *108*, 2669-2675.

56. Walrafen, G. E., Raman spectrum of water: transverse and longitudinal acoustic modes below .apprxeq.300 cm-1 and optic modes above .apprxeq.300 cm-1. *J. Phys. Chem.* **1990,** *94*, 2237-2239.

57. Walrafen, G. E.; Fisher, M. R.; Hokmabadi, M. S.; Yang, W.-H., Temperature dependence of the low- and high- frequency Raman scattering from liquid water. *J. Chem. Phys.* **1986,** *1986*, 6970-6982.

58. Zelsmann, H. R., Temperature dependence of the optical constants for liquid H2O and D2O in the far IR region. *J. Mol. Struct.* **1995,** *350*, 95-114.

59. Fukasawa, T.; Sato, T.; Watanabe, J.; Hama, Y.; Kunz, W.; Buchner, R., Relation between dielectric and low-frequency Raman spectra of hydrogen-bond liquids. *Phys. Rev. Lett.* **2005,** *95*, 197802.

60. Sampoli, M.; Ruocco, G.; Sette, F., Mixing of Longitudinal and Transverse Dynamics in Liquid Water. *Phys. Rev. Lett.* **1997,** *79*, 1678-1681.

61. Sette, F.; Ruocco, G.; Krisch, M.; Masciovecchio, C.; Verbeni, R.; Bergmann, U., Transition from Normal to Fast Sound in Liquid Water. *Phys. Rev. Lett.* **1996,** *77*, 83-86.

62. Sacchetti, F.; Suck, J.-B.; Petrillo, C.; Dorner, B., Brillouin neutron scattering in heavy water: Evidence for two-mode collective dynamics. *Physical Review E* **2004,** *69*, 061203.

63. Petrillo, C.; Sacchetti, F.; Dorner, B.; Suck, J.-B., High-resolution neutron scattering measurement of the dynamic structure factor of heavy water. *Physical Review E* **2000,** *62*, 3611-3618.

64. Pommeret, S.; Gobert, F.; Mostafavi, M.; Lampre, I.; Mialocq, J.-C., Femtochemistry of the Hydrated Electron at Decimolar Concentration. *J. Phys. Chem. A* **2001,** *105*, 11400-11406.

65. Lenchenkov, V.; Kloepfer, J.; Vilchiz, V.; Bradforth, S. E., Electron Photodetachment from [Fe(CN)6]4- : photoelectron relaxation and geminate recombination. *Chem. Phys. Lett.* **2001,** *342*, 277-286.

66. Crowell, R. A.; Bartels, D. M., Multiphoton Ionization of Liquid Water with 3.0-5.0 eV Photons. *J. Phys. Chem.* **1996,** *100*, 17940-17949.

67. Elles, C. G.; Jailaubekov, A. E.; Crowell, R. A.; Bradforth, S. E., Excitation-energy dependence of the mechanism for two-photon ionization of liquid H2O and D2O from 8.3 to 12.4 eV. *J. Chem. Phys.* **2006,** *125*, 044515.

68. Han, P.; Bartels, D. M., H/D Isotope Effects in Water Radiolysis. 2. Dissociation of Electronically Excited Water *J. Phys. Chem.* **1994,** *94*, 5824-5833.

69. Gürtler, P.; Saile, V.; Koch, E. E., Rydberg series in the absorption spectra of H2O and D2O in the vacuum ultraviolet. *Chem. Phys. Lett.* **1977,** *15*, 386-391.

70. Christiansen, O.; Nymand, T. M.; Mikkelsen, K. V., A theoretical study of the electronic spectrum of water. *J. Chem. Phys.* **2000,** *113*, 8101-8112.

71. Winter, B.; Weber, R.; Widdra, W.; Dittmar, M.; Faubel, M.; Hertel, I. V., Full Valence Band Photoemission from Liquid Water Using EUV Synchrotron Radiation. *J. Phys. Chem. A* **2004,** *108*, 2625-2632.

72. Laenen, R.; Roth, T.; Laubereau, A., Novel Precursors of Solvated Electrons in Water: Evidence for a Charge Transfer Process. *Phys. Rev. Lett.* **2000,** *85*, 50-53.

73. Subramanian, D.; Anisimov, M. A., Resolving the Mystery of Aqueous Solutions of Tertiary Butyl Alcohol. *J. Phys. Chem. B* **2011,** *115* (29), 9179.

74. Euliss, G. W.; Sorensen, C. M., Dynamic light scattering studies of concentration fluctuations in aqueous t-butyl alcohol solutions. *J. Chem. Phys.* **1984,** *80* (10), 4764.

75. Lackner, K. S., Capture of carbon dioxide from ambient air. *The European Physical Journal Special Topics* **2009,** *176*, 93-106.

76. House, K. Z.; Baclig, A. C.; Ranjan, M.; Nieropb, E. A. v.; Wilcoxd, J.; Herzogc, H. J., Economic and energetic analysis of capturing CO2 from ambient air. *Proc. Natl. Acad. Sci. U.S.A.* **2010,** *108*, 20428-20433.

77. Kuhl, K. P.; Cave, E. R.; Abramc, D. N.; Jaramillo, T. F., New insights into the electrochemical reduction of carbon dioxide on metallic copper surfaces. *Energy & Environmental Science* **2012,** *5*, 7050-7059.

78. Peterson, A. A.; Abild-Pedersen, F.; Studt, F.; Rossmeisla, J.; Nørskov, J. K., How copper catalyzes the electroreduction of carbon dioxide into hydrocarbon fuels. *Energy & Environmental Science* **2010,** *3*, 1311-1315.

79. Hori, Y.; Kikuchi, K.; Suzuki, S., Production of CO and CH4 in electrochemical reduction of CO2 at metal electrodes in aqueous hydrogencarbonate solution. *Chem. Lett.* **1985,** *14* (11), 1695-1698.

80. Hara, K.; Kudo, A.; Sakata, T., Electrochemical reduction of carbon dioxide under high pressure on various electrodes in an aqueous electrolyte. *J. Electroanal. Chem.* **1995,** *391*, 141-147.

81. Carroll, J. J.; Slupsky, J. D.; Mather, A. E., The Solubility of Carbon Dioxide in Water at Low Pressure. *J. Phys. Chem. Ref. Data* **1991,** *20*, 1201-1209.

82. Sen, S.; Liu, D.; Palmore, G. T. R., Electrochemical Reduction of CO2 at Copper Nanofoams. *ACS Catalysis* **2014,** *4*, 3091-3095.

83. Linga, P.; Kumar, R.; Englezos, P., Capture of carbon dioxide from conventional power plants or from integrated gasification plants through gas hydrate formation/dissociation. *Journal of Energy and Climate Change* **2006,** *1*.

84. Linga, P.; Adeyemo, A.; Englezos, P., Medium-pressure clathrate hydrate/membrane hybrid process for postcombustion caputre of carbon dioxide. *Environ. Sci. Technol.* **2008,** *42*, 315-320.

85. Attwood, D., *Soft X-rays and extreme ultraviolet radiation: Principles and Applications*. Cambridge University PRESS: New York, 1999.

86. Kim, K.-J. In *Characteristics of Synchrotron Radiation*, Physics of Particle Accelerators, AIP Conference Proccedings, New York, Month, M.; Dienes, M., Eds. Amer. Inst. of Physics: New York, 1989.

87. Winick, H., Synchrotron Radiation Sources- Present Capabilities and Future Directions. *J. Synchrotron Rad.* **1998,** *5*, 168-175.

88. Feng, J.; Engelhorn, K.; Cho, B. I.; Lee, H. J.; Greaves, M.; Weber, C. P.; Falcone, R. W.; Padmore, H. A.; Heimann, P. A., A grazing incidence x-ray streak camera for ultrafast, single-shot measurements. *Appl. Phys. Lett.* **2010,** *96*, 134102.

89. Chollet, M.; Ahr, B.; Walko, D. A.; Rose-Petruck, C.; Adams, B., 2-ps Hard X-Ray Streak Camera Measurements at Sector 7 Beamline of the Advanced Photon Source. *IEEE J. Sel. Topics Quantum Electron.* **2011,** *18* (1), 66 - 73.

90. Henke, B. L.; Knauer, J. P.; Premaratne, K., The characterization of X-ray probe photocathodes in the 0.1-10-KeV photon energy rergion. *J. Appl. Phys.* **1981,** *52*, 1509-1520.

91. Adams, B. W.; Rose-Petruck, C., X-ray focusing scheme with continuously variable lens. *J. Synchrotron Rad.* **2005,** *22*, 16-22.

92. Adams, B. W.; Rose-Petruck, C.; Jiao, Y., Picosecond-resolved X-ray absorption spectroscopy at low signal contrast using a hard X-ray streak camera. *J. Synchrotron Rad.* **2015,** *22*, 1022-1029.

93. Frisch, M. J.; Trucks, G. W.; Schlegel, H. B.; Scuseria, G. E.; Robb, M. A.; Cheeseman, J. R.; Scalmani, G.; Barone, V.; Mennucci, B.; Petersson, G. A.; Nakatsuji, H.; Caricato, M.; Li, X.; Hratchian, H. P.; Izmaylov, A. F.; Bloino, J.; Zheng, G.; Sonnenberg, J. L.; Hada, M.; Ehara, M.;

Toyota, K.; Fukuda, R.; Hasegawa, J.; Ishida, M.; Nakajima, T.; Honda, Y.; Kitao, O.; Nakai, H.; Vreven, T.; J. A. Montgomery, J.; Peralta, J. E.; Ogliaro, F.; Bearpark, M.; Heyd, J. J.; Brothers, E.; Kudin, K. N.; Staroverov, V. N.; Kobayashi, R.; Normand, J.; Raghavachari, K.; Rendell, A.; Burant, J. C.; Iyengar, S. S.; Tomasi, J.; Cossi, M.; Rega, N.; Millam, J. M.; Klene, M.; Knox, J. E.; Cross, J. B.; Bakken, V.; Adamo, C.; Jaramillo, J.; Gomperts, R.; Stratmann, R. E.; Yazyev, O.; Austin, A. J.; Cammi, R.; Pomelli, C.; Ochterski, J. W.; Martin, R. L.; Morokuma, K.; Zakrzewski, V. G.; Voth, G. A.; Salvador, P.; Dannenberg, J. J.; Dapprich, S.; Daniels, A. D.; Farkas, Ö.; Foresman, J. B.; Ortiz, J. V.; Cioslowski, J.; D. J. Fox, G. *Gaussian 09, Revision E.01*, Gaussian, Inc.: Wallingford, CT, USA, 2009.

94. Reiher, M.; Salomon, O.; Hess, B. A., Reparameterization of hybrid functionals based on energy differences of states of different multiplicity. *Theor. Chim. Acta* **2001,** *107*, 48-55.

95. Weigend, F.; Ahlrichs, R., Balanced basis sets of split valence, triple zeta valence and quadruple zeta valence quality for H to Rn: Design and assessment of accuracy. *PCCP* **2005,** *7*, 3297-3305.

96. Weigend, F.; Hser, M., RI-MP2: optimized auxiliary basis sets and demonstration of efficiency. *Chem. Phys. Lett.* **1998,** *294*, 143-152.

97. Enkovaara, J.; Rostgaard, C.; Mortensen, J. J.; Chen, J.; Dulak, M.; Ferrighi, L.; Gavnholt, J.; Glinsvad, C.; Haikola, V.; Hansen, H. A.; Kristoffersen, H. H.; Kuisma, M.; Larsen, A. H.; Lehtovaara, L.; Ljungberg, M.; Lopez-Acevedo, O.; Moses, P. G.; Ojanen, J.; Olsen, T.; Petzold, V.; Romero, N. A.; Stausholm-Moller, J.; Strange, M.; Tritsaris, G. A.; Vanin, M.; Walter, M.; Hammer, B.; Hkkinen, H.; Madsen, G. K. H.; Nieminen, R. M.; Norskov, J. K.; Puska, M.; Rantala, T. T.; Schiotz, J.; Thygesen, K. S.; K. W. Jacobsen, Electronic structure calculations with gpaw: a real-space implementation of the projector augmented-wave method. *J. Phys.: Condens. Matter* **2010,** *22*, 253202.

98. J. Mortensen, L. H., and K. W. Jacobsen, Real-space grid implementation of the projector augmented wave method. *Phys. Rev. B* **2005,** *71*, 35109.

99. Perdew, J. P.; Burke, K.; Ernzerhof, M., Generalized gradient approximation made simple. *Phys. Rev. Lett.* **1996,** *77*, 3865-3868.

100. Jorgensen, W. L.; Chandrasekhar, J.; Madura, J. D.; Klein, M. L., Comparison of simple potential functions for simulating liquid water. *J. Chem. Phys.* **1983,** *79*, 926-935.

101. Bahn, S. R.; Jacobsen, K. W., An object-oriented scripting interface to a legacy electronic structure code. *Computing in Science & Engineering* **2002,** *4*, 56-66.

102. Jónsson, E. Ö.; Jacobsen, K. W.; Thygesen, K. S.; Ulstrup, J. Computational Approach to Electron Charge Transfer Reactions. Thesis, Technical University of Denmark, 2014.

103. Dohn, A. O.; Jonsson, E. O.; Kjær, K. S.; Driel, T. B. v.; Nielsen, M. M.; Jacobsen, K. W.; Henriksen, N. E.; Møller, K. B., Direct dynamics studies of a binuclear metal complex in solution: The interplay between vibrational relaxation, coherence, and solvent effects. *J. Phys. Chem. Lett.* **2014,** *5*, 2414-2418.

104. Dohn, A. O., *Transient Changes in Molecular Geometries and How to Model Them*. Springer International Publishing: 2014.

105. Rappe, A.; Casewit, C.; Colwell, K.; III, W. G.; Ski, W., UFF, a full periodic table force field for molecular mechanics and molecular dynamics simulations. *J. Am. Chem. Soc.* **1992,** *114*, 10024-10035.

106. Rehr, J. J.; Ankudinov, A. L., Progress and challenges in the theory and interpretation of X-ray spectra. *J. Synchrotron Rad.* **2001,** *8*, 61-65.

107. Smith, J. W.; Lam, R. K.; Shih, O.; Rizzuto, A. M.; Prendergast, D.; Saykally, R. J., Properties of aqueous nitrate and nitrite from x-ray absorption spectroscopy. *J. Chem. Phys.* **2015,** *143*, 084503.

108. Gutsev, G. L.; Rao, B. K.; Jena, P., Photodecomposition of MnO4-: A Theoretical Study. *J. Phys. Chem. A* **1999,** *103*, 10819-10824.

109. Nakai, H.; Ohmori, Y.; Nakatsuji, H., Theoretical Study on the Photochemical Decomposition Reaction of Permanganate Ion, MnO4-. *J. Phys. Chem.* **1995,** *99*, 8550-8555.

110. Donald G. Lee, C. R. M., Takatoshi Hayashi, John I. Braurnan, Photochemistry of Aqueous Permanganate Ion. *J. Am. Chem. Soc.* **1987,** *109*, 3003-3010.

111. Li, Y. Applications of transient grating spectroscopy to temperature and transport properties measurements in high-pressure environments. Thesis, North Carolina State University, 2001.

112. Boyd, R. W., *Nonlinear Optics*. Academic Press: Boston, 1992.

113. Berne, B. J.; Pecora, R., *Dynamics Light Scattering: With Applications to Chemistry, Biology and Physics*. Dover Publications: Mineola, 2000.

114. Silvestri, S. D.; Fujimoto, J. G.; Ippen, E. P.; Jr., E. B. G.; Williams, L. R.; Nelson, K. A., Femtosecond time-resolved measurements of optic phonon dephasing by impulsive stimulated raman scattering in α-perylene crystal from 20 to 300 K. *Chem. Phys. Lett.* **1985,** *116*, 146-152.

115. Jiao, Y.; Adams, B. W.; Dohn, A. O.; Jonsson, H.; Rose-Petruck, C., Second Harmonic Phonon generation carried by ice-like structure in aqueous solutions. *Journal of Physical Chemistry Letters* **2016,** *To be Submitted*.

116. Shirom, M.; Stein, G., Excited State Chemistry of the Ferrocyanide Ion in Aqueous Solution. I. Formation of the Hydrated Electron. *J. Chem. Phys.* **1971,** *55*, 3372-3378.

117. Shirom, M.; Stein, G., Excited State Chemistry of the Ferrocyanide Ion in Aqueous Solution. II. Photoaquation. *J. Chem. Phys.* **1971,** *55*, 3379-3382.

118. Alexander, J. J.; Gray, H. B., Molecular orbital theory for metal complexes: ferrocyanide and cobalticyanide ions. *Coord. Chem. Rev.* **1967,** *2*, 15-28.

119. Reinhard, M.; Penfold, T. J.; Lima, F. A.; Rittmann, J.; Rittmann-Frank, M. H.; Abela, R.; Tavernelli, I.; Rothlisberger, U.; Milne, C. J.; Chergui, M., Photooxidation and photoaquation of iron hexacyanide in aqueous solution: A picosecond X-ray absorption study. *Structural Dynamics* **2014,** *1*, 024901.

120. Lee, T.; Jiang, Y.; Rose-Petruck, C. G., Ultrafst table-top laser-pump-x-ray-probe measurment of solvated Fe(CN)4-. *J. Chem. Phys.* **2005,** *122*, 084506.

121. Ohta, K.; Maekawa, H.; Tominaga, K., Vibrational Population Relaxation and Dephasing Dynamics of Fe(CN)64- in D2O with Third-Order Nonlinear Infrared Spectroscopy. *J. Phys. Chem. A* **2004,** *108*, 1333-1341.

122. Santucci, S. C.; Fioretto, D.; Comez, L.; Gessini, A.; Masciovecchio, C., Is There Any Fast Sound in Water? *Phys. Rev. Lett.* **2006,** *97*, 225701.

123. Lankford, J. I.; Holladay, W. T.; Criss, C. M., Isentropic Compressibilities of Univalent Electrolytes in Methanol at 25 C. *J. Solution Chem.* **1984,** *13*, 699.

124. Young, R. M.; Neumark, D. M., Dynamics of Solvated Electrons in Clusters. *Chem. Rev.* **2012,** *112*, 5553-5577.

125. Abel, B.; Buck, U.; Sobolewskic, A. L.; Domcked, W., On the nature and signture of the solvated electron in water. *PCCP* **2012,** *14*, 22-34.

126. Hammer, N. I.; Shin, J.-W.; Jeffrey M. Headrick; Diken, E. G.; Roscioli, J. R.; Weddle, G. H.; Johnson, M. A., How do small water clusters bind an excess electron? *Science* **2004,** *306*, 675-679.

127. Tielrooij, K. J.; Garcia-Araez, N.; Bonn, M.; Bakker, H. J., Cooperativity in Ion Hydration. *Science* **2010,** *328*, 1006-1009.

128. Bakker, H. J., Structural Dynamics of Aqueous Salt Solutions. *Chem. Rev.* **2008,** *108*, 1456-1473.

129. DiTuccia, M. J.; Williams, E. R., Nanometer patterning of water by tetraanionic ferrocyanide stabilized in aqueous nanodrops. *Chemical Science* **2017**.

130. Jiao, Y.; Adams, B. W.; Rose-Petruck, C., Aqueous solutions contain mesoscopic domains with high solute concentrations and ice-like high-frequency stiffness. *J. Am. Chem. Soc.* **2016,** *Submitted*.

131. Nortemann, K.; Hilland, J.; Kaatze, U., Dielectric Properties of Aqueous NaCl Solutions at Microwave Frequencies. *J. Phys. Chem. A* **1997,** *101*, 6864-6869.

132. Vassiliev, Y. B.; Bagotzky, V. S.; Osetrova, N. V.; Mikhailova, A. A., Electroreduction of carbon dioxide: Part III. Adsorption and reduction of CO2 on platinum. *Journal of Electroanalytical Chemistry and Interfacial Electrochemistry* **1985,** *189*, 311-324.

133. Hori, Y.; Murata, A.; Takahashi, R., Formation of hydrocarbons in the electrochemical reduction of carbon dioxide at a copper electrode in aqueous solution. *Journal of the Chemical Society, Faraday Transactions 1: Physical* **1989,** *85*, 2309-2326.